5-5-2021

An Investigation of the Effects of Variable Magnetic Field Gradients on Soot and CO Emissions from Non-Premixed Hydrocarbon Flames

Edison Ekperechukwu Chukwuemeka
Louisiana State University and Agricultural and Mechanical College

AN INVESTIGATION OF THE EFFECTS OF VARIABLE MAGNETIC FIELD GRADIENTS ON SOOT AND CO EMISSIONS FROM NON-PREMIXED HYDROCARBON FLAMES

A Dissertation

Submitted to the Graduate Faculty of the
Louisiana State University and
Agricultural and Mechanical College
in partial fulfillment of the
requirements for the degree of
Doctor of Philosophy

in

The Department of Mechanical and Industrial Engineering

by
Edison Ekperechukwu Chukwuemeka
B.Sc., University of Lagos, 2008
MSc., Louisiana State University, 2021
August 2021

Dedicated to my parents and family.

Acknowledgments

Sincere gratitude goes to my PhD advisors Prof. Tryfon T. Charalampopoulos (Deceased) and Prof. Ingmar Schoegl for their continuous support and guidance during the course of my study and in completing this dissertation .

Appreciation goes to Prof. Ram Devireddy, Prof. Guoqiang Li, and Dr. Shyam Menon for accepting to be members of my PhD Dissertation committee. In addition, I appreciate Prof. Kerry M. Dooley for accepting to be the dean's representative of my dissertation. Thank you for your thoughtful comments and suggestions on how to improve my research work.

Sincere gratitude goes to the Department of Mechanical Engineering at Louisiana State University for supporting my doctorate program with the Teaching Assistantship program. Also, I would like to acknowledgment the resources provided by the high performance computing center at Louisiana State University.

Gratitude and appreciation goes to my family members, who have supported my ambitions and goals during the duration of the program at Louisiana State University. Thanks to my friends, faculties and colleagues at Louisiana State University, who have directly and indirectly assisted me in accomplishing this feat.

Finally and above all, thanks to God Almighty for his providence and sustenance during the program.

Table of Contents

List of Tables

List of Figures

Nomenclature

Latin Letters

$\left(\frac{\mathrm{A}}{\mathrm{F}}\right)_{actual}$ Actual Air-Fuel ratio

$\left(\frac{\mathrm{A}}{\mathrm{F}}\right)_{stoic}$ Stoichiometric Air-Fuel ratio

a, b Apparatus dependent constants

A_j^f Pre-exponential factor of the forward reaction

$\mathbf{B}$ Magnetic field induction [T]

$\mathbf{B}_{ext}$ External magnetic field intensity [T]

b_n^* Normalized soot nuclei concentration [particles $\times 1 \times 10^{-15}$/kg]

c Model parameter

C_s Soot mass loading [kg/m^3]

C_α Soot inception rate model constant [1/s]

C_β Soot coagulation rate model constant

C_γ Soot surface growth rate model scaling factor [kgm/kmols]

$\mathrm{C}_{\omega_1}, \mathrm{C}_{\omega_2}$ Soot oxidation model constant for OH and O respectively [kg – m/(kmolK$^{\frac{1}{2}}$s)]

C_{ox} Soot oxidation scaling parameter

c_p Specific heat capacity of the mixture [J/kgK]

$\mathbf{D}$ Electric field displacement [C^2/m]

$\mathcal{D}a$ Damköhler number

$\mathcal{D}_{kj}$ Concentration diffusivity of $k-th$ species in $j-th$ species [m^2/s]

$\mathcal{D}_{k\mathrm{N}}$ Average diffusion coefficient of species k [m^2/s]

$\mathcal{D}_{\mathrm{T}k}$ Soret diffusivity coefficient [m^2/s]

d_p Soot average diameter [m]

$\mathbf{E}$ Electric field intensity [V/m]

E Activation energy [kJ/kgmol]

E_j^f Activation energy of the forward reaction

e_t Total specific internal energy [kJ/kg]

f Branching coefficient

$\mathbf{F}_m$ Magnetic Force [N]

f_k Body force per unit mass [N/kg]

F_v Integrated soot volume fraction

f_v Soot volume fraction

f_v Soot volume fraction

g Termination coefficients

$\mathbf{H}$ Magnetic field strength [A/m]

h Specific enthalpy of the fluid mixture [kJ/kg]

h_k Specific enthalpy of the gaseous species k [kJ/kg]

h_k^0 Standard state enthalpy of formation of species k [kJ/kg]

h_k^s Sensible enthalpy of species k [kJ/kg]

i Current flow [A]

I_{ij} Identity tensor

$\mathbf{J}$ Current density [A^2/m]

k_j^f Forward reaction rate constant

l, m, n Soot model parameters

$\mathbf{M}$ Magnetization vector [A/m]

M Soot mass concentration [kg/m^3]

M_p Mass of incipient soot [kg/kmol]

n Number density of soot particle [$particles/m^3$]

N Soot particles number density [particles/kg – mixture]

N Soot number density [$particles1/m^3$]

n_0 Rate of spontaneous generation of nuclei

p Hydrostatic pressure [N/m^2]

P_{ij} Hydrostatic pressure Tensor [N/m^2]

$\dot{\mathrm{Q}}$ Heat generated per unit volume [J/m^3]

q_i Heat flux [J/m^2]

Q_{cv} Heat of Reaction [kJ/kgmol]

q Charge [C]

$\mathcal{R}$ Universal gas constant [J/kgmolK]

R_g Rate of soot particles' surface growth

S Surface area per unit volume of a spherical particle [1/m]

TSI Threshold Sooting Index

T Temperature [K]

T_α Soot inception rate activation temperature [K]

T_γ Soot surface growth rate activation temperature [K]

U Fluid velocity magnitude [m/s]

u_i Average velocity components of the fluid mixture in each direction i [m/s]

V_u Volume of the soot formation zone [m^3]

$V_{k,i}$and $V_{j,i}$ Diffusion velocity of the $k-th$ and $j-th$ species [m/s]

V_{NTP} Volume of the cylinder contents at normal temperature and pressure [m^3]

V_{ki} Diffusion velocity of specie k in direction i

W_k Molecular weight of the gaseous species k

X_k Mole fraction of species k

Y_k Mass fraction of species k

Y_s Soot mass fraction

Greek Letters

ΔH Enthalpy of Formation [kJ/kgmol]

ρ_s Soot density

α Empirical steric factor

β_j^f Temperature exponent of the forward reaction

χ_j Mole fraction of species j

ϕ_c Threshold equivalence ratio

ϕ_u Local unburned equivalence ratio

η Thermophoretic diffusivity coefficient

η_{col} Collision efficiency parameter

λ Thermal conductivity of the fluid mixture [W/m^2K]

μ Fluid viscosity [Pa s]

$\mu_{m,0}$ Magnetic permeability of free space [H/m]

$\dot{\omega}_k$ Rate of production of species k

$\dot{\omega}_F, \dot{\omega}_{ox}$ Rate of consumption of the fuel and oxidizer respectively

ϕ Equivalence ratio

Ψ_{C_s} Number of surface radicals per unit surface area

ρ Density of multi-component system [kg/m^3]

ρ_c Electric charge density [C/m^3]

ρ_s Soot density [kg/m^3]

σ_{ji} Stress tensor [N/m^2]

σ_n Schmidt number of the soot nuclei

σ_s Schmidt number of the soot particle

τ_{ji} Shear stress [N/m^2]

Abstract

The interaction of the paramagnetic species in a combustion process with the magnetic field placed in the vicinity of non-premixed flames affects the characteristics of the non-premixed flames - flame height and flame lift-off height. However, the effect of this magnetic interaction on the pollutants generated by the flame is unknown.

In general, pollutant formation is promoted in most combustion systems due to incomplete combustion of the hydrocarbon due to improper mixing. Since paramagnetic combustion species such as O_2, O, OH, etc interacts with magnetic fields and possess a preferential motion direction, imposing magnetic field on non-premixed flames has a potential of improving the mixing characteristics of the combustion process.

To study the effect of magnetic fields on the pollutants of non-premixed flames, a computational study is conducted on an axisymmetric co-flow laminar propane – air non-premixed flame computed with a detailed gas phase mechanism. The pollutants of interests are soot and CO. Moreover, the formation of soot is modeled using the Moss-Brooks model with some modified parameters.

Based on the computed results, the effects of the imposed magnetic fields on the pollutants (soot and CO) depend on the magnitude of the magnetic field gradient imposed on the flame.

Chapter 1.
Introduction

With recent advancements in the computational power of computer hardware, numerical simulations of physical phenomena have been accepted in the engineering environment as a tool to improve the design process. In this regard, numerical modeling has been used in analyzing physical process such as heat transfer, fluid flow and structural behavior of materials.

This dissertation discusses the application of numerical modeling to analyze the effect of non-uniform magnetic fields on the emission of pollutants such as CO and soot. The numerical computation was conducted using a commercially available computational tool, but was modified to suit the analysis being conducted.

The objective of the research is to evaluate the impact of varying magnetic field configuration on pollutants generated in co-flowing propane-air non-premixed flames. This chapter gives an overview of combustion science, soot formation, and magnetism. In addition, the structure of the dissertation is summarized.

1.1. Overview of Combustion Science

The science that deals with the exothermic chemical reactions in flow which results in heat and mass transfer is defined as combustion science [3]. As the oldest technology, combustion resulted in the emergence of technological advancement, which has improved the lifestyle of humanity. According to a recent report, combustion processes generate about 65 % of the world's electricity or power demand [4].

Combustion processes have application in vast areas such as power generation, process industry, and heating. Although combustion has been useful in different aspects of life and also in technological advancement, it has a huge negative impact on the environment due to by-products emanating from the process [5]. With these in mind, combustion scientists have identified different modes of combustion phenomena.

The modes of combustion have be classified as either flame and non-flame mode [5].

Combustion process is said to be in the flame mode when the accompanying chemical reaction occurs within a finite region before propagating downstream in the domain. However, the non-flame mode of combustion occurs when the chemical reaction takes place within the whole domain. This work focuses on the flame mode of combustion as elaborated below.

Flames are classically categorized as either premixed flames or non-premixed flames based on the mixing characteristics of reactants within the flow before burning or chemical reaction takes place as shown in Figure 1.1.. In premixed flames, the reactants are properly mixed initially before chemical reaction or combustion is initiated within the fluid flow as depicted in Figure 1.1.a. This type of flame is common in Bunsen burners used in heating and cooking applications. Premixed flames are also present in spark ignition engines (gasoline engines) [5–7].

However, in non-premixed flames, the reactants which were not mixed initially during the flow diffuse towards each other so as to initiate combustion as shown in Figure 1.1.b. As a result, the combustion process will take place in the region with an appropriate amount of the oxidizer and fuel [5–7]. This flame type is common in furnaces, compression ignition engines (diesel engines), and turbine engines.

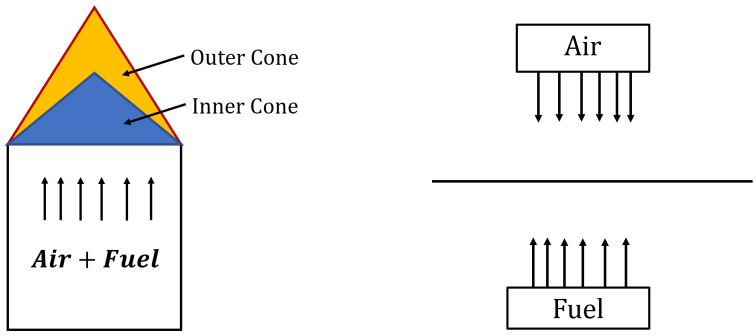

(a) Premixed flame (b) Non-premixed flame

Figure 1.1. Types of flames

Other than premixed and non-premixed flames, researchers have proposed a new class of flame known as partial premixed flames. In this type of flame, an initial

premixed reactant is allowed to react with an oxidizer flow for combustion to occur. This type of flame was proposed as a strategy to stabilize non-premixed flames [8].

Furthermore, non-premixed flames have been categorized as counter-flow and co-flow non-premixed flames based on the flow directions of the oxidizers and the fuels. An example of a counter-flow non-premixed flames is shown in Figure 1.1.b. As depicted, the reactants flow in opposite direction towards each other. The reaction takes place at the plane where they mix. However, in co-flowing non-premixed flames, the oxidizer and fuel flow parallel to each other as shown in Figure 1.2.. Co-flowing non-premixed flames have been classified as either normal diffusion flame (NDF) as depicted in Figure 1.2.a or inverse diffusion flame (IDF) as depicted in Figure 1.2.b.

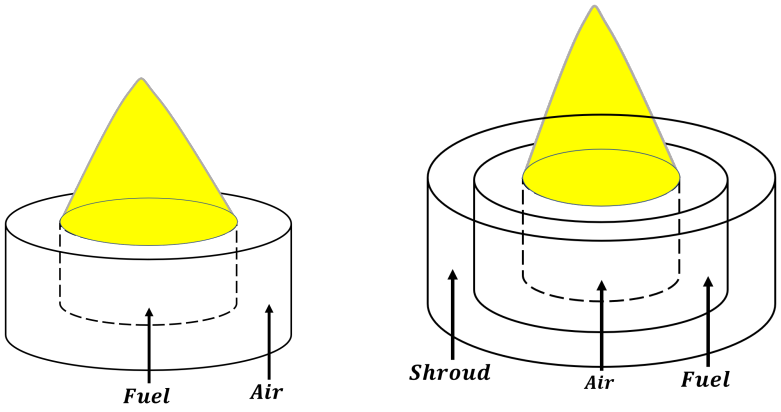

(a) Normal diffusion flame (b) Inverse diffusion flame

Figure 1.2. Classification of co-flow non-premixed

1.1.1. Classification of Flames

Based on the flow conditions of the reactants and products, flames have been classified as either laminar or turbulent [6, 7].

Laminar Flames: In this type of flames, the flow of the fuel and oxidizer before combustion is laminar i.e. the Reynolds' Number $\mathcal{R}e \leq \mathcal{R}e_{cr}$, where $\mathcal{R}e_{cr}$ is the critical Reynolds' Number.

The Reynolds' number $\mathcal{R}e_D$ of fluid flowing through a pipe of diameter D with

velocity V is given as:

$$\mathcal{R}e_D = \frac{\rho V D}{\mu}$$

However, the Renolds' number $\mathcal{R}e_L$ of fluid flowing over a flat surface of length L is given as:

$$\mathcal{R}e_L = \frac{\rho V L}{\mu}$$

The critical Reynolds' number of fluid flowing over a flat plate is $\mathcal{R}e_{cr} = 5 \times 10^5$, while the critical Reynolds' number of flow through a pipe is $\mathcal{R}e_{cr} = 2.2 \times 10^3$. This flame could either be premixed or non-premixed. This research work considers the laminar flow region through a pipe.

Turbulent Flames: The flow of the fuel and oxidizer in this combustion process are turbulent i.e. the Reynolds' number $\mathcal{R}e > \mathcal{R}e_{cr}$. In addition, this flame could be either premixed or non-premixed, where $\mathcal{R}e_{cr}$ is the critical Reynolds' Number.

1.2. Combustion Processes

Flames are the result of a particular type of chemical reaction called combustion reaction. These reactions are exothermic chemical reactions which involve the reaction of an oxidant (air or oxygen) with combustible materials such as Hydrocarbons – fuel. The chemical reaction is classified as an exothermic reaction because heat is released during the process while producing new chemical species as products of the reaction. Most chemical reactions involving hydrocarbons and oxidizer are called combustion reaction due to the amount of energy released during the process. Most of the heat released during combustion process are due to the formation of CO_2 and H_2O. The formation of CO_2 in any combustion process involves the reaction between C and O_2 which entails the formation of CO and further reaction with O_2 to produce CO_2 as given below [5]:

$$C + O_2 \rightarrow CO + \frac{1}{2}O_2 \rightarrow CO_2 \qquad \Delta H = -389.9\,\text{kJ/kgmol} \tag{1.1.}$$

Similarly, the formation of water vapor releases heat to the surroundings as shown below:

$$H_2 + \frac{1}{2}O_2 \rightarrow H_2O \qquad \Delta H = -241.8\,\text{kJ/kgmol} \tag{1.2.}$$

In general, a global stoichiometric combustion reaction of hydrocarbons (C_xH_y) in air is expressed mathematically or theoretically as:

$$C_xH_y + \left(x + \frac{y}{4}\right)(O_2 + 3.76N_2) \rightarrow xCO_2 + \frac{y}{2}H_2O + 3.76\left(x + \frac{y}{4}\right)N_2 \qquad \Delta H = -Q_{cv} \tag{1.3.}$$

The stoichiometric reaction is the theoretical reaction which represents the complete combustion of the fuel in the presence of the oxidizer. In other words, the reaction involves the theoretical amount of oxidizer that converts the hydrocarbon completely to CO_2 and H_2O.

The equivalence ratio ϕ is defined as the ratio of stoichiometric air-fuel ratio to the actual air-fuel ratio of the combustion reaction. This is used to quantitatively measure the richness of any fuel in a combustion process. Mathematically, it is expressed as:

$$\phi = \frac{\left(\frac{A}{F}\right)_{stoic}}{\left(\frac{A}{F}\right)_{actual}} \tag{1.4.}$$

When the amount of oxidizer present is less than the stoichiometric quantity required, the combustion reaction is said to be fuel rich (rich) and $1 < \phi < \infty$. However, when the oxidizer exceeds the stoichiometric required amount, the combustion reaction is said to be fuel lean (lean) and $0 < \phi < 1$ [9]. Although this theoretical reaction has provided insights into some thermodynamic properties of combustion processes, the reaction does not represent the actual behavior of combustion process in most applications. The actual behavior of combustion process is captured by elementary reactions. An elementary reaction is the reaction that takes place at the

molecular level just as it is represented by the reaction equation [7].

Accurate predictions of the essential characteristics of non-premixed flames in practical combustion systems require a detailed chemistry which incorporates the finite rate theory in the computation. The chemical reaction rate used in this type of computation is computed based on Arrhenius theory. The rate of production of species in the combustion system $\dot{\omega}_k$ is given as [10]

$$\dot{\omega}_k = \sum_{j=1}^{N} \left(v_{jk}^{''} - v_{jk}^{'} \right) \left[k_j^f (T) \prod_{n=1}^{K} \left(\frac{\rho Y_n}{W_n} \right)^{v_{jn}^{'}} - k_j^r (T) \prod_{n=1}^{K} \left(\frac{\rho Y_n}{W_n} \right)^{v_{jn}^{''}} \right] \tag{1.5.}$$

k_j^f, k_j^r are the forward and reverse rate constant for reaction j respectively. The forward reaction rate constant is given by the modified Arrhenius temperature dependence as:

$$k_j^f = A_j^f T^{\beta_j^f} \exp\left(\frac{E_j^f}{\mathcal{R} T} \right) \tag{1.6.}$$

A_j^f is the pre-exponential factor, β_j^f the temperature exponent, and E_j^f activation energy of the forward reaction path are evaluated for the chemical reaction rate constant. The reverse reaction rate constant for each reaction path could be expressed in terms of the forward reaction rate constant and chemical equilibrium constant K_j^c as:

$$k_j^r = \frac{k_j^f}{K_j^c} \tag{1.7.}$$

Theoretically, the stoichiometric condition would result in the maximum adiabatic temperature in a combustion reaction. However, a computational analysis of the adiabatic temperature of some fuels in a constant pressure reactor has shown that the peak adiabatic temperature occurs at an equivalence ratio greater than 1, which is not the stoichiometric condition [5]. Considering the combustion of propane in a constant

pressure reactor, the adiabatic temperature was computed for various equivalence ratio ϕ assuming equilibrium composition. This computation shows that the adiabatic temperature of the combustion process was $T_{ad} \approx 2260\,K$ at the equivalence ratio $\phi \approx 1.1$, which does not match the theoretical prediction of the stoichiometric condition as shown in Figure 1.3.. The mole fraction of the major species at different

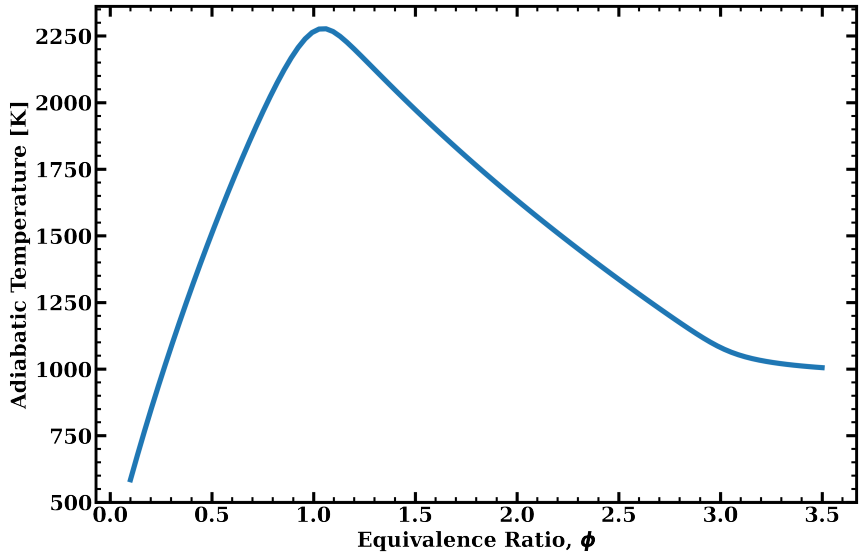

Figure 1.3. C_3H_8 - Air adiabatic temperature for different equivalence ratios

equivalence ratio was obtained as shown in Figure 1.4..

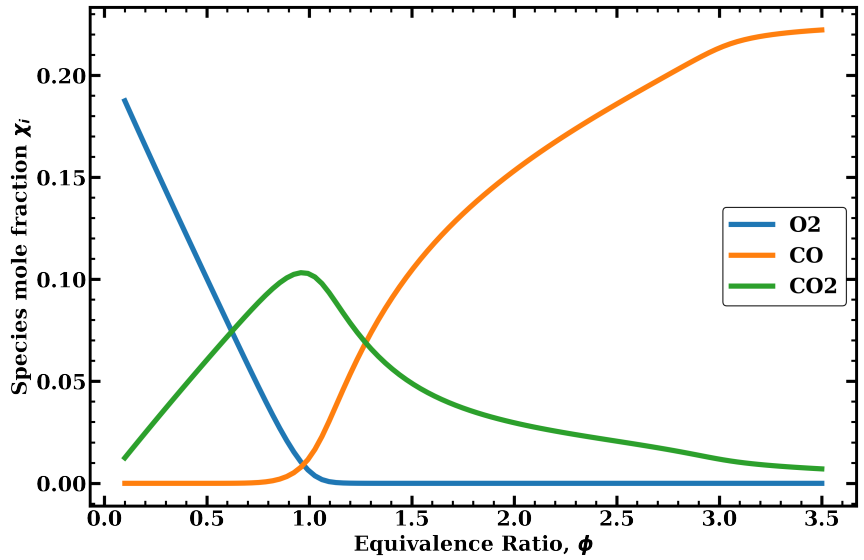

Figure 1.4. Equilibrium composition of major species of C_3H_8 - Air at different equivalence ratios

1.3. Fundamentals of Non-Premixed Flames

Non-premixed flames (also known as diffusion flames) are flames in which the fuel and oxidizer mix in the reaction zone through molecular or turbulent diffusion [5–7, 9, 11]. The structure of non-premixed flames depends on the flow configuration of the reactants. In this type of flame, the fuel could either be a condensed matter such as solid and liquid, or a gaseous stream, while the oxidizer is either a gaseous flowing stream or the quiescent atmosphere. The burning rate of the flame depends on the rate of mixing of the fuel and oxidizer in the reaction zone [11].

Although flames are classified based on the mixing characteristics of the reactant species, typical non-premixed flames differ in accordance to the relative position of the oxidizer and fuel. In this regard, non-premixed flames could be a jet flame, co-flowing flame, or counter-flow flame. In a jet flame, the fuel flows axially into the quiescent stagnant oxidizer (air). Co-flowing flames occur when the oxidizer and the fuel flow concentrically in the axial direction as shown in Figure 1.5.. Further, counter-flow flames are generated when the fuel and oxidizers flow in the opposite direction towards each other axially. Counter-flow flames could be referred to as stagnation flames because the flames are formed on the stagnation plane of the flow.

In a coflowing flame configuration, the radial distribution of the species concentration which shows the structure of flame at a specified height is shown in Figure 1.6.. This is due to the interdiffusion of reactants and products in the reaction zone. Theoretically, the reaction zone is the region within the domain where the fuel and oxidizer react at stoichiometric proportions. This theoretical proposition led to the first theoretical analysis of diffusion flames conducted by Burke and Schumann [5, 6, 9, 12, 13].

Non-premixed flames are characterized by the rate of mixing of the reactants rather than the rate of chemical reactions, because the rate of chemical reaction is faster than the rate of reactant mixing by diffusion. The characteristics of non-premixed flames in

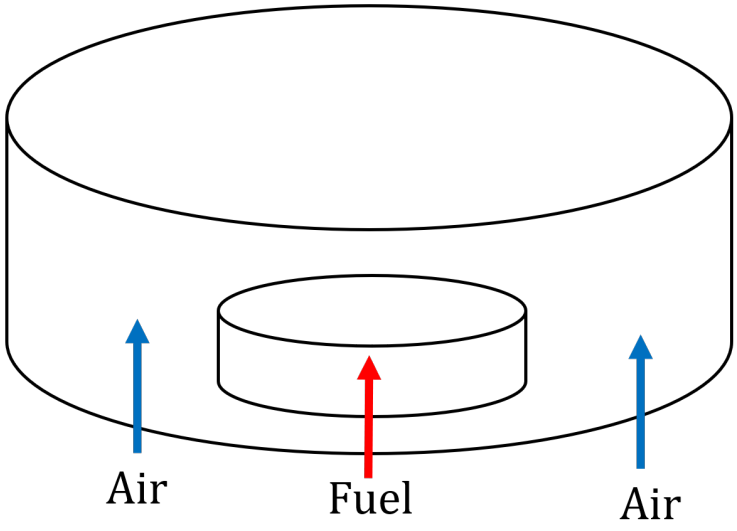

Figure 1.5. Coflowing non-premixed flames

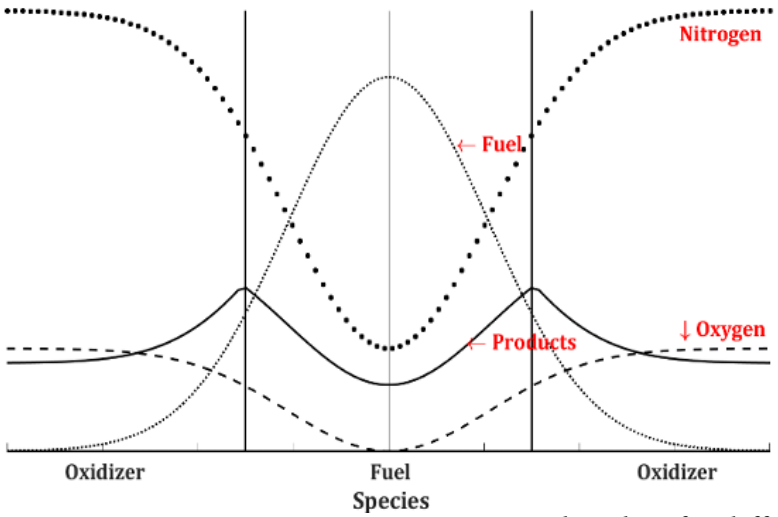

Figure 1.6. Species concentration variation at a given height of a diffusion flame

relation to the mixing properties of the reactants could be described by a dimensionless parameter called Damköhler number ($\mathcal{D}a$). The Damköhler number ($\mathcal{D}a$) is defined as the ratio of the rate of chemical reaction to the rate of mixing of the species by diffusion [12]:

$$\mathcal{D}a = \frac{\text{Rate of Chemical Reaction}}{\text{Rate of Species Mixing by diffusion}} = \frac{\text{Characteristic Mixing Time}}{\text{Characteristic Chemical Reaction Time}} = \frac{\tau_d}{\tau_{ch}} \quad (1.8.)$$

In non-premixed flames, the rate of chemical reaction is much faster than the rate of species mixing. Thus, the characteristic chemical reaction time (τ_{ch}) is much smaller than the characteristic mixing time (τ_d). This implies a high Damköhler number ($\mathcal{D}a \gg 1$). As a result, there is a narrow reaction zone near the interface between gaseous fuel and oxidizer. The concentration of the reactants is low in the reaction zone, and the rate of combustion is controlled by the rate of diffusion of the reactants towards the reaction zone.

Following the discussion described in the previous section, co-flowing non-premixed flames could further be classified according to the flow configurations of the fuel and oxidizer as shown in Figure 1.2..

1.3.1. Governing Equations of Co-Flowing Non-Premixed Flames

In coflowing non-premixed flames, the fuel (C_3H_8) stream discharges into an oxidizer (air) stream flowing into a combustion region such that they are concentric to each other as shown in Figure 1.5.. The radius of the fuel stream flow is R_f and the radius of the tube carrying the oxidizer stream is R_o such that the hydrodynamic radius of the oxidizer stream is $R_{hyd} = (R_o - R_f)$.

This combustion system is modeled as an axisymmetric system. Since the flow of the reacting gases is assumed to be in the laminar regime of the flow, this flame would be considered laminar. Thus, the conservation equations governing the chemical reacting fluid flow are given in cartesian tensor notation as [9, 12, 14]:

Continuity Equation:

$$\frac{\partial \rho}{\partial t} + \frac{\partial (\rho u_i)}{\partial x_i} = 0 \tag{1.9.}$$

Momentum Equation:

$$\rho\left[\frac{\partial u_i}{\partial t} + u_j \frac{\partial u_i}{\partial x_j}\right] = -\frac{\partial P_{ij}}{\partial x_j} + \frac{\partial \tau_{ij}}{\partial x_j} + \rho \sum_{k=1}^{N} (Y_k f_k)_i \tag{1.10.}$$

Energy Equation:

$$\rho\frac{\partial e_t}{\partial t}+\rho u_i\frac{\partial e_t}{\partial x_i}=-\frac{\partial q_i}{\partial x_i}+\frac{\partial\left(\sigma_{ji}u_i\right)}{\partial x_j}+\rho\sum_{k=1}^{N}Y_k f_{k,i}\left(u_i+V_{k,i}\right) \tag{1.11.}$$

Species Conservation:

$$\rho\frac{\partial Y_k}{\partial t}+\rho u_i\frac{\partial Y_k}{\partial x_i}+\frac{\partial\left(\rho Y_k V_{k,i}\right)}{\partial x_i}=\dot{\omega}_k \quad for \quad k=1,2,3,\ldots N \tag{1.12.}$$

Equation of State:

$$p=\rho R_{mix}T=\rho\mathcal{R}T\sum_k\left(\frac{Y_k}{W_k}\right) \tag{1.13.}$$

where ρ is the average density, u_i is the average velocity component of the fluid mixture in each direction $i-(r,\theta,z)$, σ_{ji} is the stress tensor which comprises the hydrostatic pressure p, and the shear stress tensor τ_{ji}. Y_k and f_k are the mass fraction and body force per unit mass of the species k in the mixture respectively, V_{ki} is the components of the diffusion velocity of species k in the i direction, q_i is the heat flux due to conduction, inter-diffusion or Dufour effect, e_t is the total specific internal energy of the mixture, and $\dot{\omega}_k$ is the rate of production of species k. $\mathcal{R}$ is the universal gas constant, T is the temperature of the fluid mixture, and W_k is the molecular weight of the gaseous species k.

1.3.1.1. Constitutive Equations of Newtonian Fluids

To completely describe the governing equation of reacting flows, the constitutive equations of flow properties and physics are given as [9, 14]

The stress tensor σ_{ij} is given as:

$$\sigma_{ij}=-P_{ij}+\tau_{ij}=-pI_{ij}+\mu\left[\left(\frac{\partial u_i}{\partial x_j}\right)+\left(\frac{\partial u_j}{\partial x_i}\right)\right]-\frac{2}{3}\mu\left(\frac{\partial u_i}{\partial x_j}\delta_{ij}\right) \tag{1.14.}$$

Here, the pressure tensor $P_{ij}=pI_{ij}$, where I_{ij} is the unit tensor, p is the hydrostatic

pressure of the combustion system, and μ is the fluid dynamic viscosity.

The total specific internal energy e_t of the fluid mixture is given as:

$$e_t = e + \frac{1}{2}\mathrm{U}^2 \tag{1.15.}$$

U is the average fluid mixture velocity magnitude.

From thermodynamics, the specific internal energy e is given as

$$e = h - \frac{p}{\rho} = \sum_{k=1}^{\mathrm{N}} h_k \mathrm{Y}_k - \frac{p}{\rho} \tag{1.16.}$$

h is the specific enthalpy of the fluid mixture, and h_k is the specific enthalpy of the $k-th$ gaseous species in the mixture.

The heat flux q_i of the energy equation given above is due to conduction, radiation, diffusion and Dufour effect of the heat energy transferred. The constitutive equation of the heat flux is given as:

$$q_i = -\lambda \frac{\partial \mathrm{T}}{\partial x_i} + \rho \sum_{k=1}^{\mathrm{N}} h_k \mathrm{Y}_k \mathrm{V}_{k,i} + \mathcal{R}\mathrm{T} \sum_{k=1}^{\mathrm{N}} \sum_{j=1}^{\mathrm{N}} \left[\frac{\chi_j \mathcal{D}_{\mathrm{T}k}}{\mathrm{W}_k \mathcal{D}_{kj}} \right] \left(\mathrm{V}_{k,i} - \mathrm{V}_{j,i} \right) + q_{i,rad} \tag{1.17.}$$

$\mathrm{V}_{k,i}$ and $\mathrm{V}_{j,i}$ are the diffusion velocity of the $k-th$ and $j-th$ species of the fluid mixture respectively, W_k is the molecular weight of the $k-th$ species, $\mathcal{D}_{\mathrm{T}k}$ is the Soret diffusivity coefficient, $\mathcal{D}_{kj}$ is the concentration diffusivity of $k-th$ species in $j-th$ species, χ_j is the mole fraction of species j, λ is the thermal conductivity of the fluid mixture.

1.3.2. Flame Sheet Theory of Laminar Non-Premixed Flames

The theoretical quantification of non-premixed flames was first introduced by Burke and Schumann [9, 13, 15, 16]. This theory was based on the assumption that the chemical reaction zone of a non-premixed flame is infinitely thin. This approximation is also known as the flame sheet approximation.

For simplicity, non-premixed flames are usually analyzed theoretically by approximating the chemical reaction rate as an infinitely fast chemical reaction rate. This implies that the reaction zone is a plane or sheet. The factors controlling the combustion process in this scenario are the stoichiometric rate of transport of fuel and oxidizer.

Burke and Schumann considered a system in which fuel and air flow with the same constant velocity through coaxial cylindrical tubes and the oxidizer is on the outside. Based on the results obtained, non-premixed flames could be classified as either over-ventilated or under-ventilated flames. Over-ventilated flames occur when the available oxidizer (air) exceeds the required amount for complete combustion of the fuel. The boundary of this type of flame converges to the axis of the flow. Under-ventilated flames occur when the air supply is insufficient for a complete consumption of the fuel. The boundary of the flame expands to the outer wall of the flow [9].

In Burke-Schumann's approximation, axial diffusion is assumed to be negligible in comparison to radial diffusion $\left(\partial^2 \mathrm{Y}_j/\partial r^2 \gg \partial^2 \mathrm{Y}_j/\partial z^2\right)$; the velocities of oxidizer and fuel are constant, equal and uniform in the whole fluid zone; mixing is due to radial diffusion; and reactions occur at the stoichiometric condition ($\phi = 1$).

Based on these assumptions, the governing equations given in the previous subsection reduce to the following:

Species Conservation:

$$\frac{\rho\mathcal{D}}{r}\frac{\partial}{\partial r}\left(r\frac{\partial \mathrm{Y}_j}{\partial r}\right) - \rho v_z \frac{\partial \mathrm{Y}_j}{\partial z} = \dot{\omega}_j \tag{1.18.}$$

Energy Conservation:

$$\frac{\lambda}{c_p}\frac{1}{r}\frac{\partial}{\partial r}\left[r\frac{\partial\left(c_p \mathrm{T}\right)}{\partial r}\right] - \rho v_z \frac{\partial\left(c_p \mathrm{T}\right)}{\partial z} = -\dot{\omega}_{\mathrm{F}}\Delta \mathrm{H}_r = -\dot{\omega}_{ox}\Delta \mathrm{H}_r \tag{1.19.}$$

$\mathcal{D}$ is the species diffusivity, Y_j is the mass fraction of species j, ρ is the bulk mixture

density, v_z is the axial velocity, c_p is the specific heat capacity of the mixture, $\dot{\omega}_j$ is the rate of consumption of species j, $\dot{\omega}_F$, $\dot{\omega}_{ox}$ are the rates of consumption of fuel and oxidizer respectively, and T is the temperature of the mixture.

Although this analysis computed the flame height of non-premixed flames generated from concentric circular port to some accuracy, this analysis failed to accurately compute the flame height of non-premixed flames generated from non-circular port. As a result, the flame sheet approximation has been considered as the first approximation for a more accurate computation of non-premixed flame characteristics [13].

To improve the computation conducted by Burke and Schumann, a finite rate chemical reaction of the combustion species is required. As a result, the reaction zone of the combustion species has a finite thickness.

1.3.3. Finite Rate Theory of Non-Premixed Flames

To analyze non-premixed flames in most practical combustion system, a more realistic theory - finite rate theory was proposed. This theory modified the Burke and Schumann's approach by considering a finite chemical reaction rate, which resulted in a finite reaction zone for combustion. In the finite rate theory, the velocity of the reactants is no longer constant and uniform but ensures that the continuity and momentum conservation equations are satisfie. Also, the pressure could vary as the combustion products flow [9].

1.3.3.1. Assumptions of Co-flow Non-Premixed Flames

In order to solve the governing equations of a laminar non-premixed flame using the finite rate theory to describe the flame characteristics, a steady state fluid flow could be assumed while neglecting the diffusion of the chemical species due to pressure gradients, gravity forces and Soret diffusion. To compute the diffusion velocity of the chemical species, the effect of pressure gradients, force of gravity, and temperature gradients could be neglected. These assumptions would reduce the Stefan - Maxwell

relation for diffusion velocity to:

$$\mathrm{V}_{k,i} = -\mathcal{D}_{k\mathrm{N}} \frac{\partial(\ln(\mathrm{Y}_k))}{\partial x_i} \tag{1.20.}$$

Although some heavy gaseous species present in the combustion process radiate thermal energy by virtue of their temperature, the effect of radiation heat transfer is neglected for simplicity. This assumption over-predicts the temperature distribution within the flame. The heat flux q_i which affects the combustion process is expressed as:

$$q_i = -\lambda \frac{\partial \mathrm{T}}{\partial x_i} + \rho \sum_{k=1}^{\mathrm{N}} h_k \mathrm{Y}_k \mathrm{V}_{k,i} \tag{1.21.}$$

If viscous heating is neglected, the rate of work done by virtue of the flow becomes:

$$\frac{\partial\left(\sigma_{ji} u_i\right)}{\partial x_j} = p \frac{\partial u_i}{\partial x_i} \tag{1.22.}$$

Based on the above stated assumptions, the equations governing laminar co-flow non-premixed flames using finite rate theory are given as:

Continuity Equation

$$\frac{\partial(\rho u_i)}{\partial x_i} = 0 \tag{1.23.}$$

Momentum Equation

$$\rho u_j \frac{\partial u_i}{\partial x_j} = -\frac{\partial p}{\partial x_i} + \mu \frac{\partial^2 u_i}{\partial x_j^2} + \left(\mu - \frac{2}{3}\mu\right) \frac{\partial}{\partial x_i}\left(\frac{\partial u_j}{\partial x_j}\right) + \rho \sum_{k=1}^{\mathrm{N}} (\mathrm{Y}_k f_k)_i \tag{1.24.}$$

Energy Equation

$$\frac{\partial(\rho u_i h^s)}{\partial x_i} - \frac{\partial}{\partial x_i}\left(\rho \sum_{k=1}^{\mathrm{N}} h_k^s \mathcal{D}_{k\mathrm{N}} \frac{\partial \mathrm{Y}_k}{\partial x_i}\right) - \frac{\partial}{\partial x_i}\left(\lambda \frac{\partial \mathrm{T}}{\partial x_i}\right) = u_i \frac{\partial p}{\partial x_i} - \sum_{k=1}^{\mathrm{N}} h_k^0 \dot{\omega}_k \tag{1.25.}$$

Species Conservation

$$\rho \frac{\partial Y_k}{\partial t} - \mathcal{D}_{k\mathrm{N}} \frac{\partial Y_k}{\partial x_i} = \dot{\omega}_k \qquad for \quad k = 1, 2, 3, \ldots \mathrm{N} \tag{1.26.}$$

where $\mathcal{D}_{k\mathrm{N}}$ is the average diffusion coefficient of species k, h_k^0 and h_k^s are the standard state enthalpy of formation and sensible enthalpy of species k respectively.

Using this approach, the region of the flame where fuel and oxidizer co-exist without complete reaction is captured over a finite length of the flame region.

1.4. Overview of Soot Formation

Combustion processes have been beneficial in diverse ways, but they generate hazardous by-products, for example soot and CO, which have harmful effect on the environment and human health [11, 17]. Although soot formation results in reduction in combustion efficiency, soot has been connected to the hazardous health issues affecting humans. However, in industrial furnaces and heat generators, soot formation is needed so as to enhances heat transfer by radiation. To avoid the health hazards posed by soot, the formed soot is oxidized before the exhaust are released into the environment. Also, soot are used in chemical industries for a wide range of applications such as filler in tires, toner in copiers, or printing colors [17–19].

The formation of soot results from incomplete combustion of hydrocarbons, thus reducing the combustion efficiency of a combustion system. The formation process of soot from gaseous hydrocarbons consists of the following steps: thermal fuel decomposition, nucleation, surface growth, coagulation and oxidation [17, 18].

1. Thermal fuel decomposition: This involves the decomposition of a hydrocarbon fuel into smaller hydrocarbons such C_2H_2 and other elementary species due to the heat.

2. Nucleation: This is the process of forming solid particles from the gaseous species. This process is called nucleation because solids are formed naturally

from small particles called nuclei. The nucleation process is assumed to begin with the formation of polyacetylene [17, 20].

3. Surface growth: As gaseous species collide with the formed nuclei, they interact with each other resulting in the formation of more particles in the process.

4. Coagulation: As more nuclei are formed during the nucleation and growth process, they migrate towards each other and collide. This collision results in coalescing of the particles if the energy of collision is comparable to the binding energy of the nuclei. As a result, the size of the soot nuclei increases.

5. Oxidation: This process occurs when soot particles migrate towards an oxidizing species of the reacting mixture.

Generally, the amount of soot emitted by a combustion system can be reduced by providing more oxidizing species that would oxidize the soot before it is released into the environment [17].

1.5. Overview of Magnetic Effects

This section gives an overview of magnetism, and the various types of magnetic materials used in the application of magnetism.

Although electric fields **E** are produced by stationary electric charges, magnetic fields **B** are produced by either moving electric charges or materials that possess intrinsic elementary particles such as electron that possess magnetic dipoles [21]. These materials which could be used to generate magnetic fields are referred to as magnetic materials i.e. they possess the intrinsic electrons which could be oriented in a given direction in the presence of a magnetic field.

1.5.1. Classification of Magnetic Materials

Magnetic materials possess electrons which have an "orbital" magnetic dipole moment and a spin magnetic dipole moment. These dipole moments combine

vectorially to produce magnetic fields in the material. Magnetic materials are classified based on the type of magnetism they possess. In general, there are three basic classes of magnetism: Diamagnetism, Paramagnetism, and Ferromagnetism. Based on this classification of magnetism, magnetic materials are generally classified as diamagnetic materials, paramagnetic materials, and ferromagnetic materials [21].

Diamagnetism occurs when an external magnetic field $\mathbf{B}_{ext}$ induces a weakly magnetic dipole moment in the magnetic material which acts in opposition to the applied external magnetic field $\mathbf{B}_{ext}$. In the absence of the external magnetic field, the induced magnetic field will be absent. If a diamagnetic material is exposed to a non-uniform magnetic field, the diamagnetic material is repelled from the region of higher magnetic field towards the region of lower magnetic field. Examples of diamagnetic materials are most gases such as nitrogen, hydrogen, carbon dioxide [21].

Paramagnetism is exhibited by materials which have a resultant induced magnetic dipole moment in the direction of the applied external magnetic field $\mathbf{B}_{ext}$. In the absence of the external magnetic field $\mathbf{B}_{ext}$, the dipole moments are randomly oriented in the material which results in no resultant magnetic field. In the presence of an external magnetic field $\mathbf{B}_{ext}$, paramagnetic materials generate resultant magnetic dipole moments in the direction of the applied magnetic field $\mathbf{B}_{ext}$. If the external magnetic field $\mathbf{B}_{ext}$ is non-uniform, the paramagnetic materials are attracted towards the region of higher magnetic field from the region of lower magnetic field. Examples of paramagnetic materials are transition elements, rare earth elements, oxygen gas molecules [21].

Ferromagnetic Materials exhibit ferromagnetism. Ferromagnetism occurs when the electrons of materials have strong resultant magnetic dipole moments aligned in the direction of an external magnetic field $\mathbf{B}_{ext}$. These resultant magnetic dipole moments are retained by ferromagnetic materials, thus become a permanent magnet [21].

1.5.2. Magnetic Fields

When a magnetic material is placed in the vicinity of a charged particle q moving with velocity $\mathbf{v}$. The magnetic material experiences a force $\mathbf{F}_{mag}$ due to the magnetic field $\mathbf{B}$. The magnetic field $\mathbf{B}$ is orthogonal to the direction of the exerted force $\mathbf{F}_{mag}$ and velocity $\mathbf{v}$ [21]. As a result, the magnitude of the magnetic field $\mathbf{B}$ is defined as [21]:

$$\mathrm{B} = \frac{\mathrm{F}_m}{|q|v} \tag{1.27.}$$

Thus, the magnetic force $\mathbf{F}_m$ is given as:

$$\mathbf{F}_{mag} = q\mathbf{v} \times \mathbf{B} \tag{1.28.}$$

Magnetic fields are generated around a current carrying conductor according to Ampere's theorem. For a long straight wire carrying current I[A], Biot and Savart's law defines the magnetic field $\mathbf{B}$ at a perpendicular distance R as [21]:

$$\mathrm{B} = \frac{\mu_{m,0}\mathrm{I}}{2\pi\mathrm{R}} \tag{1.29.}$$

According to Ampere's law, when two conductors carry current in the same direction, they attract each other. However, when the conductors carry current in opposite direction, they repel each other. The force acting on the conductors as shown in Figure 1.7. is given as [21]:

$$\mathbf{F}_{ba} = i_b\mathbf{L} \times \mathbf{B}_a \tag{1.30.}$$

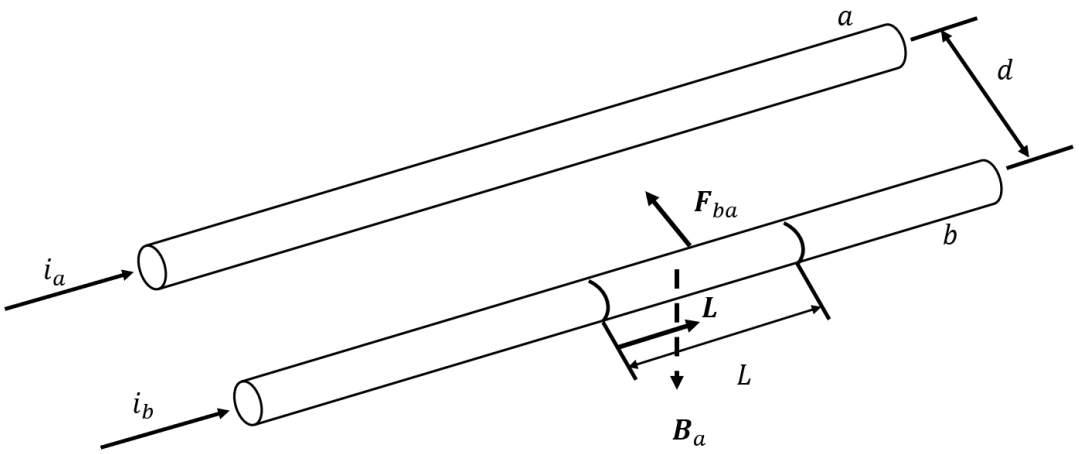

Figure 1.7. Two current carrying conductors in the same direction

1.6. Maxwell's Equation of Electromagnetism

The mathematical model that describes electromagnetic phenomena which involves electric and magnetic fields are known as Maxwell's equations. These equations describe the relationship between electric charges and electric fields or electric current and magnetic fields. The equations are [22–24]:

Gauss' Law for Electricity:

$$\nabla \cdot \mathbf{D} = \rho_c \tag{1.31.}$$

Ampere - Maxwell's Law:

$$\nabla \times \mathbf{H} - \frac{\partial \mathbf{D}}{\partial t} = \mathbf{J} \tag{1.32.}$$

Faraday's Law:

$$\nabla \times \mathbf{E} + \frac{\partial \mathbf{B}}{\partial t} = 0 \tag{1.33.}$$

Gauss' Law for Magnetism:

$$\nabla \cdot \mathbf{B} = 0 \tag{1.34.}$$

where, **H** is the magnetic field (A/m), **B** is the magnetic field induction (T), **E** is the

electric field (V/m), **D** is the electric field displacement or electric flux density $\left(C^2/m\right)$, **J** is the current density $\left(A^2/m\right)$, and ρ_c is the electric charge density $\left(C/m^3\right)$.

Although electromagnetic phenomena could involve both electric fields and magnetic fields, the physical phenomena considered in this work are predominantly magnetic fields (magnetism) which are governed by Equation 1.32. and Equation 1.34.. As such, magnetic field analyses are classified based on the type of analysis being performed as either Magnetostatics or Transient/Harmonic Analysis.

Magnetostatics involves static analysis of magnetic fields generated predominantly by permanent magnets, steady flow of DC current, or applied external field. To study the effect of magnetic fields on common pollutants generated by non-premixed flames, the non-premixed flames would be exposed to magnetic fields generated by either permanent magnets or by a DC source. Thus, a magnetostatic analysis is conducted to compute the magnetic field distribution which would be imposed on the non-premixed flames during combustion numerically.

In order to solve Maxwell's equations given above, a constitutive relationship between the magnetic field induction, magnetic field strength and magnetization properties is required for a complete description of the physical problem.

1.6.1. Constitutive Magnetic Relations

The intrinsic relationship between the Magnetic field induction **B**, magnetic field strength **H**, and the Magnetization vector **M** for any magnetic material [23].

$$\mathbf{B} = \mu_{m,0}\left(\mathbf{H} + \mathbf{M}\right) \tag{1.35.}$$

The magnetic susceptibility χ_m is expressed as $\chi_m = \frac{\mathbf{M}}{\mathbf{H}}$. Although the mass magnetic susceptibility of a diamagnetic material is independent of the absolute temperature, the mass magnetic susceptibility of a paramagnetic substance is dependent on absolute temperature. According to the Curie-Weiss law, the mass

susceptibility of the paramagnetic substance is expressed as a function of absolute temperature T as [23, 25]:

$$\chi_m = \frac{C_w}{T} \tag{1.36.}$$

For diamagnetic substance, $\chi_m < 0$, and for paramagnetic substance $\chi_m > 0$.

Since the magnetic susceptibility χ_m of a material is defined as the ratio of magnetization vector **M** to magnetic field strength $\vec{H}$, the constitutive relation given above can be expressed as:

$$\mathbf{B} = \mu_{m,0}(1 + \chi_m)\mathbf{H} \tag{1.37.}$$

1.7. Magnetic Body Force

When a paramagnetic fluid flows in the vicinity of a magnetic field **B**, the magnetic body force density $\mathbf{f}_{mag}$ is given by Equation 1.38. [23]. A detailed derivation of the magnetic body force acting on paramagnetic fluids is provided in Appendix 6.1..

$$\mathbf{f}_{mag} = \nabla \cdot \left(\frac{1}{2} \mu_m H^2 \mathbf{I} \right) \tag{1.38.}$$

where **I** is the unit Tensor.

1.8. Objectives and Dissertation Outline

1.8.1. Objectives

Since the characteristics of non-premixed flames are affected by the presence of magnetic fields, the objectives of this research is to study the effect of magnetic fields on pollutants - soot and CO generated by non-premixed flames. In this regard, the effect of the location of the flame burner tip in the magnetic fields on the pollutants is studied. In addition, the effect of the size of the magnetic field imposed on the pollutants is studied.

1.8.2. Structure of the Dissertation

This dissertation contains six chapters. Chapter 2. presents some of the published literature on soot formation and the effect of magnetic fields on characteristics (flame

temperature, flame lift-off height) of non-premixed flames.

Chapter 3. discusses the computational approach used in modeling non-premixed flames numerically using a finite volume method. It presents the modeling of the flame characteristics of a non-premixed flame and the modeling of soot formation. The chapter concludes with the computation of magnetic fields.

Chapter 4. discusses the effect of infinitely wide permanent magnetic fields on CO and soot formation in propane - air non-premixed flames. Chapter 5. discusses the effect of the magnetic field of a solenoid coil on CO and soot formation in propane - air non-premixed flames. In addition, the impact of the flame size on the magnetic field effect is discussed.

Finally, Chapter 6. concludes the dissertation with a summary of the computational results obtained and a proposed future research.

Chapter 2.
Literature Review

2.1. Modeling of Soot Formation

Theoretically, combustion of hydrocarbons results in the formation of only CO_2 and H_2O for a stoichiometric composition of fuel and oxidizer as shown in Equation 1.3.. However, in practical combustion systems such as industrial furnaces, gas turbines, and internal combustion engines, conditions deviate from the ideal condition described. This deviation is the result of the formation of other chemical species which are emitted as products of the combustion reaction. Some of these chemical species are minor species that may only exist for a short duration, while others are major species due to the relative large amount within the products. The most common major chemical species are CO_2, H_2O, CO, NO_x, and soot [19].

The soot formation process is complex and requires a detailed understanding of the physical process to be modeled mathematically. This complexity stems from the fact that particulate matters are generated from gaseous species. Most combustion processes involve the chemical reaction of gaseous species, but soot being a particulate matter is also one of the constituents by-products of the gaseous chemical reaction. This complicates the modeling of soot formation process.

In order to understand the process of soot formation, some researchers have proposed that soot precursors are acetylene (C_2H_2), polyacetylene, allene, butadiene, polyaromatic hydrocarbons(PAH). Among those, PAH have been found to be the most common soot precursors according to most experimental, thermodynamic and kinetic evidence [26]. Although soot formation is common to both types of flames – premixed and non-premixed, the process of soot formation is slightly different. The formation of soot precursors in premixed flames involves both fuel pyrolysis and oxidation reactions. These competitive reactions affect the formation of soot from these precursors. However, in non-premixed flames, soot precursors are formed during the

fuel pyrolysis in the absence of an oxidation reaction [27].

Although the formation of soot precursors in non-premixed flames involves only fuel pyrolysis, the dynamics of soot formation in various classes of non-premixed flames differ. In normal diffusion flames, the combustion products in the fuel stream side such as the fuel, soot precursors and other constituents are subject to convection and molecular diffusion towards the flame front. The convection process dominates the motion of the combustion products because the fuel stream motion supports the convection process. In counter-flow diffusion flames, the motion of the products in the fuel region of the flame is dominated by molecular diffusion across the stagnation streamline of the flow. In counter-flow flames, the soot particles reside only on the fuel side of the flame front, and are thus not oxidized. Similarly, in inverse diffusion flames, the convection of the soot precursors and combustion products on the fuel region are directed away from the flame zone [27].

2.1.1. Soot Formation Process

Generally, the formation of soot involves four major chemical processes [26]:

- Initial soot precursor formation
- Particle Nucleation / HACA
- Particle growth by coagulation
- Surface reactions of the cluster of particles

2.1.1.1. Initial soot precursor formation

The formation of soot from the gaseous C_2H_4 starts with the pyrolysis of the fuel which results in the formation of the initial soot precursors such as C_2H_2, polyacetylenes, allene, butadiene, and PAH. The process depends on the temperature range of the reaction. In particular, the high temperature reaction path involves [26]:

- The formation of vinylacetylene.

$$C_2H_3 + C_2H_2 \rightarrow [C_4H_5]^{\#} \rightarrow C_4H_4 + H \tag{2.1.}$$

- The addition of acetylene C_2H_2 to nC_4H_3:

$$C_4H_4 + H \rightarrow nC_4H_3 + H_2 \tag{2.2.}$$

$$C_2H_2 + C_4H_3 \rightarrow C_6H_5 \tag{2.3.}$$

- Hydrogen abstraction:

$$C_6H_5 + H_2 \rightleftharpoons C_6H_6 + H^+ \tag{2.4.}$$

At low temperature, the reaction path would involve:

- The formation of vinylacetylene:

$$C_2H_3 + C_2H_2 \rightarrow C_4H_5 \tag{2.5.}$$

- Formation of Benzene:

$$C_4H_5 + C_2H_2 \rightarrow C_6H_6 + H^+ \tag{2.6.}$$

- Hydrogen abstraction reaction:

$$C_6H_6 + H^+ \rightarrow C_6H_5 + H_2 \tag{2.7.}$$

2.1.1.2. Particle Nucleation

Following the formation of the initial benzene ring, the aromatic ring grows by a two-step process: H-abstraction and acetylene addition. Frenklach and Wang [26] called this reaction process H-abstraction-C_2H_2-addition (HACA) reaction. The reaction of the benzene ring with other chemical species other than acetylene dominates the growth

process, which relaxes to the HACA mechanism as the concentration of the acetylene (C_2H_2) is comparable to the benzene concentration [26]. The proposed reaction scheme for the growth of PAH from the initial benzene ring is given as:

$$A_i + H \rightleftharpoons A_i* + H_2 \tag{2.8.}$$

$$A_i* + C_2H_2 \rightleftharpoons A_iC_2H_2* \tag{2.9.}$$

$$A_iC_2H_2* + C_2H_2 \rightleftharpoons A_{i+1} + H \tag{2.10.}$$

where A_i denotes an aromatic molecule containing i fused aromatic rings, A_i* is an aromatic radical formed by hydrogen abstraction, and $A_iC_2H_2*$ is the radical formed by acetylene addition.

2.1.1.3. Particle growth by coagulation

After the formation of polyaromatic hydrocarbons (PAH) takes place, these particles move randomly in accordance to Brownian motion. During this movement, they collide with each other and coagulate to form a bigger mass. This coagulation process affects the number of available PAH but increases the mass of soot formed during the combustion process.

2.1.1.4. Surface reactions of particle clusters

Although the mass of soot formed increases with coagulation, the mass of soot rejected as exhaust of the combustion depends on the nature of surface reaction taking place after the formation of the soot particles. The actual nature and type of surface reaction in most combustion processes is uncertain due to the large number of chemical species available in a combustion process. However, the popular consensus of the most common chemical species reacting with soot particles are O_2, OH, C_2H_2, H^+, and PAH. Appel et al. [28] presented the chemical reaction mechanism for the common soot surface reaction as presented in Table 2.1. below.

Table 2.1. Soot surface growth mechanism

No.	Reaction	A $\left[\mathrm{cm}^3/\mathrm{kmol}-\mathrm{s}\right]$	n	E$[kCal/\mathrm{kmol}]$
S1	$C_s - H + H \rightleftharpoons C_s^* + H_2$	4.3×10^{13}		13.0
S2	$C_s - H + OH \rightleftharpoons C_s^* + H_2O$	1×10^{10}	0.734	1.43
S3	$C_s^* + H \rightarrow C_s - H$	2×10^{13}		
S4	$C_s^* + C_2H_2 \rightarrow C_s - H + H$	8×10^{7}	1.56	3.8
S5	$C_s^* + O_2 \rightarrow 2CO + products$	2.2×10^{12}		7.5
S6	$C_s - H + OH \rightarrow CO + products$			

2.1.2. Soot Formation Model

Due to the lack of concrete evidence of the actual chemical reaction path to the formation of soot, soot models provided in literature have been classified broadly into [29]:

- Empirical models
- Semi-Empirical Models
- Detailed Chemical Models

2.1.2.1. Empirical Models

This class of models compute the amount of soot produced by the combustion of certain fuel from correlation obtained from other experimental studies. This class of model is used in complex problems where detailed models are computationally intractable. In this model, certain critical parameters are used to estimate the relative proportion of soot.

In premixed flames, such parameters are critical or threshold Equivalence ratio ϕ_c. However, in diffusion flames, the soot emission from a flame has been estimated to depend on flame height. The sooting tendencies of fuels and mixture is measured by the Threshold Sooting Index (TSI) [30].

$$\mathrm{TSI} = a - b\phi_c \tag{2.11.}$$

where (a, b) are apparatus dependent constants and ϕ_c is the threshold equivalence ratio.

Based on empirical results, Khan et al.[31] proposed a soot model for diesel engines. This model is based on the size of soot particles from engines operated at different speeds with constant load. This model assumes that the rate of soot inception is the major factor affecting the rate of soot formation and growth. A general soot model was proposed as

$$\frac{dC_s}{dt} = c\left(\frac{V_u}{V_{NTP}}\right)P_u\phi_u^n \exp\left(\frac{-E}{R_u T}\right) \tag{2.12.}$$

The soot mass loading is C_s (kg/m^3), a modeling parameter is c , volume of the soot formation zone is V_u (m^3), volume at normal temperature and pressure of the cylinder contents is V_{NTP} (m^3), partial pressure of unburned fuel is P_u (Pa), unburned equivalence ratio ϕ_u, activation energy E and local temperature T(K).

The modeling parameters c, n, and E are calibrated with an injection diesel engine [29].

2.1.2.2. Semi-Empirical Models

This model incorporates some the soot formation and growth physics during the modeling process. Tesner et al. [32] used a simple kinetic model to interpret the soot particle formation measurements in an acetylene-hydrogen flame. This model is a two-step mechanism that described the rate of soot nuclei n formation which is given as [32]

$$\frac{dn}{dt} = n_0 + (f - g)n - g_0 N n \tag{2.13.}$$

The temperature dependent rate of generation of nuclei is n_0, f and g are branching and termination coefficients respectively, the rate of loss of nuclei due to collisions with soot particles is g_0 , the number density of soot particles is N [32].

The soot particle number density N (particles/kg – mixture) is computed using

$$\frac{d\mathrm{N}}{dt} = (a - b\mathrm{N})n \tag{2.14.}$$

Leung et al. [33], and Lindstedt [34] proposed a chemical kinetic mechanism that predicts soot formation in non-premixed flames assuming that the soot propensity depends on pyrolysis intermediates such as acetylene (C_2H_2). Assuming acetylene to be the primary soot precursor for soot nucleation, the model predicted the soot formation process in non-premixed. To compute the soot mass fraction and soot number density, two additional conservation equations were solved.

Soot nucleation is assumed to start with the pyrolysis process which results from the breakdown of fuel. In this regard, acetylene acts as the soot precursor to obtain a first approximation. The nucleation process is given by the reaction:

$$\mathrm{C_2H_2} \rightarrow 2\mathrm{C}_s + \mathrm{H_2} \tag{2.15.}$$

The initial soot particle formed during the nucleation process is assumed to contain 100 carbon atoms which resulted in a particle size of about 1.24nm. The activation temperature $\left(\frac{\mathrm{E}}{\mathcal{R}}\right)$ was found to be around 21 100 K to form the incipient soot particles and initiate surface growth.

Assuming a first order reaction, the rate of nucleation is computed using

$$\mathrm{R}_1 = 10^4[\mathrm{C_2H_2}]\exp\left(-\frac{21100}{\mathrm{T}}\right)\left[\mathrm{kgmol/m^3 s}\right] \tag{2.16.}$$

where $[\mathrm{C_2H_2}]$ is the concentration of acetylene $\left[\mathrm{kmol/m^3}\right]$.

The surface growth due to adsorption of C_2H_2 by the soot particles is governed by

the soot formation reaction given by

$$C_2H_2 + nC_s \rightarrow (n+2)C_s + H_2 \tag{2.17.}$$

For a first order reaction, the rate of surface growth is computed by

$$R_2 = k_2(T) f(S)[C_2H_2] \tag{2.18.}$$

where the acetylene molar concentration is $[C_2H_2]$ $\left(\text{kmol/m}^3\right)$, surface area per unit volume of soot is S $\left(\text{m}^2/\text{m}^3\right)$.

The surface area per unit volume of soot is computed as

$$S = \pi d_p^2(\rho N) = \pi\left(\frac{6}{\pi}\frac{1}{\rho_{C_s}}\frac{Y_{C_s}}{N}\right)^{\frac{2}{3}}(\rho N) \tag{2.19.}$$

The particle diameter d_p is then computed by

$$d_p = \left(\frac{6}{\pi}\frac{1}{\rho_{C_s}}Y_{C_s}N\right)^{\frac{1}{3}} \tag{2.20.}$$

and the surface area per unit volume dependency of the soot formation process is computed by

$$f(S) = \sqrt{\pi\left(\frac{6M_{C_s}}{\pi\rho_{C_s}}\right)^{\frac{2}{3}}} \times [C_s]^{\frac{1}{3}}[\rho N]^{\frac{1}{6}} \qquad \left[\text{kmol/m}^3\text{s}\right] \tag{2.21.}$$

where $[C_s] = \left[\frac{\rho Y_{C_s}}{M_{C_s}}\right]^{\frac{1}{3}}$, N [particles/kg − mixture], species k mass fraction is Y_k, molar mass of soot is $M_{C_s} = 12.011\,\text{kg/mol}$.

The rate constant of the surface growth $k_2(T)$ can be computed using

$$k_2(T) = 0.6 \times 10^4 \exp\left(-\frac{12100}{T}\right) \tag{2.22.}$$

and the oxidation reaction of soot was assumed to be calculated by

$$\mathrm{C}(s) + \frac{1}{2}\mathrm{O}_2 \rightarrow \mathrm{CO} \tag{2.23.}$$

Thus, the rate of soot oxidation and rate constant are computed by

$$\mathrm{R}_3 = k_3(\mathrm{T})\mathrm{S}[\mathrm{O}_2] \qquad \left[\mathrm{kmol/m^3 s}\right] \tag{2.24.}$$

$$k_3(\mathrm{T}) = 10^4 \mathrm{T}^{\frac{1}{2}} \exp\left(-\frac{19680}{\mathrm{T}}\right) \tag{2.25.}$$

Other semi-empirical models have published in literature as listed in [29].

2.1.2.3. Soot Model with Detailed Chemistry

Mathematical models which considers empirical inputs to define soot nucleation, growth and oxidation rate are specific to fuel used during the experiments. To accommodate other possible conditions, a detailed soot model based on chemical kinetics has been proposed. Brown and Frenklach [26], Frenklach [35], Frenklach et al. [36], and Wang and Frenklach [37] used a detailed chemical mechanism to model soot formation, growth and oxidation.

In accordance to the soot formation process described in the previous section, Brown and Frenklach modeled the soot growth process by a linear lumping of the change in moment distributions of the soot incipient particle concentration and size. This considers the propensity of forming soot incipient particles during the combustion process.

The $k-th$ moment of the soot particle concentration was defined as:

$$\mathrm{M}^k = \sum_{i=1}^{\infty} m_i^k \mathrm{N}_i \tag{2.26.}$$

where the $k-th$ concentration moment is $\mathrm{M^k}$, mass of PAH species of class i is m_i^k, and number concentration of the same size class is N_i.

Other than using the concentration moment M^k to describe the evolution of soot incipient particles, the $k-th$ size moment of the incipient species could be used. The $k-th$ size moment of the PAH distribution is defined as:

$$\mu_k = \frac{M^k}{M^1} \tag{2.27.}$$

where $M^1 = \sum_{i=1}^{\infty} N_i$. The mass per unit volume of the incipient species is given by the concentration moment, while the average size of the soot incipient species is given by the first size moment.

The evolution of the size distribution of soot particles using linear lumping is obtained from the following equations:

$$\frac{dM^0}{dt} = r_0 \tag{2.28.}$$

$$\frac{dM^1}{dt} = m_0 r_0 + \sum_{l=1}^{l_c} \Delta m_l R_l^{[0]} \tag{2.29.}$$

$$\frac{dM^2}{dt} = m_0^2 r_0 + \sum_{l=1}^{l_c} \Delta^{[2]} m_l R_l^0 + 2\Delta_c m \sum_{l=1}^{l_c} \Delta m_l R_l^{[1]} \tag{2.30.}$$

$$\vdots \tag{2.31.}$$

$$\frac{dM^k}{dt} = m_1^k r_1 + \sum_{j=0}^{k-1} \binom{r}{j} (\Delta_c m)^j \sum_{l=1}^{l_c} \Delta^{[r-j]} m_l R_l^{[j]} \tag{2.32.}$$

$$\Delta^{[p]} m_l = (m_l - \Delta_c m)^p - (m_{l-1} - \Delta_c m)^p \quad l = 1, 2, \ldots, l_c$$

$$\Delta_c m = \sum_{l=1}^{l_c} \Delta m_l = \sum_{l=1}^{l_c} (m_l - m_{l-1}) = m_{i+l_c} - m_i$$

where the rate of formation of the first lumped species is r_0, the number of the replicating sequence mass-addition reactions is l, the total number of replicating sequence mass addition reactions is l_c, the number of carbon atoms in the species of the

mass-addition reaction sequence is m_l, the number of carbon atoms added to the l's mass-addition reaction is Δm_l, the total number of carbon atoms added during the mass-addition replicating sequence, is $\Delta_c m$, and the flux of j-lumped reaction l is $R_l^{[j]}$ [20].

Frenklach and Wang [20] assumed that a soot particle is formed when two PAH molecules combine to form a dimer. However, to describe other formation processes such as surface growth, the hydrogen addition and carbon abstraction (HACA) assumption is used to describe the process. The reactions of the soot surface growth process according to the HACA assumption are defined as follows:

$$C_i - H + H \rightleftharpoons C_i* + H_2 \tag{2.33.}$$

$$C_i* + H \rightarrow C_i - H \tag{2.34.}$$

$$C_i* + C_2H_2 \rightarrow C_{i+2} - H + H \tag{2.35.}$$

where C_i is the acetylene C_2H_2 species of the combustion process and C_i* is the acetylene radical. Assuming O_2 is responsible for soot oxidation, the governing reaction is defined as:

$$C_i* + O_2 \rightarrow products \tag{2.36.}$$

Thus, the surface growth rate of soot particles was formulated as:

$$R_g = kC_g\alpha\Psi_{C_s}Sn \tag{2.37.}$$

where the site rate coefficient is k, the growth species concentration is C_g, the empirical steric factor is α, the surface area of a spherical particle is S, and the number density of soot particle is n. The diameter d_p of the soot particle sphere was based on the density

and mass of soot. The number of surface radicals per unit surface area Ψ_{C_s} is defined as:

$$\Psi_{C_s} = \frac{k_{A1}[H]}{k_{-A1}[H_2] + k_{A2}[H] + k_{A3}[C_2H_2] + k_{A4}[O_2]} \times \Psi_{C_s-H} \tag{2.38.}$$

where Ψ_{C_s-H} is the number of $C_i - H$ sites per unit soot particle area. Other detailed soot models has been reviewed by Kennedy [29].

In general, the mass fraction of soot Y_s in laminar diffusion flame could be computed from the equation given as [29]:

$$\frac{\partial}{\partial x_i}(\rho u_i Y_s) = \frac{\partial}{\partial x_i}\left[\rho \mathcal{D} \frac{\partial Y_s}{\partial x_i}\right] + \frac{\partial}{\partial x_i}\left[0.54\eta \frac{1}{T}\frac{\partial T}{\partial x_i} Y_s\right] + \frac{d}{dt}(\rho_s f_v) \tag{2.39.}$$

where the soot density is ρ_s, the soot volume fraction is f_v, and thermophoretic diffusivity coefficient is η.

2.2. Magnetic Field Effect on Non-Premixed Flames

The presence of magnetic field in the vicinity of gaseous flames alters the flame characteristics due to the magnetic nature of the combustion gases which interacts with the magnetic field. The nature of the interaction depends also on the variation of the magnetic field being imposed on the gaseous flame [38–40].

Prior to 1847, little was known about the effect of magnetic fields on flames until the work of Padre Bancalari, who found that candle flames deflect in the presence of magnetic field aroused the interest of Zantedeschi and Faraday. In 1847, Zantedeschi and Faraday presented independent reactions to the work of Bancalari on flame behavior in the vicinity of magnetic fields. Faraday used an electromagnetic field generated by attaching a conical soft iron to the base of a horse-shoe that is wound with copper coils [38–40].

Faraday and Zantedeschi observed that a flame deflects in the opposite direction of the magnetic field when current was supplied to the wound copper coil and returned to it natural position when the current supply was disconnected. This effect was

pronounced in the presence of a strong magnetic fields [38, 39]. This flame behavior was initially attributed to the diamagnetic nature of gaseous species present in flames by researchers [39, 41]. Most gaseous species found in flames are repelled towards the decreasing magnetic field when placed in the vicinity of magnetic fields. However, oxidizing gaseous species like O_2 behave in an opposite manner towards the increasing magnetic field [39, 42, 43].

Contrary to the interpretation by Faraday [39] and Ueno et al. [44] that flame behavior in the presence of magnetic field is due to the diamagnetic nature of gaseous species, Wakayama posited that it was due to the paramagnetic nature of oxygen, while the diamagnetic nature of the fuel and the combustion products have less impact on the flame behavior [45].

More than one century after initial observations on the effect of magnetic fields on flames obtained by Faraday [39] and Zantedeschi [38], it was reported that magnetic fields also affect the luminescence of non-premixed flames [46]. As the magnetic field intensity imposed on the non-premixed flame increases, the luminescence of the flame increases [46].

In addition to the luminescence of non-premixed flames, the emission characteristics of certain excited ions in non-premixed flames are affected by the presence of magnetic fields. The emission characteristics of certain excited species containing oxygen such as HPO decreases in the presence of a magnetic field, but the emission characteristics of excited ions without oxygen such as CuH, CuCl, S_2, and Se_2 are negligibly affected by the presence of magnetic fields [47]. However, the effect of magnetic fields on the emission characteristics of excited ions depends on the direction of the magnetic field gradient [48]. When the non-premixed flame is located in an upward- decreasing magnetic field such as region B in Figure 2.1., the emission intensity of the excited ions increases. However, the emission intensity of the excited ions decreases in an upward-increasing magnetic field (Region C) [48]. In a uniform

magnetic field, the effect of magnetic field on non-premixed flames is insignificant (Region A) [49].

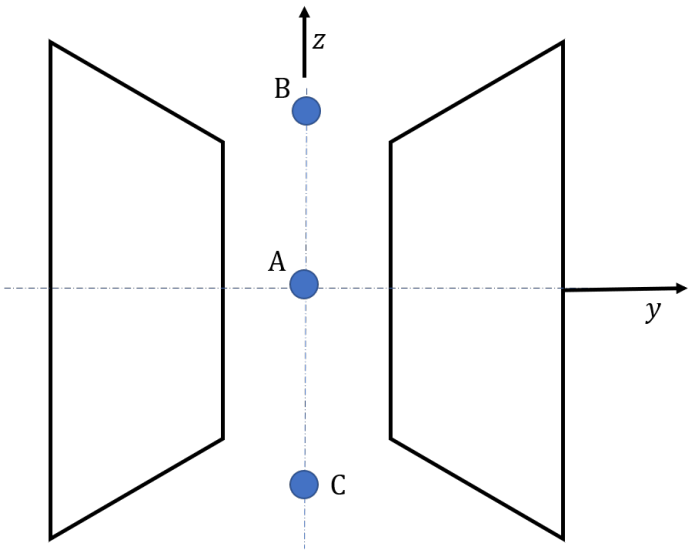

Figure 2.1. Magnetic field imposed on a non-premixed flame.

Magnetic fields imposed on the non-premixed flames affect the flame temperature. However, the effect on the flame temperature depends on the magnetic field gradient. In a uniform magnetic field with zero magnetic field gradient, the flame temperature is not affected [50]. In an upward-decreasing magnetic field, the flame temperature increases while the flame temperature decreases in an upward-increasing magnetic field [41, 45, 50].

Flame heights of non-premixed have been reported to be affected by the presence of magnetic fields [38, 51], but it depends on the direction of the magnetic field gradient that is imposed on the flame. The lift-off height of a non-premixed flame under a vertical magnetic field has been computed numerically [52].

Above a critical fuel flow rate, the base of a diffusion flame detaches from the burner tip and is suspended above the burner tip. This phenomenon is called lift-off. The condition at which lift-off or flame instability occurs is altered by exposing the flame to a non-uniform magnetic field [2]. Again, this effect depends on the direction of the

magnetic field gradient. There are insignificant effects when a uniform magnetic field is imposed on the non-premixed flame, but the lift-off height decreases when an upward-decreasing magnetic field is imposed [2, 53, 54].

In microgravity, diffusion flames are difficult to sustain due to lack of buoyancy-induced convection of combustion species. However, magnetic fields is used to support and sustain combustion of diffusion flames in microgravity [55, 56]. Numerical study on the effect of magnetic fields on microgravity combustion conducted on hydrogen – oxygen diffusion flames indicated that the combustion was supported in the presence of a magnetic field gradient. This was due to the induced magnetic body force acting on the paramagnetic species, and mainly attributed to O_2 [56].

Soot morphology and aggregates are affected by the presence of magnetic fields. The size of soot particles increase in the presence of the magnetic field as reported in [57]. However, this effect depends on the location of the measurement conducted [57].

Other than the experiments conducted on the effect of magnetic fields on non-premixed flames characteristics, numerical computation can predict the behavior of non-premixed flames in the presence of magnetic fields [52, 56, 58]. The effect of magnetic field on the stabilization of lifted flames has been simulated [58]. The lift-off height of a non-premixed flame under a vertical magnetic field has been computed numerically [52].

The effect of magnetic fields on pollutants generated from combustion processes are yet to be predicted numerically exhaustively based on our knowledge of available literature. In this regard, this research intends to bridge the knowledge of the effect of magnetic field on pollutants such as CO and soot by conducting a numerical modeling of the effect of magnetic field on non-premixed flames. To study the impact of magnetic fields on common pollutants emitted by non-premixed flames numerically, a numerical simulation of the underlying physics of a co-flowing non-premixed flame, soot formation model, and the magnetic field is conducted using commercial software.

Non-premixed flames have been modeled in numerous literature using either simple reaction mechanisms [59–61] or detailed reaction mechanisms [10, 62–64], while soot formation in non-premixed flames has been modeled in numerous literature using method of moments [65], or other semi-empirical methods [1, 66, 67]. In this research, the non-premixed flame is modeled using a detailed reaction mechanism and the soot formation is modeled with a mathematical model (Moss-Brooks).

Chapter 3.
Computational Models of Co-flowing Non-Premixed Flame, Magnetic Fields, and Soot Formation

This chapter describes the computational modeling of non-premixed flames, numerical modeling of soot generated by laminar non-premixed flames, and the numerical modeling of magnetic fields of a permanent magnet. The computational methods described are validated with experimental data available in literature.

In general, laminar co-flowing non-premixed flames are modeled numerically by solving the governing equations given in Equation 1.9. - Equation 1.13. using a numerical method - finite difference method, finite element method, finite volume method, or spectral method [68]. In this work, the finite volume method is used to model the laminar non-premixed flame whereas a finite element method is employed to compute the magnetic field.

3.1. Finite Volume Discretization: Integral Conservation Equation

In general, the conservation equation of a steady state flow problem is given as [69–71]

$$\nabla \cdot (\rho\phi\mathbf{v}) = \nabla \cdot \left(\Gamma_\phi \nabla\phi\right) + S_\phi \tag{3.1.}$$

where ρ is the fluid density, $\mathbf{v}$ is the fluid velocity vector, ϕ is the fluid transport scalar, Γ_ϕ is the diffusion coefficient of ϕ, and S_ϕ is the source of ϕ per unit volume. Let the approximate solution to ϕ be $\bar{\phi}$, then the residual $\mathcal{R}_{\bar{\phi}}$ of the conservation equation is given by

$$\mathcal{R}_{\bar{\phi}} = \nabla \cdot \left(\rho\bar{\phi}\mathbf{v}\right) - \nabla \cdot \left(\Gamma_{\bar{\phi}} \nabla\bar{\phi}\right) - S_{\bar{\phi}} \tag{3.2.}$$

Integrating and applying Gauss theorem to Equation 3.2. gives

$$\int_V \mathcal{R}_{\bar{\phi}} dV = \oint_{\partial V} \left(\rho\bar{\phi}\mathbf{v}\right) \cdot d\mathbf{A} - \oint_{\partial V} \left(\Gamma_{\bar{\phi}} \nabla\bar{\phi}\right) \cdot d\mathbf{A} - \int_V S_{\bar{\phi}} dV = \varepsilon_{\bar{\phi}} \tag{3.3.}$$

In order to compute Equation 3.3. numerically, the fluid domain is subdivided into

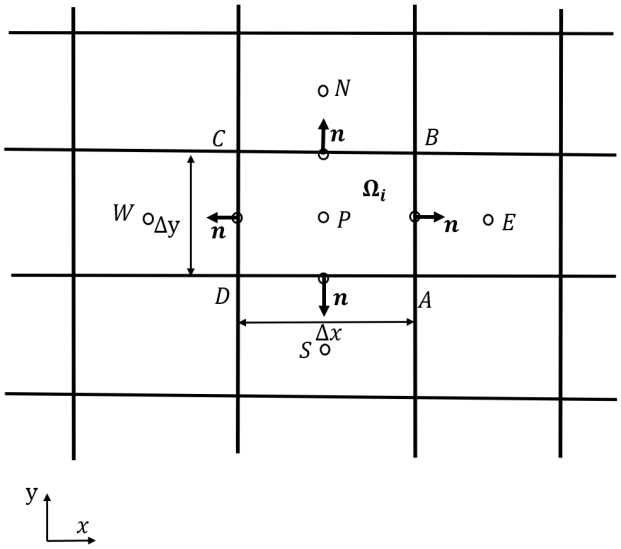

Figure 3.1. Discretization domain of a structured mesh with uniform grid size

smaller volumes called mesh or control volumes (CV) as shown in Figure 3.1.. Equation 3.3. in discrete form is applied to each control volume (see Figure 3.1.) of the computational domain results in

$$\sum_{f}^{\mathrm{N}_{faces}} \rho_f \mathbf{v}_f \bar{\phi}_f \cdot \mathbf{A}_f - \sum_{f}^{\mathrm{N}_{faces}} \Gamma_{\bar{\phi}} \nabla \bar{\phi}_f \cdot \mathbf{A}_f - \mathrm{S}_{\bar{\phi}} \mathrm{V} = \varepsilon_{\bar{\phi}} \tag{3.4.}$$

ρ_f is the fluid density, N_f is the number of faces enclosing the control volume, $\bar{\phi}_f$ is the value of $\bar{\phi}$ convected through the face f, $\mathbf{A}_f$ is the area vector of face f, $\nabla\bar{\phi}_f$ is the gradient of $\bar{\phi}$ at face f, and V is the volume of the control volume.

3.1.1. Discretization Scheme Methodology

To solve the governing equations using Finite Volume schemes, two approaches can be used to evaluate the flow variables within the discretized CVs. These are:

- Cell Centered Approach: In this approach, the unknown flow variables are defined at the center of the mesh cells. These values are interpolated to compute the values assigned at the grid points also known as node points.
- Cell Vertex Approach: This approach assigns the unknown variables to the vertices

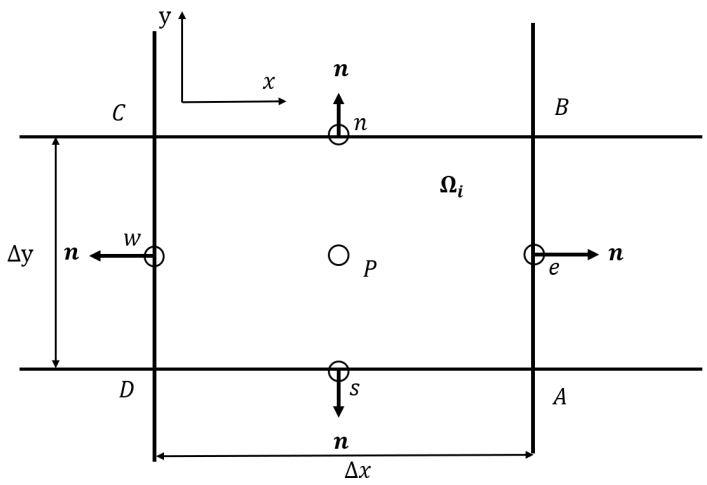

Figure 3.2. Control volume of the fluid domain.

(nodes) of the domain mesh. This values are used in the discretized equation.

The cell centered approach is considered in this work during the discretization of the governing equation.

3.1.2. Spatial Discretization of the Integral Equation

The finite volume equation given in (3.4.) is solved algebraically by approximating the fluid variable values on the cell faces of the control volumes as shown in Figure 3.2. as an interpolation from the cell-centered values using one of the following spatial discretization schemes - upwind differencing scheme, central differencing scheme, second order upwind differencing scheme, etc.

3.1.2.1. Upwind Interpolation Scheme

The approximate value of a fluid variable ϕ on the face e (ϕ_e) of the CV as shown in Figure 3.1. using the upwind scheme is equal to the value of the fluid variable in the neighboring cell [69]. However, the value of ϕ_e depend on the direction of the flow such that:

$$\phi_e = \begin{cases} \phi_{\mathrm{P}} & if \ (\mathbf{V}\cdot\mathbf{n}) > 0 \\ \phi_{\mathrm{E}} & if \ (\mathbf{V}\cdot\mathbf{n}) < 0 \end{cases} \tag{3.5.}$$

This discretization scheme is first order accurate.

3.1.2.2. Central Differencing Scheme

This scheme is also known as the linear interplolation scheme. It interpolates between two neighboring cells which share the face of interest to be computed. The face value ϕ_e is computed using

$$\phi_e = \psi\phi_P + (1-\psi)\phi_E \tag{3.6.}$$

where $\psi = \frac{|x_e - x_E|}{|x_P - x_E|}$. This scheme is second order accurate for a structured mesh but first order accurate for an unstructured mesh [69]. To compute the convection term for example using this scheme at the face e in Figure 3.1., the interpolation is given as:

$$(\nabla\phi \cdot \mathbf{n})_e = \left(\frac{\partial\phi}{\partial n}\right)_e \approx \frac{\phi_E - \phi_P}{x_E - x_P} \tag{3.7.}$$

3.1.2.3. Second Order Upwind Differencing Scheme

The scheme is an improvement to the upwind scheme discussed previously. It incorporates a gradient term into the upwind scheme so as to improve the accuracy of the scheme from 1st order to 2nd order. Similar to regular upwind scheme, this scheme depends on the flux direction. Thus, the fluid variables at the cell faces are computed using

$$\phi_e = \begin{cases} \phi_P + (\nabla\phi)_P \cdot \mathbf{r} & \text{if } (\mathbf{V}\cdot\mathbf{n}) > 0 \\ \phi_E + (\nabla\phi)_P \cdot \mathbf{r} & \text{if } (\mathbf{V}\cdot\mathbf{n}) < 0 \end{cases} \tag{3.8.}$$

$\mathbf{r}$ is the displacement vector from the upstream cell centroid to the face centroid.

3.2. Problem Formulation and Geometry

Although practical combustion modeling are the three-dimensional turbulent modeling with the recent advanced computational resource available, significant insight into such systems are obtained from modeling simplified domains in the laminar region of the flow. In this regard, an axisymmetric, laminar non-premixed

flame configuration is used to model the effect of the magnetic field of a pair of infinitely wide permanent magnets on the formation of soot and CO.

The axisymmetric laminar non-premixed flame configuration comprises a propane (C_3H_8) fuel flowing through an inner tube whose inner diameter is 6 mm with a wall thickness 1 mm. The oxidizer (Air) flows concentrically through a tube of diameter 52 mm surrounding the flowing fuel. A schematic of the configuration is shown in **??**.

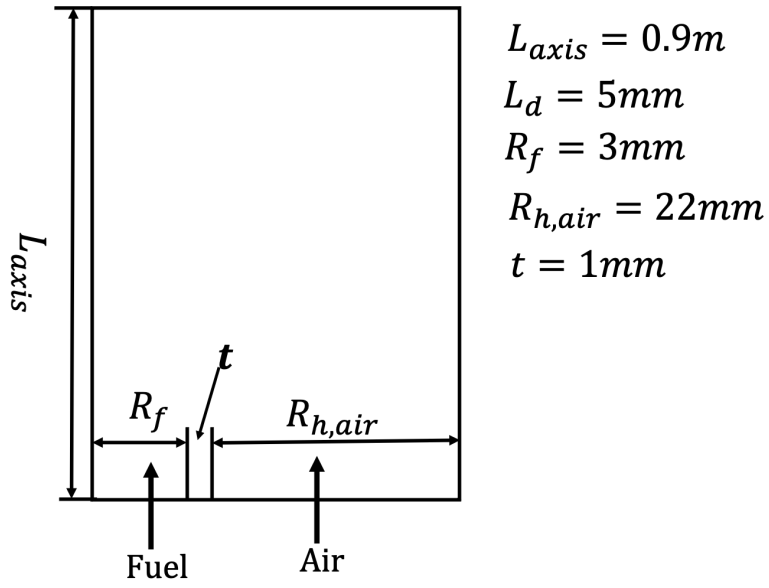

Figure 3.3. Non-premixed flame configuration

3.3. Mathematical Model

The reacting fluid flow is assumed to be axisymmetric due to the flame configuration, and the fluid flow is steady.

In this regard, the elliptic partial differential equations governing the physics of reacting flow - conservation of mass, momentum, energy, and species using the Cartesian tensor notations are defined respectively by [9]

$$\frac{\partial(\rho u_i)}{\partial x_i} = 0 \tag{3.9.}$$

$$\rho u_j \frac{\partial u_i}{\partial x_j} = -\frac{\partial p}{\partial x_i} + \frac{\partial \tau_{ij}}{\partial x_j} + \rho \sum_{k=1}^{N} (Y_k f_k)_i \tag{3.10.}$$

with $\tau_{ij} = -\frac{2}{3}\mu \frac{\partial u_k}{\partial x_k}\delta_{ij} + \mu\left(\frac{\partial u_i}{\partial x_j} + \frac{\partial u_j}{\partial x_i}\right)$

$$\frac{\partial(\rho u_i h^s)}{\partial x_i} - \frac{\partial}{\partial x_i}\left(\rho \sum_{k=1}^{N} h_k^s \mathcal{D}_{kN} \frac{\partial Y_k}{\partial x_i}\right) - \frac{\partial}{\partial x_i}\left(\lambda \frac{\partial T}{\partial x_i}\right) = u_i \frac{\partial p}{\partial x_i} - \sum_{k=1}^{N} h_k^0 \dot{\omega}_k \tag{3.11.}$$

$$\rho u_i \frac{\partial Y_k}{\partial x_i} - \mathcal{D}_{kN} \frac{\partial Y_k}{\partial x_i} = \dot{\omega}_k \qquad \text{for } k = 1, 2, 3, \ldots N \tag{3.12.}$$

The equation of state of the ideal gas is given in Equation 3.13..

$$p = \rho R_{mix} T = \rho \mathcal{R} T \sum_k \left(\frac{Y_k}{W_k}\right) \tag{3.13.}$$

where u_i is average velocity components of the fluid mixture in each direction $i - (r, \theta, z)$, τ_{ij} is the shear stress tensor, and p is the hydrostatic pressure of the combustion system. Y_k and f_k are the mass fraction and body force per unit mass of the species k in the mixture, respectively.

The presence of a magnetic field in the vicinity of the flame induces an additional body force $f_{mk,i}$ acting on species within the flame. Thus, the body force per unit mass f_k acting on the species of the flame is given by

$$(f_k)_i = g_i + f_{mk,i} \tag{3.14.}$$

To compute the characteristics of the flame numerically, the thermodynamic and transport properties are computed from thermodynamics and transport data using a polynomial fit. However, the chemical reaction of the combustion process is modeled with the finite rate reaction model.

3.3.1. Thermodynamics and Transport Properties Models

The thermodynamic and transport properties are computed assuming the fluid mixtures is comprised of ideal gases. The thermodynamic properties are computed using NASA polynomial fit coefficients [72].

3.3.1.1. Specific Molar Heat Capacity $C^0_{p,k}$ of Chemical Species k

The specific heat capacity $C^0_{p,k}$ of each of the gaseous species is computed using the polynomial fit coefficients as [5, 14, 73]

$$\frac{C^0_{p,k}}{\mathcal{R}} = \sum_{i=1}^{5} a_{i,k} T_k^{i-1} \tag{3.15.}$$

The molar specific heat of the mixture is evaluated using

$$\bar{C}_{p,mix} = \sum_{k=1}^{N} X_k C^0_{p,k}(T)$$

3.3.1.2. Specific Molar Enthalpy H^0_k of Chemical Species

Using the NASA polynomial fits, the specific molar enthalpy of the chemical species is computed using

$$\frac{H^0_k}{\mathcal{R}} = a_{6,k} + \sum_{i=1}^{5} \frac{a_{i,k}}{i} T_k^i \tag{3.16.}$$

and the mixture average specific molar enthalpy $\bar{H}$ is computed with

$$\bar{H} = \sum_{k=1}^{N} X_k H^0_k$$

3.3.1.3. Diffusivity of the Gaseous Species

The diffusivity D_{ij} of binary gases i and j is evaluated with [14, 73]

$$D_{ij} = \frac{3}{16} \frac{\sqrt{2\pi\kappa_B^3 \frac{T^3}{m_{ij}}}}{p\pi\sigma_{ij}^2 \Omega_{ij}^{(1,1)}} \tag{3.17.}$$

$m_{ij} = \frac{m_i m_j}{m_i + m_j}$ is the reduced mass, κ_B is Boltzmann constant, σ_{ij} is the reduced collision diameter, and $\Omega_{ij}^{(1,1)}$ is the collision integral.

The mixture diffusivity of species k is computed using

$$D_{km} = \frac{1 - Y_k}{\sum_{j \neq k}^{N} \frac{X_j}{D_{jk}}} \tag{3.18.}$$

3.3.1.4. Thermal Conductivity of the Mixture

The thermal conductivity of the fluid mixture is computed as [74]

$$\lambda = \frac{1}{2} \left[\sum_{k=1}^{N} X_k \lambda_k + \frac{1}{\sum_{k=1}^{N} \left(\frac{X_k}{\lambda_k} \right)} \right] \tag{3.19.}$$

3.3.2. Viscosity of the Mixture

The viscosity μ of the gaseous mixture used in modeling the non-premixed flame is evaluated using [74]

$$\mu = \sum_{k=1}^{N} \frac{X_k \mu_k}{\sum_{j=1}^{N} X_j \Phi_{kj}} \tag{3.20.}$$

$$\Phi_{kj} = \frac{1}{\sqrt{8}} \left(1 + \frac{W_k}{W_j} \right)^{-\frac{1}{2}} \left(1 + \left(\frac{\eta_k}{\eta_j} \right)^{\frac{1}{2}} \left(\frac{W_j}{W_k} \right)^{\frac{1}{4}} \right)^2$$

where W_k and W_j are the molecular weights of species k and j.

3.3.3. Chemical Kinetics

The effect of chemical kinetics on the reacting flow is modeled based on a reaction mechanism that defines the rate of formation and destruction of chemical species. The reaction mechanism can either be a skeletal or detailed. In this work, a detailed reaction mechanism with 58 species and 270 is used to model the kinetics of the reacting flow [75].

The chemical source term of Equation 1.12. is computed by solving the Ordinary Differential Equation (ODE) system governing the chemical kinetics. Due to the rapid transient nature of chemical kinetics, the system of ODE is stiff. The stiff ODE is linearized using the In-Situ Adaptive Tabulation (ISAT) approach, which accelerates the detailed chemistry computation [76].

3.3.4. Boundary Condition

The system of elliptic partial differential equations modeling the transport of reactive flow requires appropriate boundary conditions to fully define the phenomena. In this regard, along the axis of symmetry ($r = 0$), $u_r = \frac{\partial u_z}{\partial r} = \frac{\partial \mathrm{T}}{\partial x_i} = \frac{\partial \mathrm{Y}_k}{\partial x_i} = 0$ for $k = 1, 2, \ldots, \mathrm{N}$. The flow condition at the pressure outlet ($z = \mathrm{L} = 900\,\mathrm{mm}$) is such that $p_g = 0$. The combustion wall ($r = \mathrm{R_{air}}$) of the combustion domain has a no-slip condition $u_r = u_z = 0$ with the temperature gradient across the wall $\nabla \mathrm{T} = 0$ and there is no diffusive flux across the wall. The condition on the pipe wall $[(\mathrm{R}_f \leq r \leq \mathrm{R}_f + t_f)\&(z = 0)]$ is such that no energy is transferred across the pipe-wall, thus $\frac{\partial \mathrm{T}}{\partial r} = \frac{\partial \mathrm{T}}{\partial z} = \frac{\partial \mathrm{Y}_k}{\partial r} = \frac{\partial \mathrm{Y}_k}{\partial z} = u_r = u_z = 0$. The inlet flow is assumed to be fully developed before exit the tubes such that the fuel inlet velocity is $u_z = u_{\mathrm{fuel}}$, the fuel mass fraction is $\mathrm{Y}_{\mathrm{C_3H_8}} = 1$, and the fuel inlet temperature is $\mathrm{T} = 300\,\mathrm{K}$. However, the air inlet flow velocity is $u_z = u_{\mathrm{air}}$, air inlet mass fraction is $\mathrm{Y}_{\mathrm{O_2}} = 0.233, \mathrm{Y}_{\mathrm{N_2}} = 0.767$, and the inlet flow temperature is $\mathrm{T} = 300\,\mathrm{K}$. In these conditions, $u_{\mathrm{fuel}} = 2\bar{\mathrm{V}}_f[1 - (\frac{r}{\mathrm{R}_f})^2]$, $u_{\mathrm{air}} = \frac{2\bar{\mathrm{V}}_{\mathrm{air}}}{[1+\kappa^2+\frac{(1-\kappa^2)}{\log(\kappa)}]}[1 - (\frac{r}{\mathrm{R_{air}}})^2 - \frac{(1-\kappa^2)}{\log(\kappa)} log(\frac{r}{\mathrm{R_{air}}})]$, with $\kappa = \frac{(\mathrm{R}_f + t_f)}{\mathrm{R_{air}}}$.

The average inlet fuel velocity $\bar{\mathrm{V}}_f$ is $0.493\,\mathrm{m/s}$, and the average inlet air velocity $\bar{\mathrm{V}}_{\mathrm{air}}$

is 0.458 m/s. The radius of the fuel flow R_f is 3 mm, the wall thickness of the fuel flow t_f is 1 mm, and the radius of the air flow R_{air} is 26 mm.

3.3.5. Spatial Discretization of the Governing Equations

The effect of magnetic field gradients on the pollutants generated from propane-air non-premixed flames is studied numerically by discretizing the governing equations spatially using the Finite Volume Method. The finite volume discretization method is accomplished using Ansys-Fluent such that momentum, species, and energy equation were discretized with second order upwind method, while the continuity equation which solves for pressure was discretized using the second order central difference method [77].

3.4. Numerical Simulation of Non-Premixed Flames

This section describes the computation of a non-premixed flame based on the experimental configuration provided in [1] as shown in Figure 3.4.. A co-flowing mixture of ethylene (C_2H_4) and nitrogen (N_2) flows through a tube of diameter 4.0 mm with a thickness of 0.38 mm into a concentric tube of diameter 50 mm through which air flows. The fuel and oxidizer flow with an average velocity of 35 cm/s and the temperature of the flow are 300 K respectively.

3.4.1. Results of Numerical Simulations

Considering the configuration of [1], Figure 3.5. shows the computed flame characteristics of the diluted C_2H_4 - air non-premixed flames. The computed and measured temperature distribution of the flame are shown in Figure 3.5.. These computed flame characteristics are in agreement with the experimental data published in the literature.

Figure 3.5.a shows the temperature distribution of the flame. The maximum computed temperature is 2520 K while the maximum measured temperature is 2085 K. This discrepancy could be attributed to the fact that effect of radiation is not

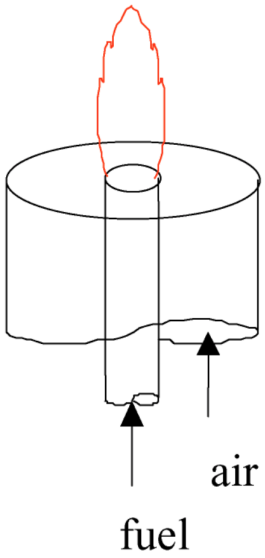

Figure 3.4. Schematic of the coflow non-premixed flame [1]

incorporated into the computation.

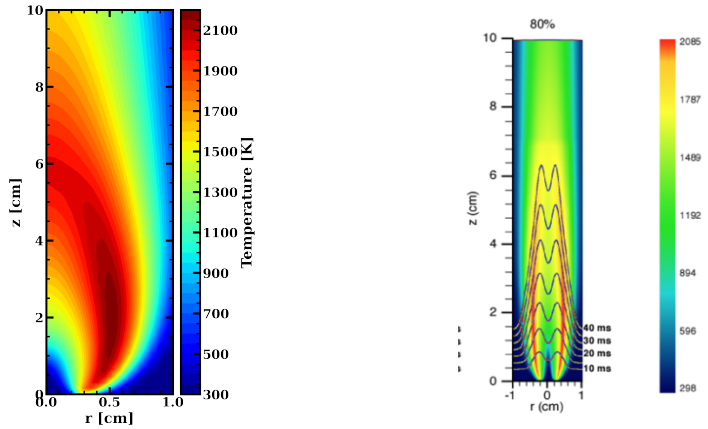

(a) Computed temperature [K] (b) Measured temperature [K] [1]

Figure 3.5. Computational validation of C_2H_4 - Air coflowing non-premixed with the experimental measurement provided by Smooke et al. [1] for 80% C_2H_4 and 20% N_2 by mass.

3.5. Soot Formation Model

In this work, the soot formation process is modeled using a semi-empirical (Moss-Brooks) model that was modeled for both laminar and turbulent co-flowing non-premixed flame. However, the computation of the soot particles generated by the non-premixed flames was conducted using a modified version of Moss-Brooks soot

model to model the soot nucleation and transport process.

Although other models described in section 2.1. could be formulated to model soot formation, the Moss-Brooks model was considered due to the simplicity and relative generality of the models.

The model solves the transport equation for the soot mass concentration (M) and soot number density (N). The soot model incorporates terms that describes the soot processes such as soot particle nucleation, coagulation, surface growth, and oxidation [78]. The rate of production of soot particles due to nucleation from the gaseous phase and coagulation in the free molecular regime is given by [77]

$$\partial_t(\rho \mathrm{Y}_s) + \frac{\partial}{\partial x_i}(\rho u_i \mathrm{Y}_s) = \frac{\partial}{\partial x_i}\left(\frac{\mu_{mix}}{\sigma_s}\frac{\partial \mathrm{Y}_s}{\partial x_i}\right) + \frac{d\mathrm{M}}{dt} \tag{3.21.}$$

$$\partial_t(\rho b_n^*) + \frac{\partial}{\partial x_i}(\rho u_i b_n^*) = \frac{\partial}{\partial x_i}\left(\frac{\mu_{mix}}{\sigma_n}\frac{\partial b_n^*}{\partial x_i}\right) + \frac{1}{\mathrm{N}_{norm}}\frac{d\mathrm{N}}{dt} \tag{3.22.}$$

The rate of soot nucleation $\frac{d\mathrm{N}}{dt}$ and rate of production of the mass concentration $\frac{d\mathrm{M}}{dt}$ are modeled respectively as:

$$\frac{d\mathrm{N}}{dt} = \mathrm{C}_\alpha \mathrm{N}_\mathrm{A}\left(\frac{\chi_{\mathrm{C_2H_2}}\mathrm{P}}{\mathcal{R}\mathrm{T}}\right)^l \exp\left(-\frac{\mathrm{T}_\alpha}{\mathrm{T}}\right) - \mathrm{C}_\beta\left(\frac{24\mathcal{R}\mathrm{T}}{\rho_s \mathrm{N}_\mathrm{A}}\right)^{\frac{1}{2}} d_p^{\frac{1}{2}}\mathrm{N}^2 \tag{3.23.}$$

$$\frac{d\mathrm{M}}{dt} = \mathrm{R}_n + \mathrm{R}_s + \mathrm{R}_o \tag{3.24.}$$

$$\mathrm{R}_n = \mathrm{M}_p \mathrm{C}_\alpha \left(\frac{\chi_{\mathrm{C_2H_2}} \mathrm{P}}{\mathcal{R}\mathrm{T}}\right)^l \exp\left(-\frac{\mathrm{T}_\alpha}{\mathrm{T}}\right) \tag{3.25.}$$

$$\mathrm{R}_s = \mathrm{C}_\gamma \left(\frac{\chi_{\mathrm{C_2H_2}} \mathrm{P}}{\mathcal{R}\mathrm{T}}\right)^m \exp\left(-\frac{\mathrm{T}_\gamma}{\mathrm{T}}\right) \left[(\pi \mathrm{N})^{\frac{1}{3}} \left(\frac{6\mathrm{M}}{\rho_s}\right)^{\frac{2}{3}}\right]^n \tag{3.26.}$$

$$\mathrm{R}_o = -\mathrm{A}_{ox} \left[\mathrm{C}_{\omega_1} \chi_{\mathrm{OH}} + \mathrm{C}_{\omega_2} \chi_{\mathrm{O}} \exp\left(-\frac{\mathrm{T}_{\omega_2}}{\mathrm{T}}\right)\right] \tag{3.27.}$$

$$\mathrm{A}_{ox} = \mathrm{C}_{ox} \eta_{col} \frac{\mathrm{P}}{\mathcal{R}\mathrm{T}} \sqrt{\mathrm{T}} (\pi \mathrm{N})^{\frac{1}{3}} \left(\frac{6\mathrm{M}}{\rho_s}\right)^{\frac{2}{3}} \tag{3.28.}$$

where Y_s is the soot mass fraction, N is the soot particle number density, $b_n^* = \frac{\mathrm{N}}{\rho \mathrm{N}_{norm}}$ is the normalized soot nuclei concentration, and $d_p = \left(\frac{6\mathrm{M}}{\pi \rho_s \mathrm{N}}\right)^{\frac{1}{3}}$ is the average diameter of a soot particle. Values of soot model parameters are given in Table 3.1..

Table 3.1. Soot model parameters.

Parameter	**Value**
C_α	54 [1/s]
C_β	0.5
C_γ	11 700 [kgm/kmols]
C_{ω_1}	105.8125 $[\mathrm{kg-m/(kmolK^{\frac{1}{2}}s)}]$
C_{ω_2}	8903.51 $[\mathrm{kg-m/(kmolK^{\frac{1}{2}}s)}]$
l, m, n	1
M_p	144 [kg/kmol]
N_{norm}	1×10^{15} $[particles]$
$\mathrm{N_A}$	6.022×10^{26} [1/kmol]
T_α	21 100 [K]
T_γ	12 100 [K]
η_{col}	1.3×10^{-1}
C_{ox}	1×10^{-1}
ρ_s	2000 $[\mathrm{kg/m^3}]$

3.5.1. Numerical simulation of soot formation in non-premixed flames

Considering soot generated by the co-flowing non-premixed flame of diluted ethylene as described in [1], the modified Moss-Brooks model is used to model the soot

formation process in this configuration.

In this regard, additional elliptical partial differential equations that models the nucleation and transport of the soot particles formed by the non-premixed flames are incorporated to the governing equations.

The transport equation of soot mass fraction Y_s and the normalized soot nuclei concentration $b_n^* = \frac{N}{\rho N_{norm}}$ are [77–79]

$$\frac{\partial}{\partial x_i}(\rho u_i Y_s) = \frac{\partial}{\partial x_i}\left(\frac{\mu}{\sigma_s}\frac{\partial Y_s}{\partial x_i}\right) + S_m \tag{3.29.}$$

$$\frac{\partial}{\partial x_i}(\rho u_i b_n^*) = \frac{\partial}{\partial x_i}\left(\frac{\mu}{\sigma_n}\frac{\partial b_n^*}{\partial x_i}\right) + \frac{1}{N_{norm}} S_N \tag{3.30.}$$

The rate of production and destruction of soot mass concentration $S_m = \frac{dM}{dt}$ and the rate of production and destruction of soot number density $S_N = \frac{dN}{dt}$ are given in Equation 3.24. and Equation 3.23. respectively. The soot particle Schmidt number σ_s and nuclei Schmidt number σ_n are assumed to be unity respectively.

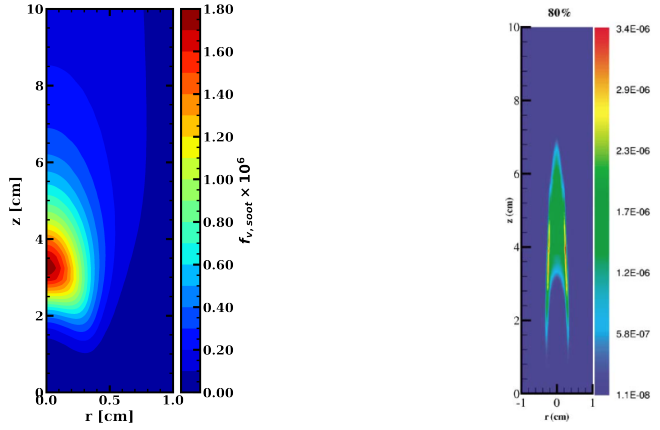

(a) Computed soot volume fraction

(b) Experimental soot volume fraction [1]

Figure 3.6. Computed characteristics of the diluted ethylene co-flowing non-premixed flame

Figure 3.6.a shows results for soot volume fraction obtained from the modified Moss-Brooks model. The results agree with published experimental data. The peak measured soot volume fraction is 3.4×10^{-6} for 80% by mass of ethylene mixture

burning in air while the computed peak soot volume fraction with our model is 3.75×10^{-6}.

3.6. Numerical Computation of the Magnetic Field a Permanent Magnet

This section computes the magnetic field of a finite width and inifinite width permanent magnets numerically. The computed magnetic field are validated with the analytical results. Consider a NdFe35 rectangular permanent magnetic block with dimensions $A \times B \times L$ such that the magnetization vector ($\mathbf{M} = M\hat{k}$) acts in the z direction as shown in Figure 3.7.a. The analytical expression of the magnetic field **B** along z is defined as [80, 81]:

$$B(z) = \frac{\mu_{m,0}\mu_{m,r}M}{\pi}\left[\arctan\left[\frac{AB}{2z\sqrt{4z^2+A^2+B^2}}\right] - \arctan\left[\frac{AB}{2(L+z)\sqrt{4(L+z)^2+A^2+B^2}}\right]\right] \tag{3.31.}$$

Here, z is the distance measured from the top surface of the magnet in the direction of the North pole.

A numerical computation of the magnetic field in the domain around the magnet was conducted using a finite element package - Ansys-Maxwell [82] such that M = 890 000 A/m, $\mu_{m,r} = 1.1$, $\mu_{m,0} = 4\pi \times 10^{-7}$ H/m, A = 20 mm, B = 20 mm, and L = 40 mm.

The computational and analytical variation of the magnetic field along the z-axis of the magnet is shown in Figure 3.7.b, which depicts that the computed magnetic field agrees with the theoretical magnetic field.

For an infinitely wide permanent magnet, such that as $B \to \infty$ the magnetic field along the z-axis varies asymptotically as:

$$B(z) = \frac{\mu_{m,0}\mu_{m,r}M}{\pi}\left[\arctan\left(\frac{A}{2z}\right) - \arctan\left(\frac{A}{2(L+z)}\right)\right] \tag{3.32.}$$

When an infinitely wide permanent magnet as shown in Figure 3.8.a is considered, the magnetic field variation of the infinitely wide permanent magnet was computed

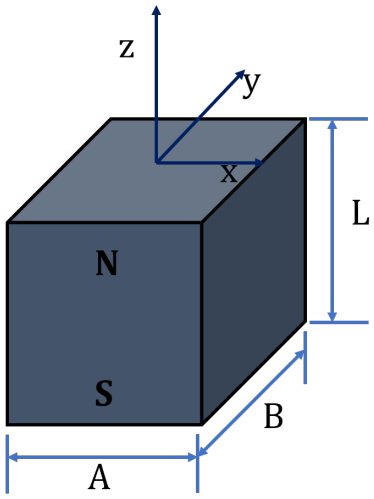

(a) Rectangular Permanent Magnet

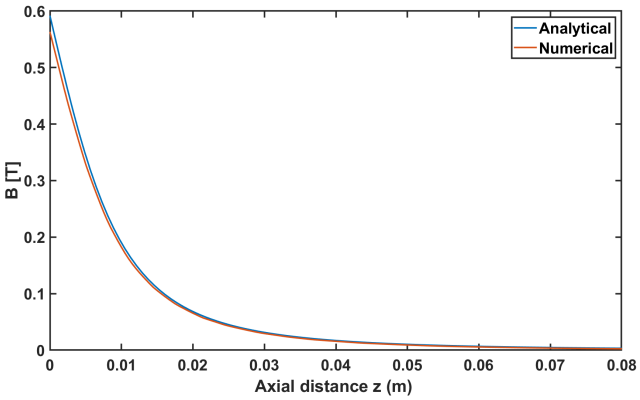

(b) Magnetic field of a finite width permanent magnet

Figure 3.7. Computation of the magnetic field of a finite width permanent magnet

is as shown in Figure 3.8.b. The computed field was compared to the analytical result obtained using Equation 3.32..

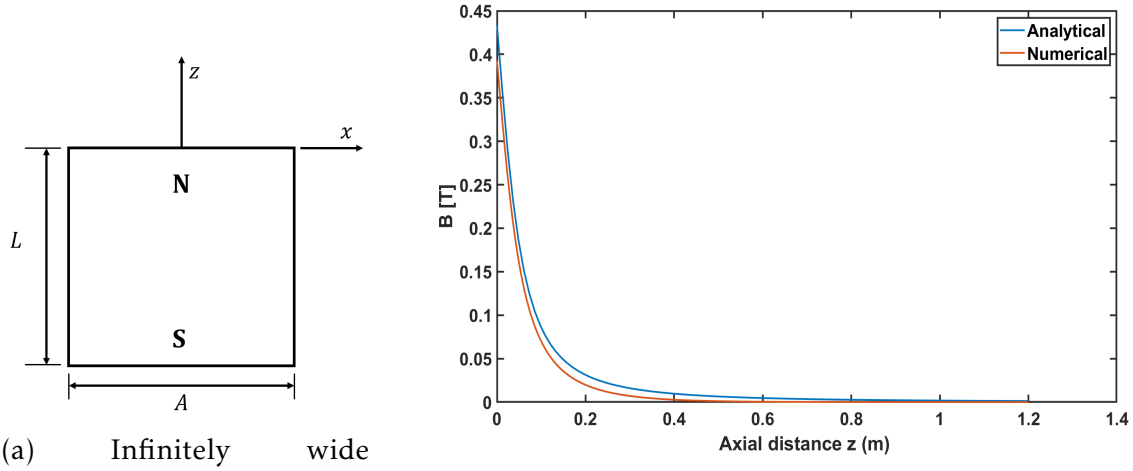

(a) Infinitely wide permanent magnet

(b) Magnetic field of an infinitely wide permanent magnet

Figure 3.8. Computation of the magnetic field of an infinitely wide permanent magnet

From Figure 3.7.b and Figure 3.8.b, the computed magnetic field agrees with the analytical magnetic field of the configuration. This indicates the accuracy of the computation of the magnetic field.

3.7. Numerical Computation of the Effect of Permanent Magnetic Field on Flame Lift-off Height

Experimental research on the effect of permanent magnetic field on the lift-off height of methane (CH_4) was conducted by Gillon et al. [2] for varying velocity of CH_4 and air. The experimental setup consists of a burner and two permanent magnets as shown in Figure 3.9.a. The burner is made up of two concentric tubes which carries methane through the inner tube of diameter 4 mm and a coflowing air through the outer concentric tube with diameter 10 mm. The tubes are 1 mm thick and the experiments were performed at atmospheric pressures and temperature of 293 K. The two permanent magnets generated a peak magnetic field of about 0.35 T at the center.

To validate assumptions and approach of this study, the imposed magnetic field was computed using Ansys-Maxwell [82] such that the magnetic field along the centerline of the flow has a peak magnitude of 0.35 T at the center. The magnets used in the computation was NdFeB35. The computed axial magnetic field shown in

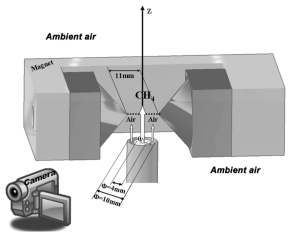

(a) Experimental Setup

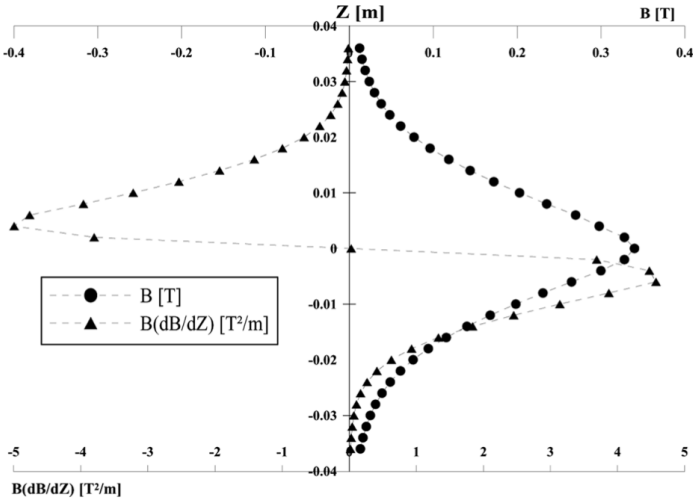

(b) Imposed magnetic field [T]

Figure 3.9. Experimental setup of the effect of magnetic field on the lift-off height of CH_4 - air non-premixed flame [2].

Figure 3.10. agrees quantitatively with the measured magnetic field during the experiments as shown in Figure 3.9.b.

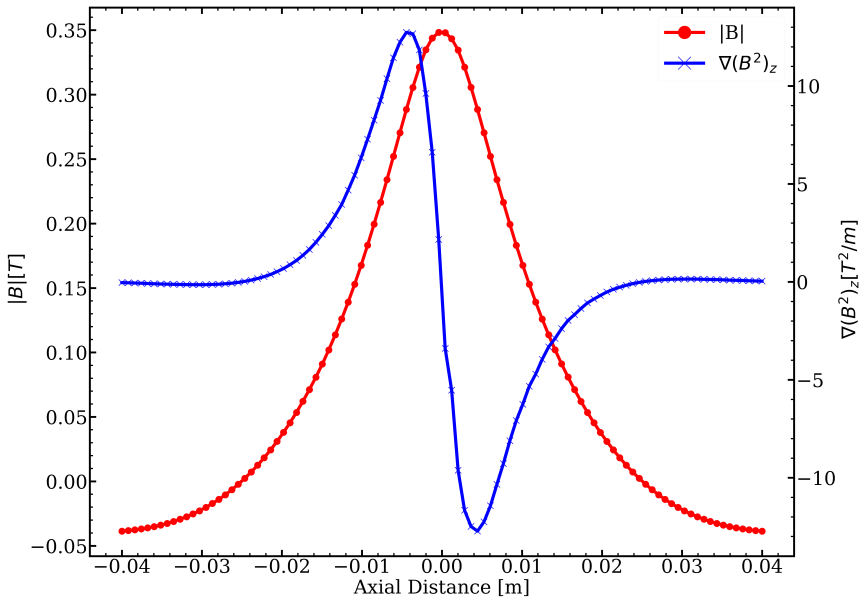

Figure 3.10. Computed magnetic field imposed on the non-premixed flame

3.7.1. Magnetic Body Force

Considering the source of the effect of magnetic fields on non-premixed flames, some researchers attributed it to the magnetic force $\mathbf{F}_L$ acting on charged combustion

species. The magnetic force acting on the charged combustion species based on the Lorentz force $\mathbf{F}_{\mathrm{L}}$ is however insignificant due to the small amount of these radicals in the combustion process [48].

The magnetic force $\mathbf{F}_m$ acting on the combustion species due to intrinsic magnetic properties of the species interacting with the magnetic field gradient is given as [48]

$$\mathbf{F}_{m,i} = \frac{1}{2}\rho(\chi_{m,i} - \chi_{m,0})\nabla\left(\mathbf{H}^2\right) \tag{3.33.}$$

where $\mathbf{H}$ the magnetic field, and $\chi_{m,i}$ the volumetric susceptibility of the species.

Equation 3.33. can be simplified further using the constitutive relations between $\mathbf{B}$ and $\mathbf{H}$ as [83]

$$\mathbf{F}_{m,i} = \frac{1}{2\mu_{m,0}}\rho \mathrm{Y}_i \chi_{m,i}\nabla\left(\mathbf{B}^2\right) \tag{3.34.}$$

The mass density of the combustion species i is $\rho \mathrm{Y}_i$, and $\nabla(\mathbf{B}^2)$ the gradient of the magnetic field.

This magnetic force F_m induced an additional body force - buoyant force acting on the fluid flow. The induced effect of the magnetic field depends on the location of the burner tips within the magnetic field. The buoyant force acting on the flow increases in the region where the magnetic field gradient is negative, but decreases in the region of positive magnetic field gradient.

Diamagnetic species (with no unpaired e^-) possess negative $\chi_{m,i}$, while the paramagnetic species (with unpaired e^-) possess a positive $\chi_{m,i}$. The magnetic susceptibility $\chi_{m,i}$ of the paramagnetic combustion species, which depends on the electron spin momentum S_i and the electron orbital momentum of the species is computed using Curie's law. According to Curie's law, the magnetic susceptibility $\chi_{m,i}$ of paramagnetic species is defined as [84]

$$\chi_{m,i} = \frac{\mathrm{N_A} g_{\mathrm{L}}^2 \mu_{\mathrm{B}}^2 \mathrm{S}_i\left(\mathrm{S}_i + 1\right)\mu_{m,0}}{3\kappa \mathrm{T M}_i} \tag{3.35.}$$

where the electron orbital momentum of the chemical species is neglected.

The total electron spin momentum S_i of the paramagnetic combustion species considered in this work are given in Table 3.2..

Table 3.2. Total Electron Spin S_i of major paramagnetic chemical Species i

i	O_2	O	OH	H	HO_2	CH_3	HCO	CH_2	CH	HC_2O
S_i	1	1	$\frac{1}{2}$	$\frac{1}{2}$	$\frac{1}{2}$	$\frac{1}{2}$	$\frac{1}{2}$	1	$\frac{1}{2}$	$\frac{1}{2}$

In this regard, the body force induced by the permanent magnet on the paramagnetic species is computed as

$$f_{mk,i} = \frac{1}{2\mu_{m,0}} Y_k \chi_{m,k} \frac{\partial\left(\mathbf{B}^2\right)}{\partial z} \quad \text{for } k = 1, 2, 3, \ldots, N \tag{3.36.}$$

Based on this experimental configuration, the numerical approach described is applied to compute the effect of magnetic field found experimentally. The magnetic field computed based on this setup was imposed on the non-premixed flame. The computed lift-off height and the flow conditions considered are given in Table 3.3..

Table 3.3. Lift-off height of methane-air non-premixed flame in the presence of magnetic field.

$V_{CH_4}[m/s]$	$V_{Air}[m/s]$	$H_{\text{lift-off}}[mm]$ - Measured	$H_{\text{lift-off}}[mm]$ - Computed
3.17	0.70	16	8
3.17	1.05	27	16
3.17	1.24	32	20

The lift-off height of the non-premixed flame increases with increase in air flow velocity for a given a fuel flow velocity. In the presence of a magnetic field, the flame lift-off height decreases as shown in Figure 3.11. . Although the computed lift-off height did not agree quantitatively, the relative effect of increasing the inlet velocity of air correlates with the effects observed experimentally with and without the presence of magnetic field as shown in Figure 3.11.. However, the effect of the magnetic field imposed on the flames agrees quantitatively with the measured data published.

The computed flame temperature is shown in Figure 3.12. for the flow conditions

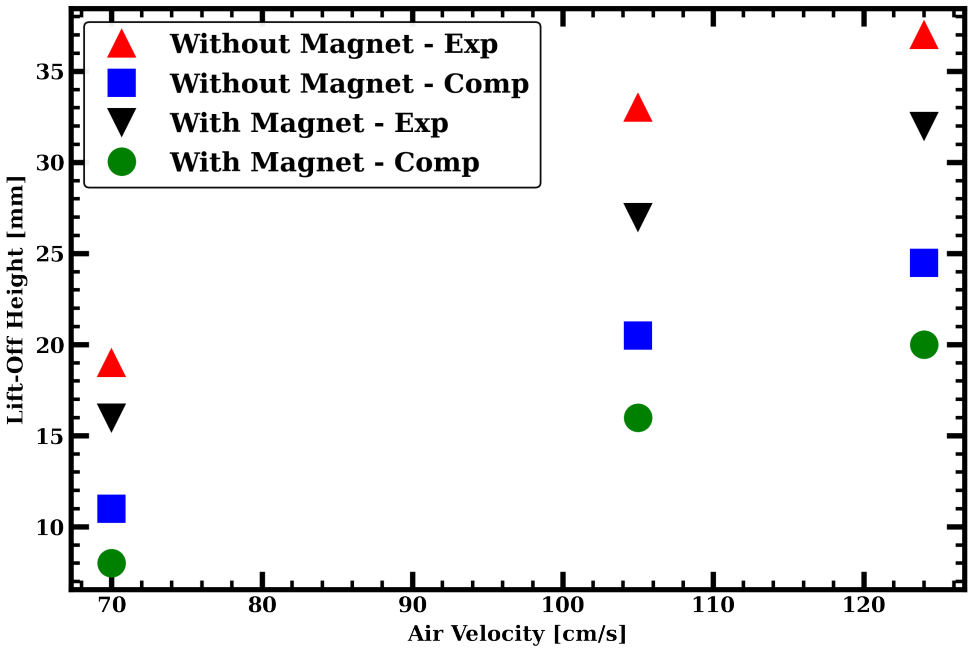

Figure 3.11. Magnetic field effect on flame lift-off height.

given in Table 3.3.. The quantitative agreement of the effect of magnetic field on the lift-off height of the non-premixed flame validates the computation of the effect of the magnetic field.

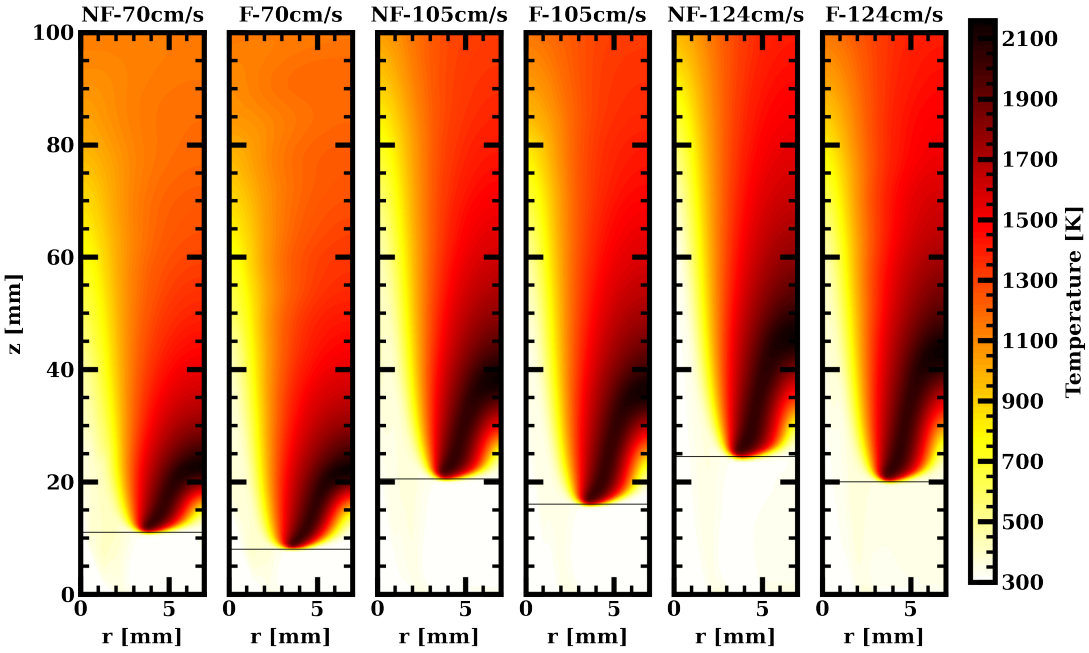

Figure 3.12. Effect of magnetic field on the temperature field.

Chapter 4.
Effect of Infinitely Wide Permanent Magnets on Soot and CO Formation in Laminar Non-Premixed Flames

The effects of magnetic fields on flame lift-off heights was presented in section 3.7.. In this chapter, the effect of a pair of infinitely wide permanent magnets in the vicinity of a co-flowing non-premixed flame on the formation of soot and CO is studied numerically such that the fuel (C_3H_8) flows with an average velocity of 0.439 m/s and the average inlet velocity of air is 0.458 m/s. The effect of the magnetic field on the non-premixed flame is studied when the axis of the permanent magnets is located at the flame tip.

Furthermore, the study considers the effect of the flame burner exit location in the magnetic field on the formation of the pollutants. Moreover, the effect of the flame size within the magnetic field is studied by reducing the fuel inlet velocity to 0.20 m/s, which reduces the flame size.

The chemical kinetics of the reaction is modeled using the laminar finite rate model with a detailed kinetic mechanism [75]. The detailed kinetic mechanism comprises 58 species and 270 elementary reactions that was imported into Ansys-Fluent. The thermodynamic and transport properties of the fluid mixture was computed using Ansys-Chemkin-Pro libraries [73].

Due to the imposed magnetic field on the non-premixed flames, an additional source term is appended to Ansys-Fluent as a user defined function (UDF). In this regard, the UDF is implemented to compute the magnetic force term acting on the fluid flow as an addon source code implemented by Ansys-Fluent. The magnetic force imposed on the fluid flow is assumed to act on the paramagnetic species given in Table 3.2. using the equation described in subsection 3.7.1.. The magnetic body force is computed using Equation 3.36..

To ensure a stabilized converged solution, GMRES stabilization method was used

during the computation process. The soot mass fraction was computed using the Modified Moss-Brookes model [78] described in section 3.5.. In this model, the incipient soot particle is assumed to be acetylene C_2H_2, the Schmidt number of the soot particles and soot nuclei are unity, and that the mass density of soot particle is 2000 kg/m^3. The oxidizing species of the soot formation process in this computation are OH and O which are assumed to be in partial equilibrium with the soot particles.

4.1. Problem Formulation

The flow configuration when placed in the vicinity of a pair of infinitely wide permanent magnets is shown in Figure 4.1.. The magnet is made of NdFe35 with a magnetic coercivity $\mathbf{H}_c$ = 890 kA/m and relative magnetic permeability μ_r = 1.1. In this configuration, the burner exit plane is located at the centerline of the permanent magnets.

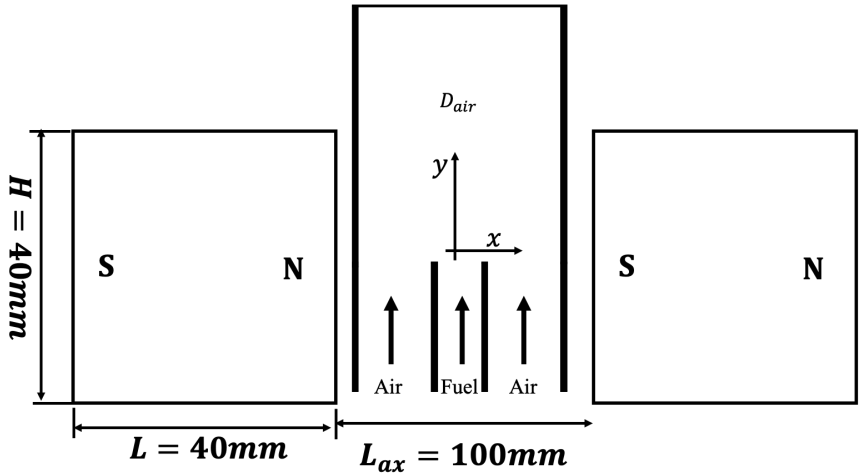

Figure 4.1. Magnetic field of a pair of infinitely wide permanent magnet imposed on non-premixed flame configuration

Although the magnetic field imposed is not axisymmetric due to the geometry of the magnet, the axisymmetric assumption is satisfactory because the magnetic force varies significantly only in the axial direction. Thus, the radial components are neglected in the computation.

4.2. Computation of the Magnetic Field of the Permanent Magnet

The magnetic field imposed on the non-premixed flame configuration shown in Figure 4.1. is computed using Ansys-Maxwell [82]. The pair of infinitely wide permanent magnets placed in the vicinity of the non-premixed flame are made up of NdFe35 such that the magnetic coercivity of the magnets $\mathbf{H}_c$ is 8.9×10^5 A/m in the horizontal direction and the relative permeability $\mu_r = 1.1$. Dimensions of the magnets are given in Figure 4.1.. In this study, the axis of the magnets is located at flame tip and at the flame burner exit. The flame tip is found around 180 mm downstream from the flame burner exit. The computed magnetic field and magnetic field gradient are shown in Figure 4.2..

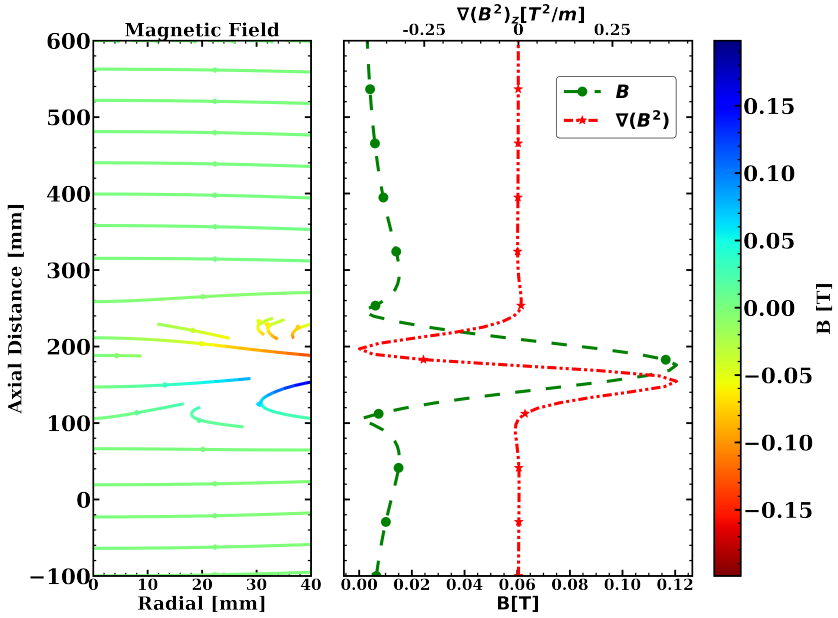

Figure 4.2. The magnetic field imposed on the non-premixed flame by the permanent magnets and the centerline variation of the magnetic field and the magnetic field gradient along the axial direction with the magnet's axis located at the flame tip.

Considering the burner exit plane as the origin plane, the computed vector plot and the centerline variation of the magnetic field **B** of the permanent magnets imposed on the flame is shown in Figure 4.3.. The computed peak magnetic field is 0.125 T and the

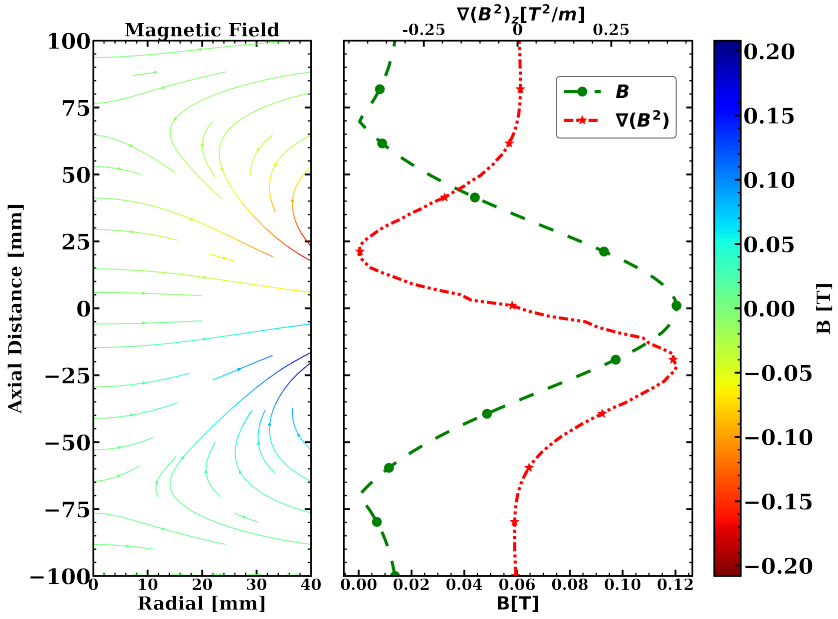

Figure 4.3. The magnetic field imposed on the non-premixed flame by the permanent magnets and the centerline variation of the magnetic field and the magnetic field gradient along the axial direction with the magnet's axis located at the flame burner exit.

computed peak magnetic field gradient is $0.38\,T^2/m$.

As shown in Figure 4.3., the peak magnetic field occurs at the central axis of the magnets which corresponds to the origin plane in this configuration. However, the peak magnetic field gradients imposed on the non-premixed flame offsets about $\approx 25\,mm$ from the central axis. The distance between the peak magnetic field gradients is approximately the height of the permanent magnets.

4.3. Results and Discussion

The magnetic field effects on CO and soot generated from a propane-air non-premixed flame is computed in the computational domain discretized with a non-uniform mesh size with an excerpt shown in Figure 4.4.. The non-uniform mesh sizes are chosen such that the axial direction of the computational domain has a minimum mesh size of $0.15\,mm$, while the radial direction has a non-uniform

minimum mesh sizes of 0.05 mm, 0.1 mm, and 0.22 mm at the fuel inlet, pipe thickness and air inlet respectively.

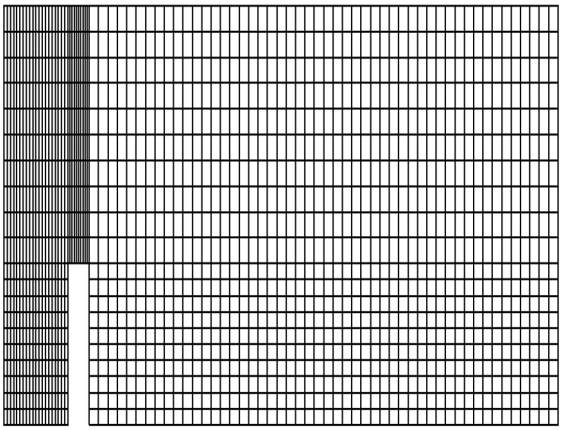

Figure 4.4. Excerpt of the discretized computational domain - Mesh

4.3.1. Grid Convergence Study

A grid convergence study is conducted for different mesh sizes in order to confirm an appropriate mesh distribution for the computational combustion analysis. In this study, flame characteristics in the absence of magnetic field are used to characterize convergence criteria of the grid study.

The computational approach described in chapter 3. is used to compute the non-premixed flame characteristics. The computed results shown in Figure 4.5. is the axial variation of the flame temperature for different mesh sizes. In this figure, the temperature variation obtained from the computation as the mesh size decreases trend the same profiles. The figure indicates that for mesh below 0.2 mm, the temperature profile are approximately the same. Figure 4.6. is the plot of infinity norm of the relative error of temperature against the minimum mesh size h_{min} used in the computation. As the mesh size decreases, the computational error norm given in Equation 4.1. decreases until the computational error stops changing significantly, which indicates that a relative accurate result would be obtained for mesh sizes $h_{min} < 0.2$.

$$\epsilon_r = \left\| \frac{\mathrm{T} - \mathrm{T}_{fine}}{\mathrm{T}_{fine}} \right\|_{\infty} \tag{4.1.}$$

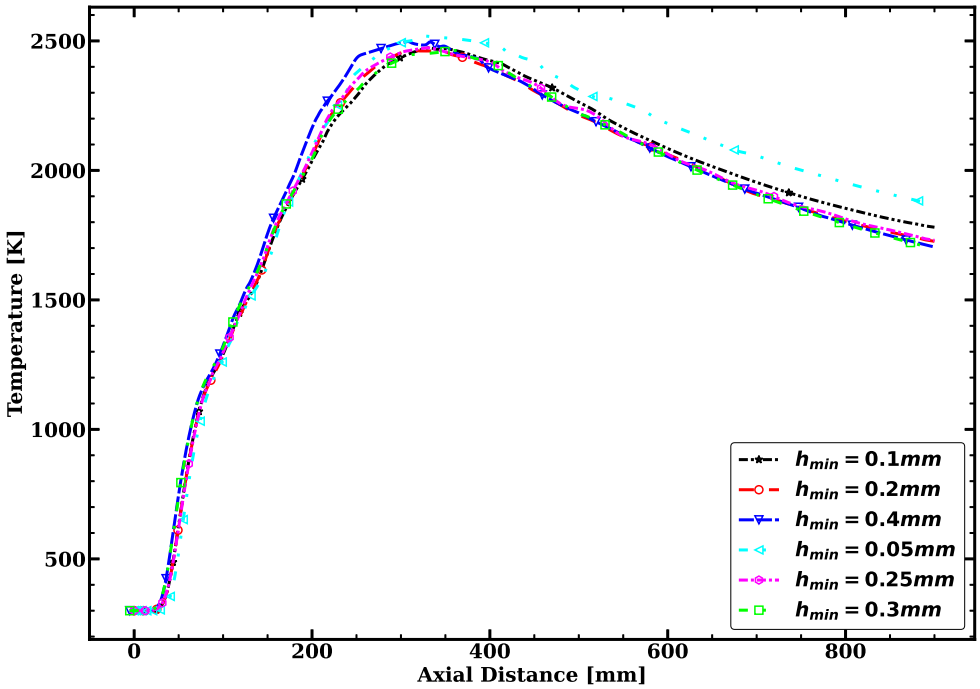

Figure 4.5. Comparison of computed results for different mesh sizes

4.3.2. Computation of the Flame Characteristics

The non-premixed flame characteristics of a propane gas flowing through a pipe of diameter 6 mm and thickness 1 mm with an average inlet velocity of 0.439 m/s while air is flowing through the concentric tube of diameter 52 mm with an average inlet velocity of 0.458 m/s is computed using the numerical approach described in chapter 3..

Figure 4.7. shows the computed radial variation of the flame characteristics - temperature, CO, soot mass fraction and soot volume fraction obtained from the non-premixed flame in the absence of a magnetic field at four different height from the flame exit 100 mm, 150 mm, 200 mm, and 300 mm downstream the flame burner exit plane. Downstream of the flow, the average flame temperature increases then decreases. In addition, the average value of the mass fraction of CO, mass fraction of soot, and volume fraction of soot increases downstream of the flame but decreases after

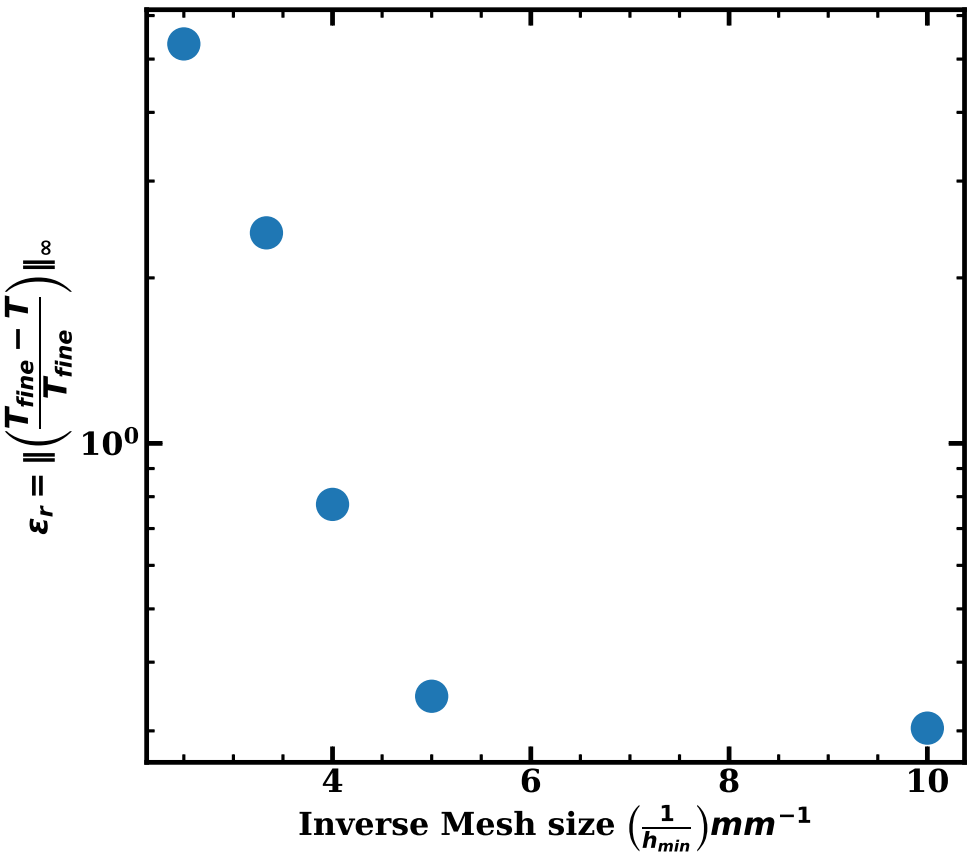

Figure 4.6. Grid Convergence Study

200 mm.

As shown in Figure 4.7., the region between [100 mm – 300 mm] downstream from the burner exit plane depicts the finite region where most of the combustion reaction is taking place, thus the formation of CO and soot. This implies that the flame height falls within this region. With respect to the variation of CO and soot, the flame tip is located at approximately close to 200 mm since the peak mass fraction of CO [Y_{CO}] decreases downstream at this height. Also at this height, the peak temperature indicates the location where the fuel-air mixture are close to the stoichiometric proportion while the region to the left of this peak indicate the fuel rich zone of the flame and the region to the right represent the region of fuel lean zone. The soot formation process started at around 100 mm as shown in Figure 4.7.. This formation process occurs over a vertical distance of approximately 200 mm.

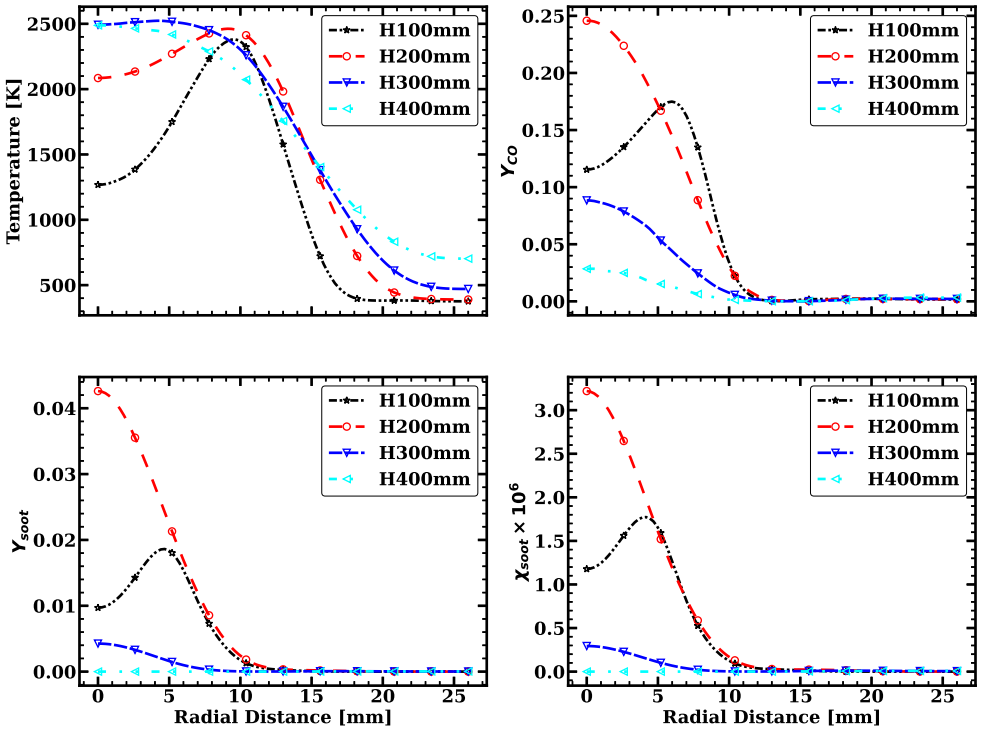

Figure 4.7. Radial variation of flame characteristics at different height from the flame exit without magnetic fields.

4.3.3. Effect of Magnetic Field on CO and Soot Formation

In this section, the effect of magnetic field on the formation of CO and soot when the axis of the permanent magnets are located around the flame burner exit and around the flame tip respectively.

4.3.3.1. Magnetic Field Imposed at the Flame Burner Exit

The computed variation of the temperature, mass fraction of $O_2(Y_{O_2})$, and flow velocity magnitude in the presence of the magnetic field of the permanent magnets located at the flame burner exit are presented in Figure 4.8.a, Figure 4.8.b, and Figure 4.8.c respectively.

From Equation 3.14., the presence of magnetic fields in the flame vicinity induce an additional body force acting on the paramagnetic species of the flame. Depending on the value of the magnetic field gradients imposed on the flame, the body force acting on the flow field either increases or decreases. This is due to the magnetic field gradient

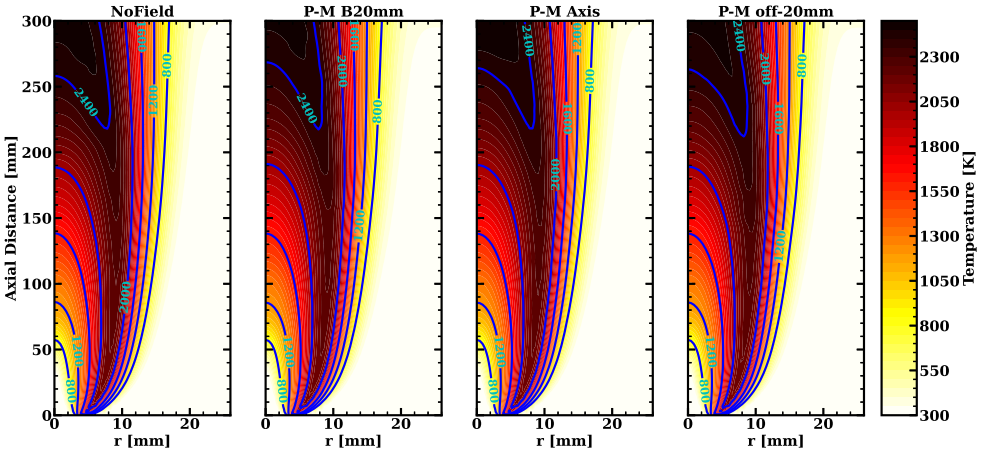

(a) Variation of temperature - T[K]

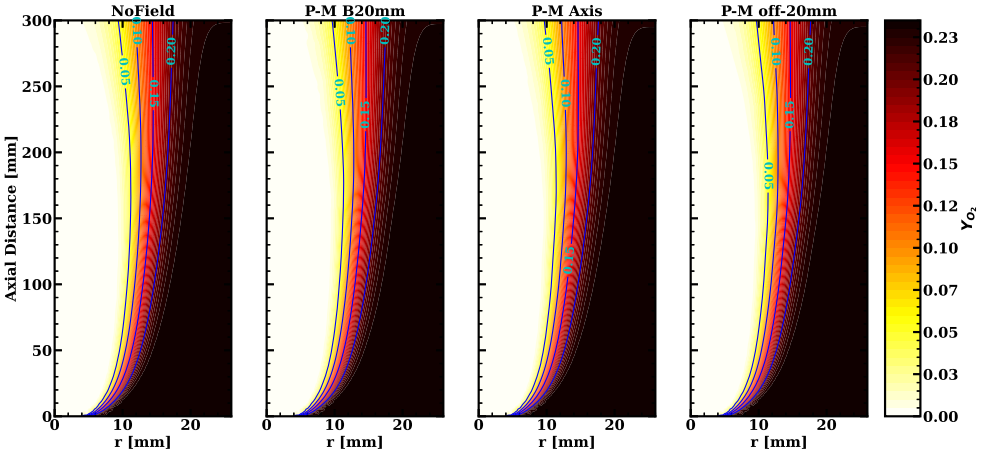

(b) Variation of oxygen mass fraction - $Y_{O_2}[-]$

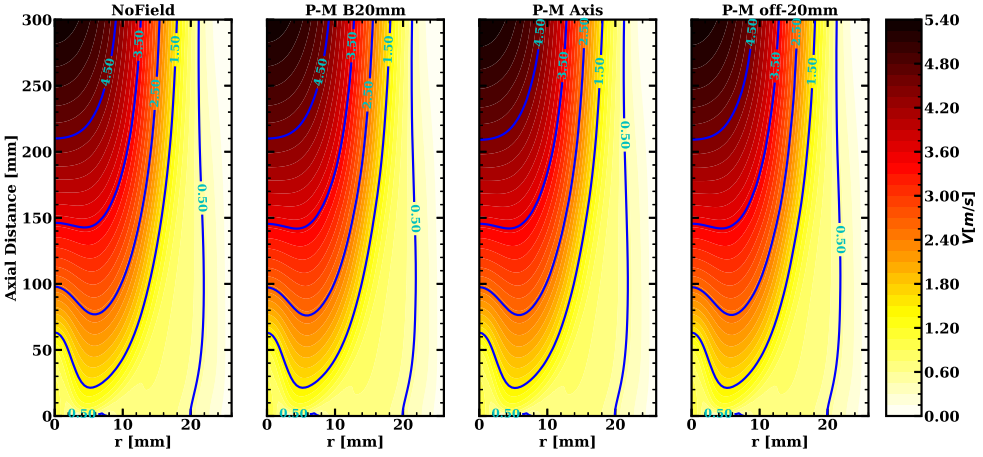

(c) Variation of the magnitude of velocity - V[m/s]

Figure 4.8. Flowfield variation of non-premixed C_3H_8 - Air flames in the presence of a permanent magnetic field located at the flame burner exit.

being negative or positive respectively. A positive magnetic field gradient decreases the body force while negative magnetic field gradient increases the body force acting on the flame.

Considering the location of the flame burner exit plane with respect to the peak magnetic field imposed such that the location of the peak magnetic field imposed is given in Table 4.1., the induced body force acting the flame varies downstream from the burner exit plane. The variation of the induced body force affects the diffusion of the combustion species, thus the combustion reaction. Although the effect of the imposed magnetic field on the flame characteristics shown in Figure 4.8. is less pronounced, the magnetic field imposed on the flame affected the variation of the flame temperature in contrast to the absence of magnetic field. The location of the peak temperature of the flame increased with the presence of the magnetic field due to the migration of the combustion species downstream as the body force increases in relation to the imposed magnetic field gradients which promotes the oxidation of the carbon containing species. In addition to the effect of magnetic field on the location of the peak temperature, the spread of the variation of the flame temperature increased due to the presence of magnetic field.

Table 4.1. Location of the peak magnetic field $\mathbf{B}$ and magnetic field gradient $\nabla(\mathbf{B}^2)$ for each configuration of the burner exit location.

Configuration	P-M Axis	P-M B20mm[mm]	P-M Off-20mm [mm]
$\lvert\mathbf{B}\rvert_{max}$	0	20	-20
$\nabla(\mathbf{B}^2)_{max+}$	-20	0	-40
$\nabla(\mathbf{B}^2)_{max-}$	20	40	0

Due to the variation of the magnetic field gradient imposed on the flame in relation to the location of burner exit, the effect is less pronounced when the burner exit is offset 20 mm below the central axis of the magnets in comparison to other configurations. This is due to the decreased body force imposed on the flow close to the burner exit, which deters the combustion process. However, the effect of the magnetic field on temperature is less pronounced due to the magnitude of the imposed magnetic field gradient in this

case. Similarly, the variation of Y_{O_2} contracts towards the central axis of the flow due to the presence of magnetic field as shown in Figure 4.8.b by tracing the contour of $Y_{O_2} = 0.1$.

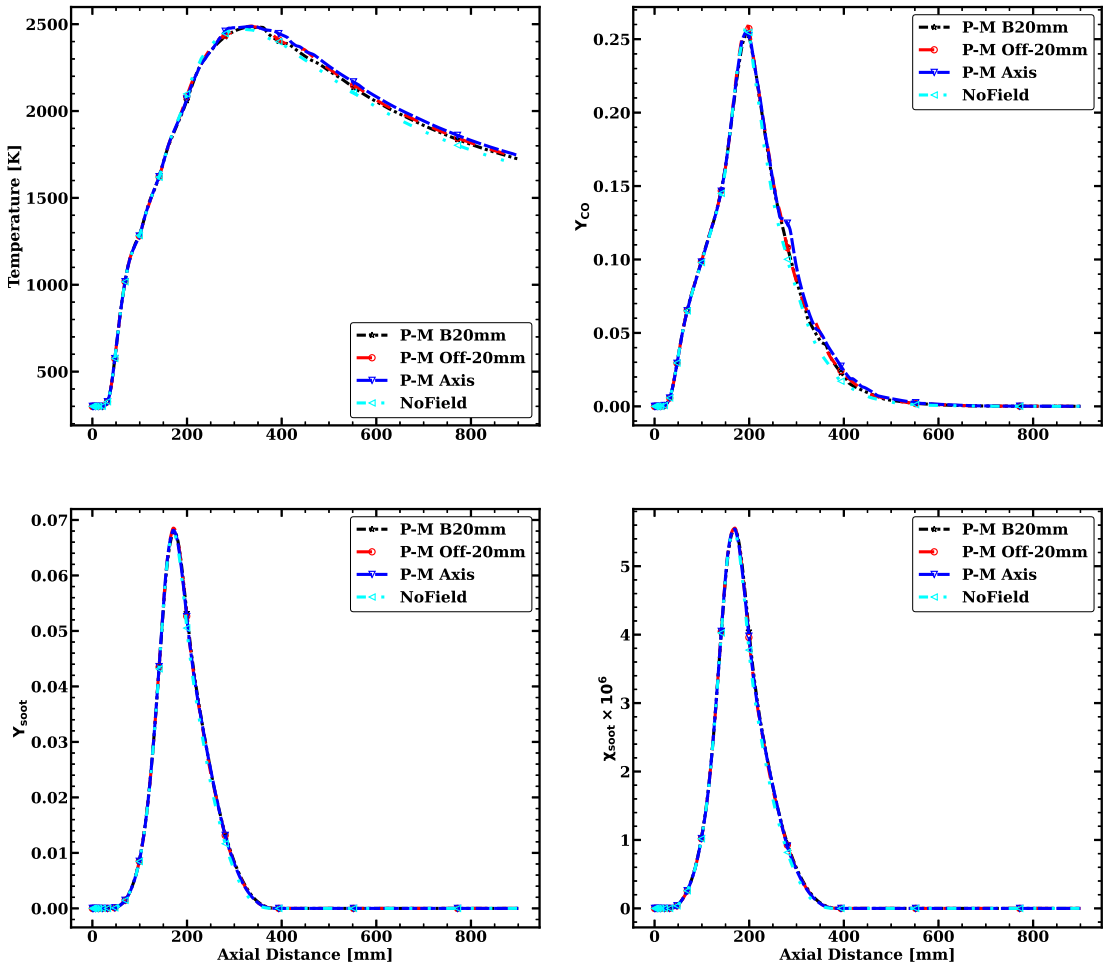

Figure 4.9. Axial variation of the effect of magnetic field placed at the flame burner exit on the non-premixed flames.

Figure 4.9. shows the variation of temperature, mass fraction of CO (Y_{CO}), soot mass fraction (Y_{soot}), and soot volume fraction (f_v) respectively along the centerline of the flame in the absence of the magnetic field and when the flame burner exit is located at different locations with the magnetic fields from the permanent magnets. There is a slight difference in the variation of the flame characteristics due to the presence of the magnetic field. The impact of the magnetic field on the axial variation is insignificant due to the magnitude of the imposed magnetic field gradient.

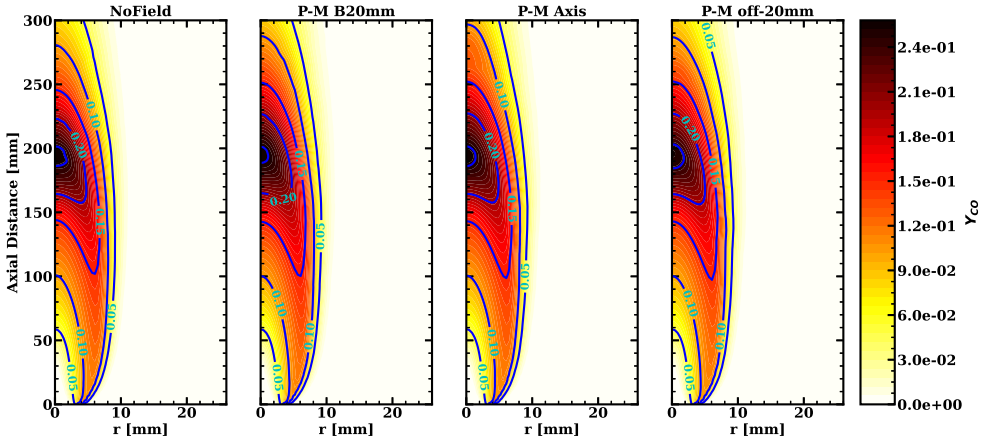

(a) Variation of the mass fraction of CO - $Y_{CO}[-]$

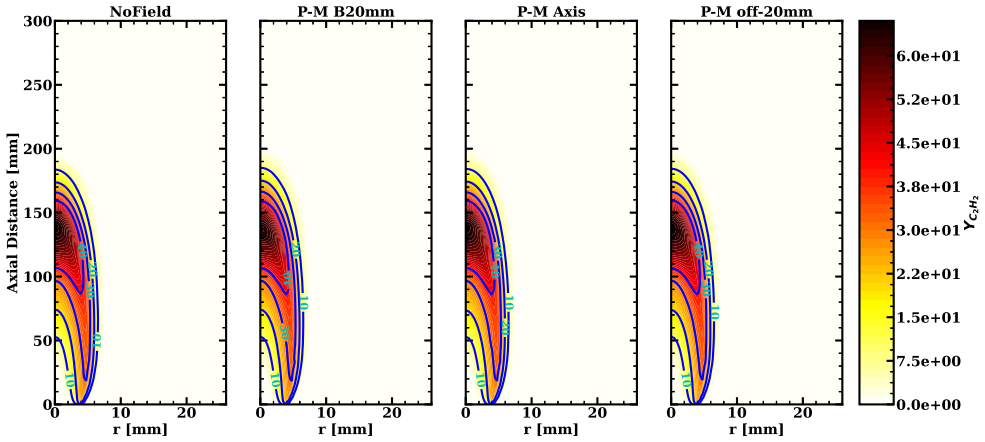

(b) Variation of the mass fraction of acetylene - $Y_{C_2H_2}[-]$

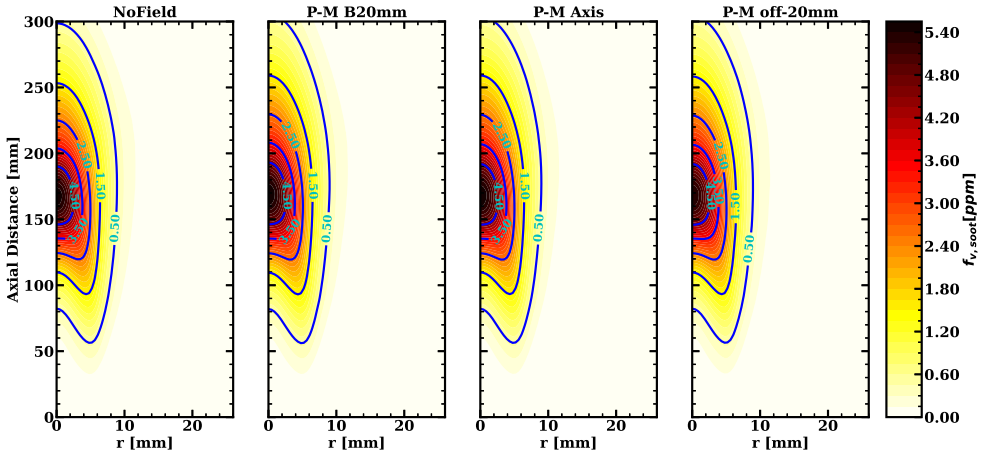

(c) Variation of the soot volume fraction - $\chi_{soot}[-]$.

Figure 4.10. Variation of the Y_{CO}, C_2H_2, and f_v in non-premixed C_3H_8 - Air flames in the presence of the permanent magnets located at the flame burner exit.

Figure 4.10. shows the effect of magnetic field on CO and soot generated by C_3H_8 - air non-premixed flames in the vicinity of infinitely wide permanent magnets. As

shown, the induced magnetic body force acting on the flame affected the spatial variation of the CO mass fraction (Y_{CO}), C_2H_2 mass fraction ($Y_{C_2H_2}$), and soot volume fraction (f_v). Although the effect of the imposed magnetic field shown in Figure 4.10. is minimal - due to the magnitude of the magnetic field gradient imposed, the presence of the magnetic fields increased the region of CO and soot formation in comparison to the absence of the magnetic field. This dispersion depends on the location of the burner exit within the magnetic field and the location of the peak magnetic field gradient imposed on the flame with respect to the flame burner exit locations as provided in Table 4.1..

As the flame burner exit translates downstream across the permanent magnets, the radial dispersion of the flame characteristics varies due to the relative position of the peak magnetic field gradient imposed. The presence of magnetic field in the vicinity of the flame affected the dispersion of Y_{CO} generated by the flame as shown in Figure 4.10.a. Although the effect is minimal, the contour plot of Y_{CO} indicates that the variation of Y_{CO} spread-out in the presence of the permanent magnets in comparison to the contour plot obtained in the absence of the magnetic field. This displacement correlates with the displacement of Y_{O_2} shown in Figure 4.8.b which is due to the variation of the magnetic field gradient imposed. The presence of a negative magnetic field gradient induced a displacement of the O_2 species towards the flame which further promotes the oxidation of CO to CO_2. However, the opposite is the case in the presence of positive magnetic field gradient.

The presence of the magnetic field gradient which distorts the variation of Y_{CO} resulted in an increased average CO produced during the combustion process as shown in Figure 4.12.. This is due to the promoted oxidation of the carbon filled species of the flame such as soot induced by the presence of the magnetic field. Figure 4.11. shows the area integrated average Y_{CO} of the non-premixed flame in the presence of the infinitely wide permanent magnets. The peak value shown corresponds to the location of the peak

flame temperature.

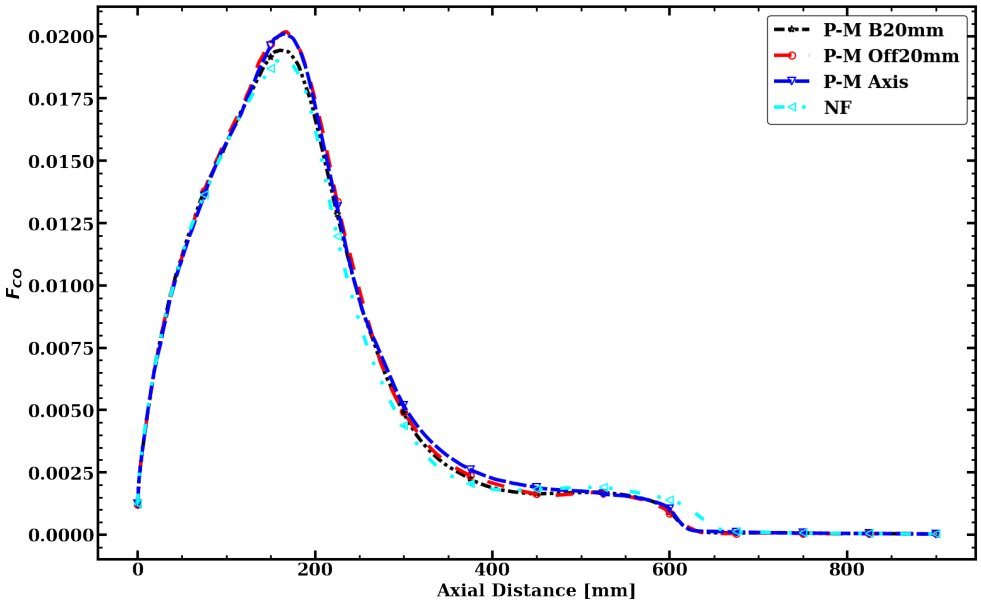

Figure 4.11. Variation of the radial integrated average of CO mass fraction of the flame for $V_{C_3H_8}$ = 0.493 m/s in the presence of the infinitely wide permanent magnet .

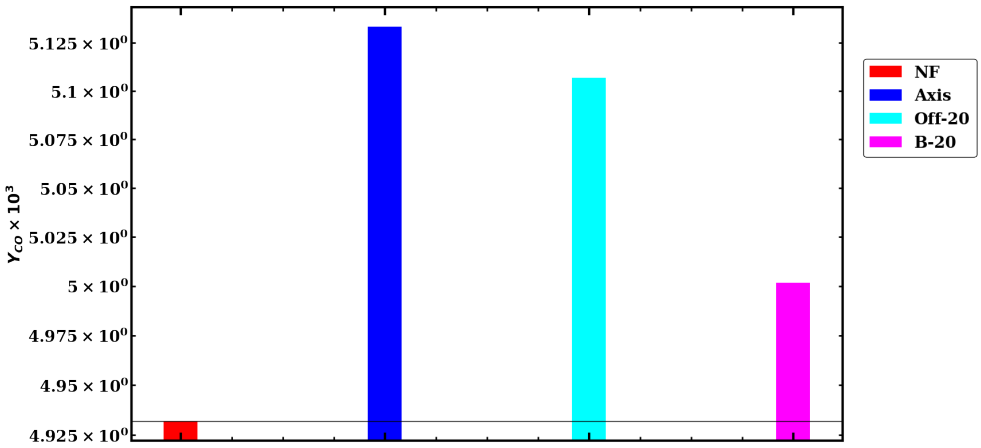

Figure 4.12. Average CO mass fraction due to the imposed magnetic fields of the flame in the presence of the infinitely wide permanent magnets.

Figure 4.10.b shows the variation of $Y_{C_2H_2}$ in the presence of the infinitely wide permanent magnets. This indicates that the variation of $Y_{C_2H_2}$ in the flame are affected by the presence of magnetic field around the burner exit. Around the burner exit plane, the variation of $Y_{C_2H_2}$ in the flame is slightly affected when the burner exit is located 20mm below the central axis (P-M B20mm) of the infinitely wide permanent

magnet. However, at other burner exit location within the magnetic field minimal effect is observed. Since the peak magnetic field gradient imposed on the flame is positive when the burner exit is located at 20mm below the central axis, the combustion is impeded due to reduced convection flow in that region. This thus promotes the formation of C_2H_2 close to the burner exit as shown. However, the region of peak temperature which promotes the formation C_2H_2 is minimally affected by the presence of the magnetic field because the magnetic field gradients are negligible in this region.

Since C_2H_2 is the species assumed to be responsible for the formation of soot nuclei - incipient soot particle, the presence of magnetic field affects the formation of soot as shown in Figure 4.10.c. Due to less significant impact of the magnetic field on the migration of oxidizing species in the flame, the soot formation and oxidation process are slightly impacted by the presence of the imposed magnetic fields, though slight visible shift of the f_v is observed in Figure 4.10.c.

The effect of the magnetic field on soot is quantified by computing the area averaged integrated soot volume fraction F_v as a function of axial distance (z) using

$$F_v(z) = \frac{1}{A_c}\int_S f_v dA_c = \frac{2}{R_{air}^2}\int_0^{R_{air}} r f_v dr \tag{4.2.}$$

The variation of the area averaged integrated soot volume fraction $F_v(z)$ due to the presence of magnetic field is shown in Figure 4.13..

The effect of the imposed magnetic field on the amount of soot produced by the non-premixed flame is considered by computing the volume average soot volume fraction generated by the flame. The volume average soot volume fraction generated by the flame is given as

$$\Phi_s = \frac{1}{V}\int_V f_v dV \tag{4.3.}$$

As shown in Figure 4.14., the magnetic fields imposed on the non-premixed flame generated less soot when the flame burner exit is at the axis of the magnets and at off20

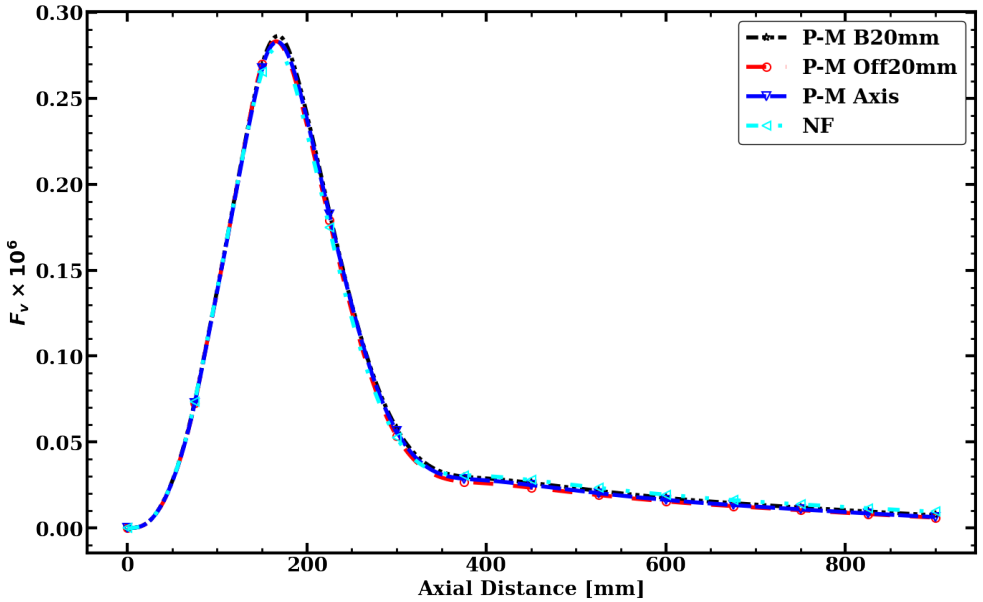

Figure 4.13. Variation of the area averaged integrated soot volume fraction for $V_{C_3H_8}$ = 0.493 m/s in the presence of an infinitely wide permanent magnet .

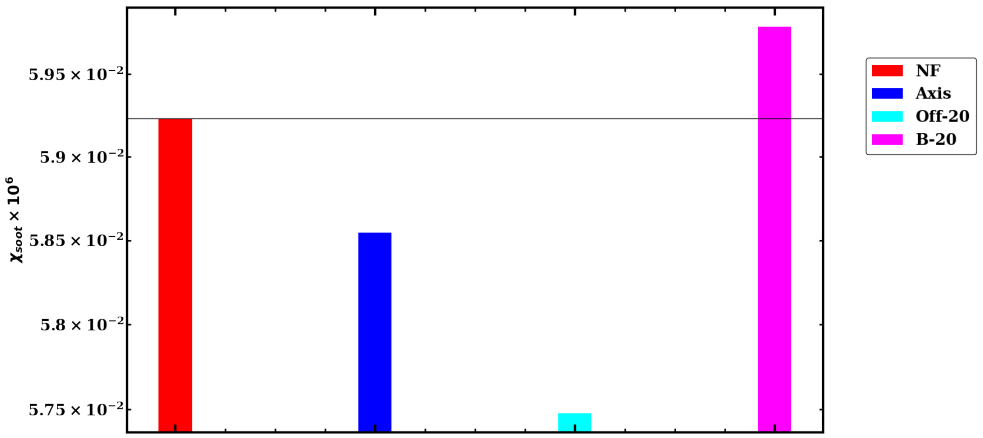

Figure 4.14. Volume average soot volume fraction due to the imposed magnetic fields for $V_{C_3H_8}$ = 0.493 m/s in the presence of an infinitely wide permanent magnet .

than without the magnetic fields. However, the amount of soot generated is higher when the flame burner exit is located below the axis of the magnets.

4.3.3.2. Magnetic Field Imposed at the Flame Tip

A pair of infinitely wide permanent magnets in the vicinity of a non-premixed flame such that the flame tip is located at the distances given in Table 4.2. from the axis of the permanent magnets. The flame characteristics were computed using the models described in Chapter3.. This ensures that the magnetic field is imposed in the region

where the pollutants formation is prominent during the combustion process.

Table 4.2. Location of the flame tip with respect to the axis of the infinitely wide permanent magnets.

Label	P-M B20mm	P-M Axis	P-M Off-20mm
Offset [mm]	-20	0	20

The computed variation of the temperature, mass fraction of O_2 (Y_{O_2}), and flow velocity magnitude in the presence of the magnetic field are shown in Figures 4.15.a, 4.15.b, and 4.15.c respectively. Although the impact of the imposed magnetic field on the variation of the flame characteristics is not noticeable, slight deviations of the contour plots are observed such as the width of the contour region of the peak temperature. The variation of the mass fraction of CO (Y_{CO}), mass fraction of C_2H_2 ($Y_{C_2H_2}$), and the soot volume fraction (f_v) are depicted in Figure 4.16.a, Figure 4.16.b, and Figure 4.16.c respectively. The presence of the magnetic field in the vicinity of the flame tip induced additional body forces which reduces the net body forces in the fluid domain and increases downstream from the axis of the permanent magnets. The resulting effect is due to the interaction of the magnetic field with the paramagnetic species of the flames.

In Figure 4.16.a, the imposed magnetic fields distorted the diffusion pathway of the paramagnetic species which affected the region of CO formation which increased due to the migration of the paramagnetic species away from the reaction zone due to the imposed positive magnetic field gradient. Similarly, the magnetic fields affected the region of soot formation as shown in Figure 4.16.c. The region of soot formation increased due to the magnetic fields. This effect correlates to the effect of the magentic fields on the paramagnetic species. However, the effect of the magnetic field on the region of C_2H_2 formation correlates with the effect on soot formation. Although C_2H_2 is the incipient soot particle used in this model, the soot formation process depends on other processes such as soot oxidation which are affected by the availability of O_2. As a result, the magnetic field affects the soot formation process because the presence

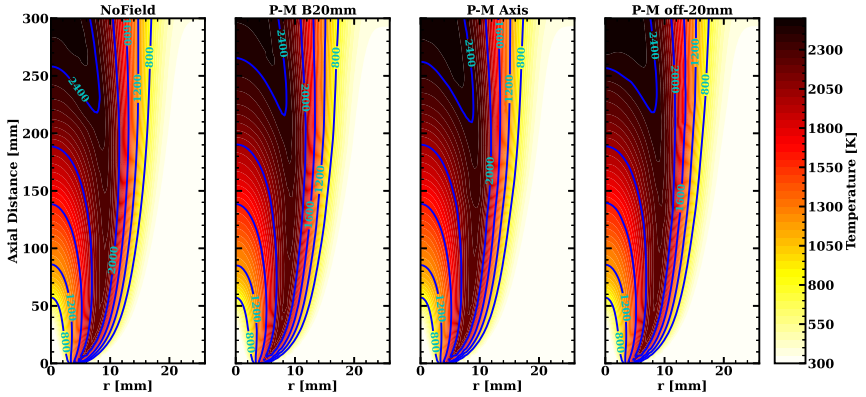

(a) Variation of temperature - T[K]

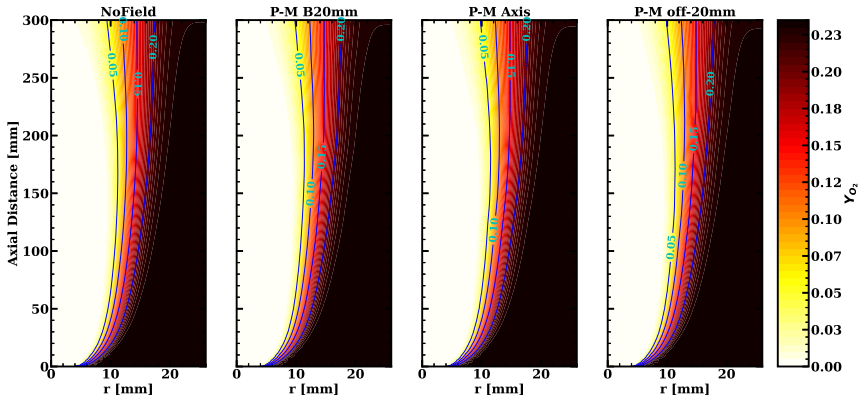

(b) Variation of oxygen mass fraction - $Y_{O_2}[-]$

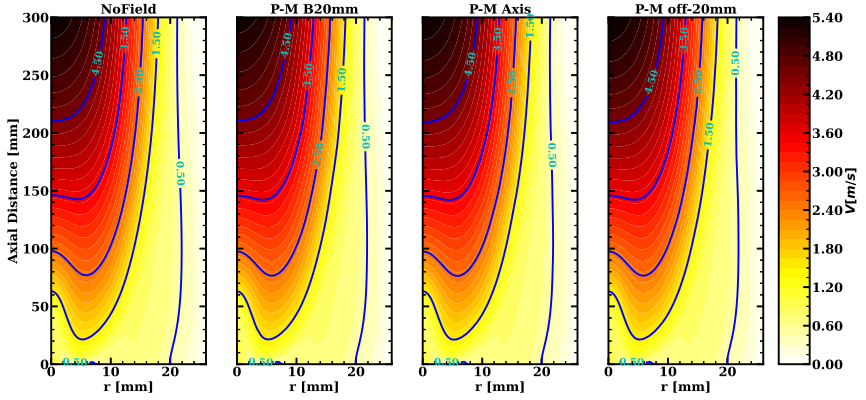

(c) Variation of the magnitude of velocity - V[m/s]

Figure 4.15. Flowfield variation of a non-premixed C_3H_8 - Air flames in the presence of a permanent magnetic field placed around the flame tip.

of magnetic field gradient in the vicinity of the flame distorts the variation of O_2 mass fraction in the flame domain.

The area average and volume average of the CO formed during the combustion process is shown in Figure 4.17. and Figure 4.18. respectively. The presence of a

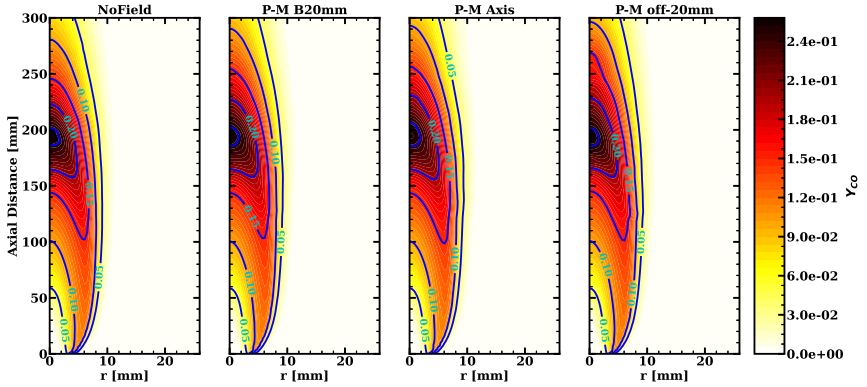

(a) Variation of the mass fraction of CO - $Y_{CO}[-]$

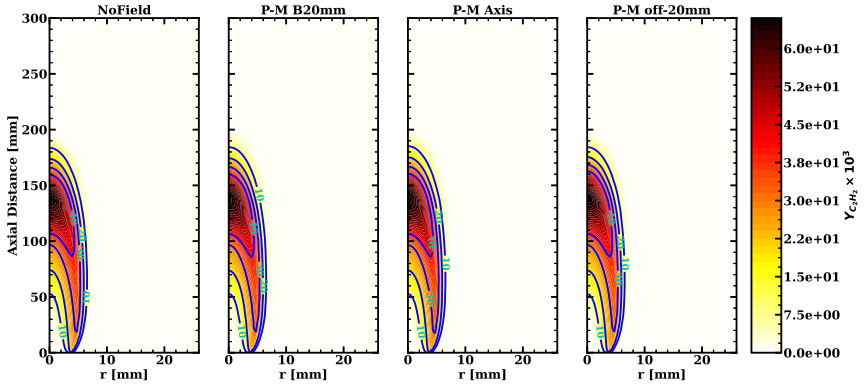

(b) Variation of the mass fraction of acetylene - $Y_{C_2H_2}[-]$

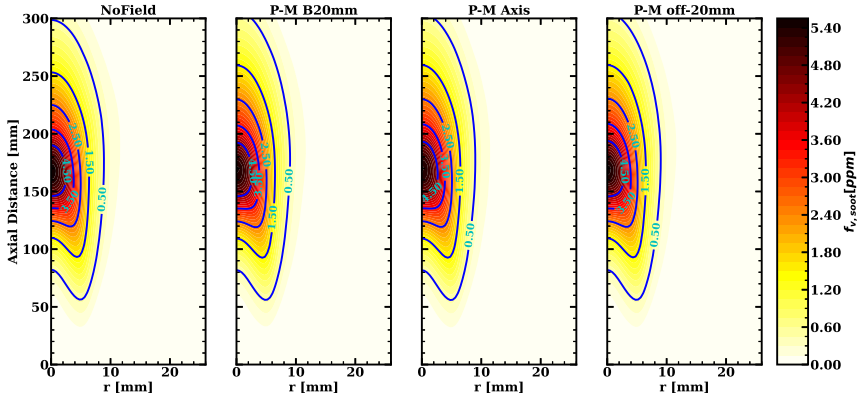

(c) Variation of the soot volume fraction - $\chi_{soot}[-]$.

Figure 4.16. Variation of the Y_{CO}, C_2H_2, and f_v in non-premixed C_3H_8 - Air flames in the presence of the permanent magnets placed around the flame tip.

magnetic field around the flame tip increased the amount of CO formed by the non-premixed flame. However, the magnetic field imposed decreased the amount of soot formed by the non-premixed flame as shown in Figure 4.19. and Figure 4.20..

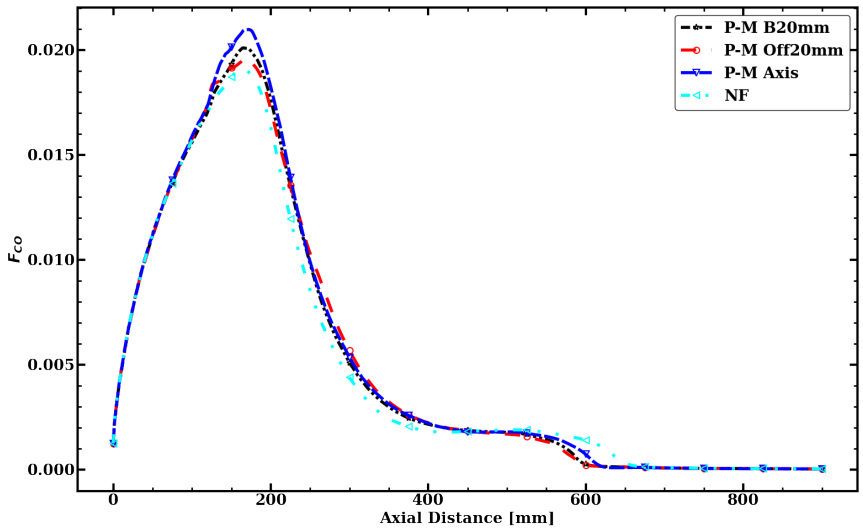

Figure 4.17. Variation of the radial integrated average of CO mass fraction of the flame for $V_{C_3H_8}$ = 0.493 m/s in the presence of the infinitely wide permanent magnet placed around the flame tip.

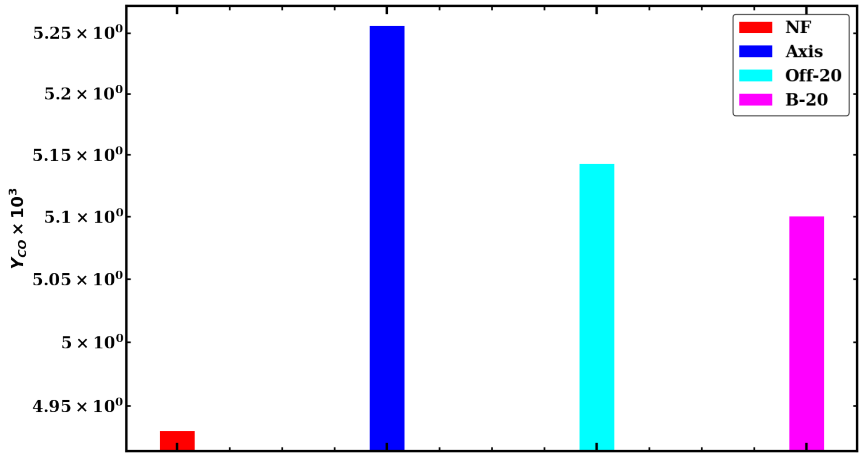

Figure 4.18. Average CO mass fraction due to the imposed magnetic fields of the flame in the presence of the infinitely wide permanent magnets placed around the flame tip.

4.3.3.3. Relationship between the Magnetic Field Effect and Flame Size

To study the relationship between the magnetic field effect and the flame size (fuel velocity), the computation is conducted such that the average fuel inlet velocity is reduced to 0.2 m/s in the presence of the magnetic field generated by the infinitely wide permanent magnet.

The flame temperature is shown in Figure 4.21.a while Figure 4.21.b depicts the soot volume fraction obtained from the computation. Figure 4.21.c is the variation of

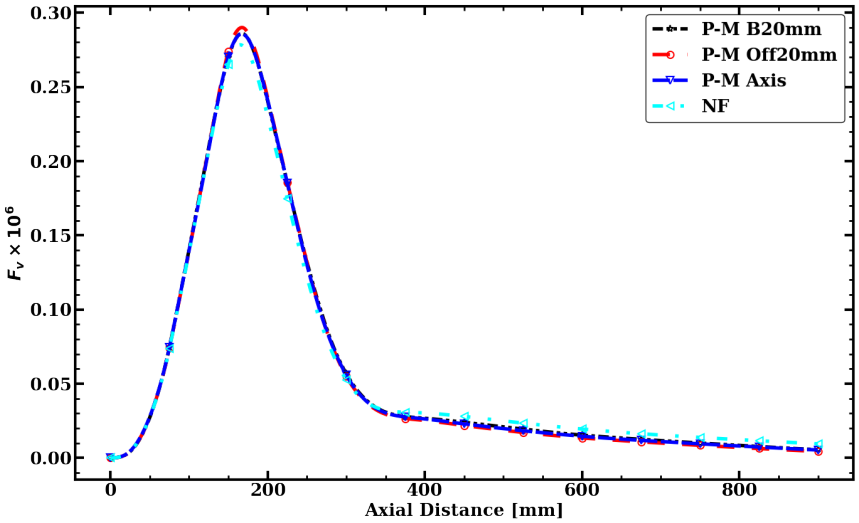

Figure 4.19. Variation of the area averaged integrated soot volume fraction for $V_{C_3H_8}$ = 0.493 m/s in the presence of an infinitely wide permanent magnet placed around the flame tip.

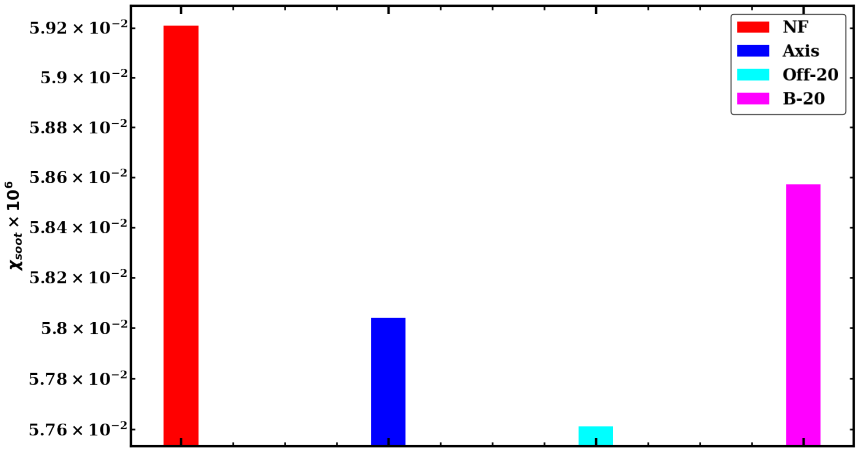

Figure 4.20. Volume average soot volume fraction due to the imposed magnetic fields for $V_{C_3H_8}$ = 0.493 m/s in the presence of an infinitely wide permanent magnet placed around the flame tip.

the mass fraction of CO in the presence of the infinitely wide permanent magnets. The flame length computed for this flow condition is ≈ 30 mm in the absence of the magnetic field.

In the presence of the infinitely wide permanent magnets, the radial outward displacement of oxygen impede the oxidation of soot which resulted an increased average soot volume fraction. However, the displacement of O_2 due to the magnetic field imposed induced a reduction of average CO mass fraction when the burner exit is

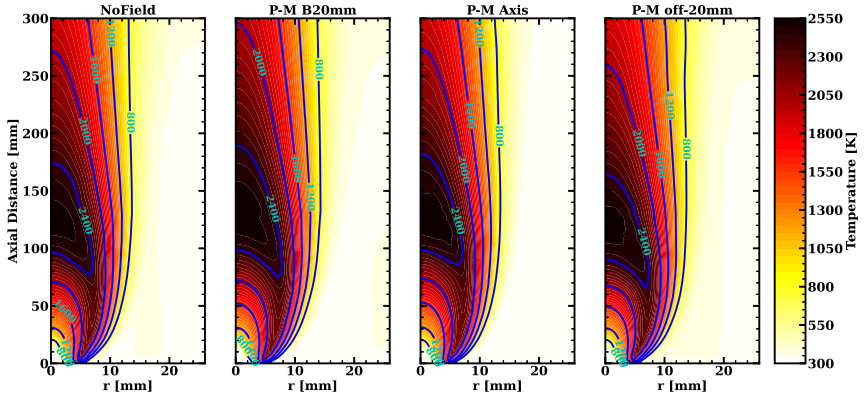

(a) Variation of temperature T[K] .

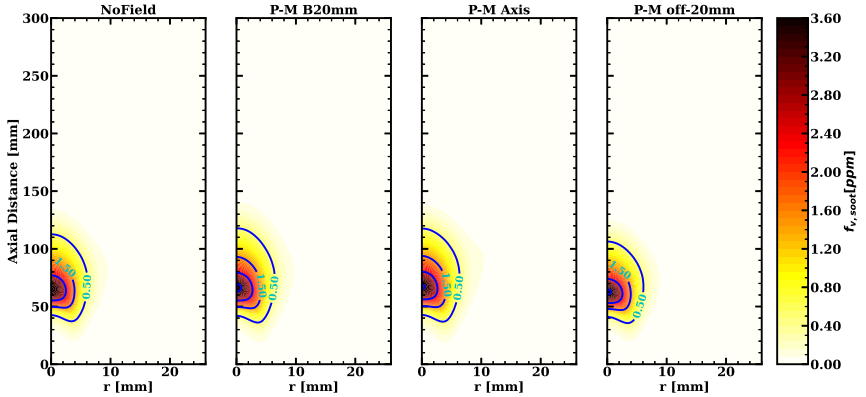

(b) Variation of soot volume fraction variation $\chi_s[-]$.

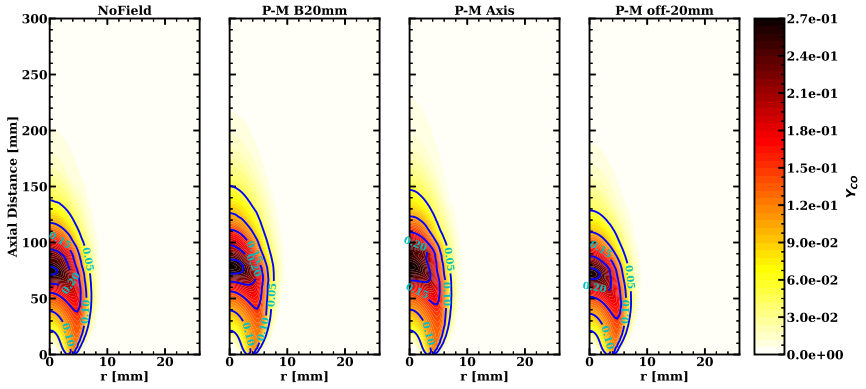

(c) Variation of the mass fraction of CO $Y_{CO}[-]$.

Figure 4.21. Variation of flame characteristics of the C_3H_8 non-premixed flame in the presence of the infinitely wide permanent magnet located at the flame burner exit for $V_{C_3H_8} = 0.2\,m/s$

located at 20 mm but an increase in average CO mass fraction when the burner exit is located at the center of the permanent magnet. This occurs because the presence of the magnetic field induced the radial displace of the oxidizer in the region of the flame

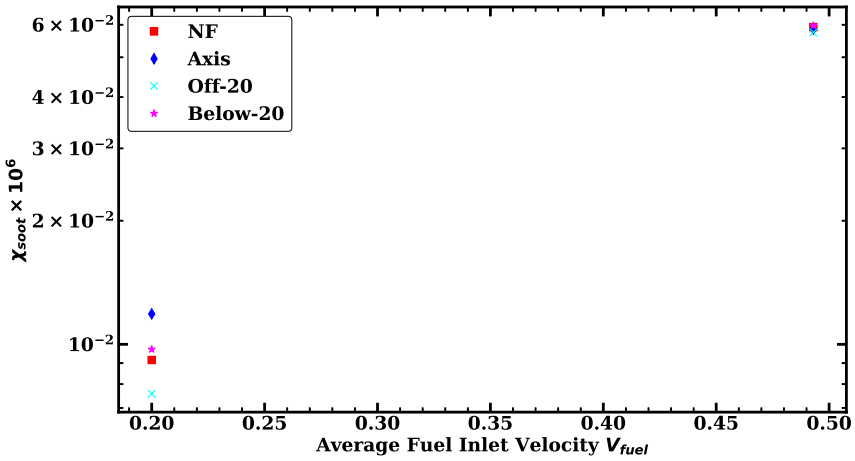

Figure 4.22. Effect of flame size on soot formation in the presence of an infinitely wide permanent magnet located at the flame burner exit.

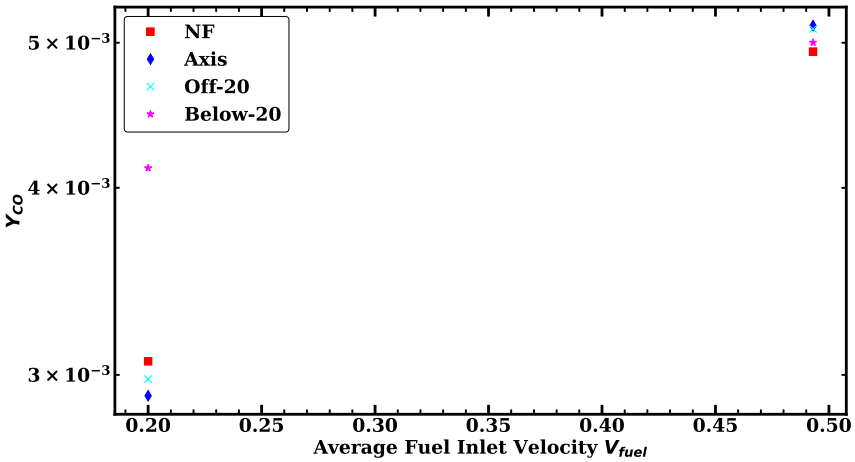

Figure 4.23. Effect of the flame size on CO formation in the presence of the infinitely wide permanent magnets located at the flame burner exit.

when the burner tip is located at the axis of the permanent magnet. However, the radial displacement of the oxidizer in the region of the flame decreased when the flame is located downstream at 20 mm, which promoted the oxidation of CO.

With respect to the flame size, the effect of the magnetic field on the soot formation and CO decreases as the flame size increases as shown in Figure 4.22. and Figure 4.23. respectively. This is due to the fact that the flame forms in the region where the oxidizers are displaced radially outward due to the presence of the magnetic field.

4.4. Conclusions

The effect of a magnetic field of an infinitely wide permanent magnet on the formation of CO and soot is studied numerically. In addition, the relationship between the location of the burner exit plane and the magnetic field effect on CO and soot is analyzed. Moreover, the effect of flame size on the resulting magnetic field effect on soot and CO is also studied.

Results demonstrate that the presence of a magnetic field in the vicinity of the flame distorts the flame characteristics. This is due to the variation of the body force acting on the flame due to the presence of the magnetic field. This induced body force either promotes or impedes combustion depending on the magnetic field gradient imposed on the flame. A positive magnetic field gradient decreases the body force in relation to the absence of magnetic fields but the opposite occurs with a negative magnetic field gradient.

Moreover, the formation of CO and soot is affected by the presence of the magnetic field. Although the magnetic field effect on CO and soot observed are minimal for the imposed magnetic field, this is attributed to the magnitude of the imposed magnetic field and the magnetic susceptibility of the paramagnetic species which is inversely proportional to temperature.

The imposed magnetic field decreased the average soot volume fraction formed by the flames over the computational domain in most of the cases studied. However, the average mass fraction of CO formed by most of the flame studied increased by the presence of the magnetic field placed on the flame burner exit.

As the flame size increases, the relative effect of the magnetic field on the formation of CO and soot reduces when the magnets are placed on the flame burner exit. As the flame size increases, the location of formation of soot increases such that the imposed magnetic field gradient envelope is evaded thus reducing the effect of the magnetic field on the formation of soot.

Based on the computation, the location of the flame burner exit dictates the effect of the magnetic field on the formation of pollutants. To promote combustion, the location of the burner exit plane should be located in the region with negative magnetic field gradient to promote convection. However, the magnetic field effect at the location depends on the flame size.

Chapter 5.
Effect of Magnetic Field on Soot Emission and CO from Propane-Air Non-Premixed Flames

The presence of magnetic field around a non-premixed flame affects the formation of soot and CO as presented in chapter 4.. Although the effect was not pronounced due to the magnitude of the imposed magnetic field, an electromagnetic field generated by solenoids is considered here to quantify the effect of magnetic field on soot formation and CO. In addition, the effect of the flame size on the effect of magnetic field on soot formation and CO is studied numerically.

5.1. Problem Formulation and Geometry

The flame configuration is placed in the vicinity of the magnetic field of a copper solenoid coil wound around a cylindrical bracket with inner diameter 200 mm; outer diameter of 300 mm; flange width of 40 mm; thickness of 10 mm; and a height of 200 mm as shown in Figure 5.1.. The diameter of the coil is $\frac{1}{3}$mm.

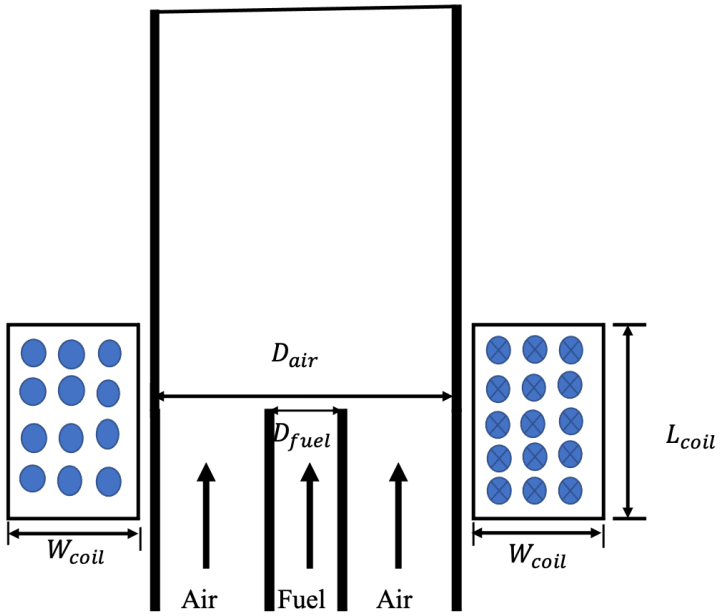

Figure 5.1. Magnetic field from solenoids imposed on non-premixed flame configuration

5.2. Results and Discussion

In this study, the effect of the magnetic field on CO and soot emission with respect to the position of the flame burner exit plane is studied such that the burner exit plane of the coaxial jet flame was positioned at three different locations within the magnetic field of the solenoid coils. The offset distances of the exit plane in the positive direction from the center of the solenoid coil are given in Table 5.1..

Table 5.1. Location of the flame exit with respect to the center of the solenoid coil generating the field

Name	Offset [mm]	Label
Center	0	Axis
Offset 100	100	Off100
Offset 200	200	Off200

The magnetostatic field imposed on the non-premixed flame is generated by a current of 20 A flowing through a copper coil such that the number of turns N is 25 000, 35 000, and 100 000. The computed magnetic field **B** vector generated by the solenoid coils with $N = 1 \times 10^5$ turns of wound copper solenoid coils is shown in Figure 5.2.. Figure 5.2. also depicts the axial variation of the magnetic field **B** and magnetic field gradient $\nabla(\mathbf{B}^2)$ computed by solving Maxwell's equation numerically. The imposed magnetic field gradients have peaks located at approximately 200 mm from the center of the solenoid coil as shown in Figure 5.2..

Figure 5.3.a, Figure 5.3.b, and Figure 5.3.c show the variation of the mass fraction of oxygen (Y_{O_2}), velocity magnitude, and temperature of the non-premixed flame with and without magnetic field respectively.

5.2.1. Effect of Magnetic field on Soot Formation

The prominent disparity of the variation of Y_{O_2} as shown in Figure 5.3.a is found where the peak magnetic field gradients imposed is located on each configuration, which is marked with blue triangles. This region of the flame experiences a positive magnetic field gradient which decreases the buoyant force acting on the flame. This

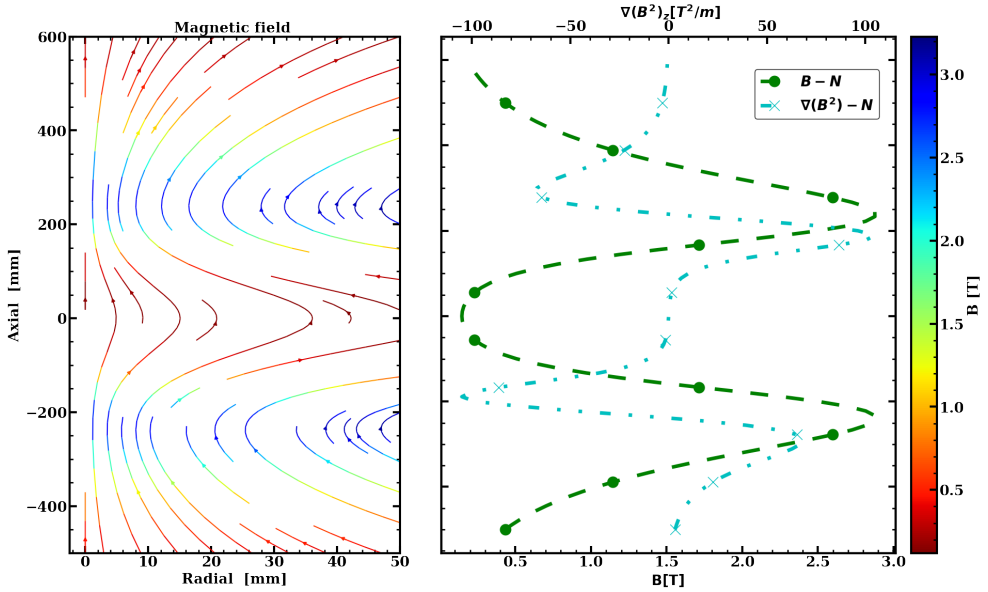

Figure 5.2. Magnetic Field **B** generated by the solenoid coil with $N = 1 \times 10^5$ turns

reduction induces an outward displacement of oxygen species that inhibits the combustion process. Above this peak location downstream, the magnetic field gradient is negative, thus increasing the buoyant force and the combustion process is promoted.

A decrease in the downward buoyant force in the region of the positive magnetic field gradient resulted in an increase in the rate of change of the flow velocity with respect to the axial distance as shown in Figure 5.3.b. In this regard, when the burner exit plane is located at the center of the solenoid, the induced buoyant force was initially negligible over some distance but increases close the peak location. This resulted in a lower average acceleration imposed on the flow, i.e. the average rate of change of the flow velocity in the axial direction is lower than when it is located at an offset of 100 mm.

As shown in Figure 5.3.c, the width of the reaction zone increases in the region of positive magnetic field gradient, which affected the location of the peak temperature. This effect thus determine the location of the incipient soot formation within the flame which is dependent on the peak temperature of the flame.

Soot formation depends on certain processes such as nucleation, surface growth of soot nuclei, coagulation of soot particles, and oxidation [35]. This depends on the

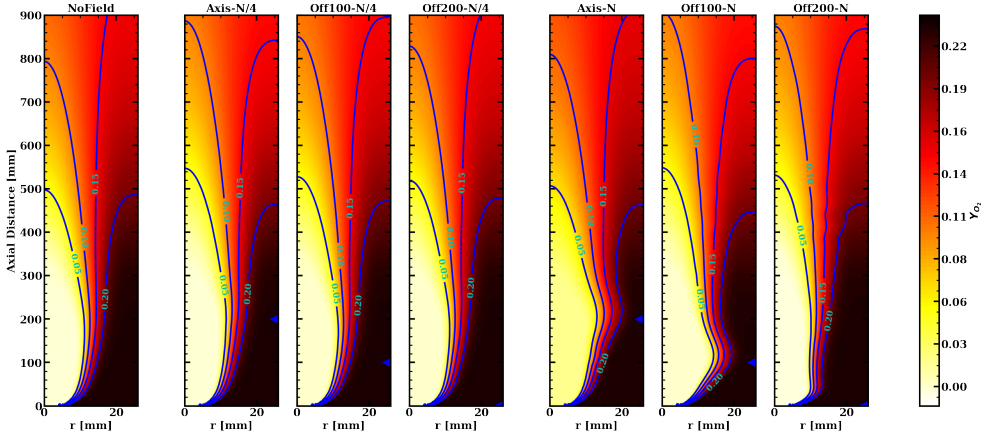

(a) Variation of oxygen mass fraction - Y_{O_2} [−].

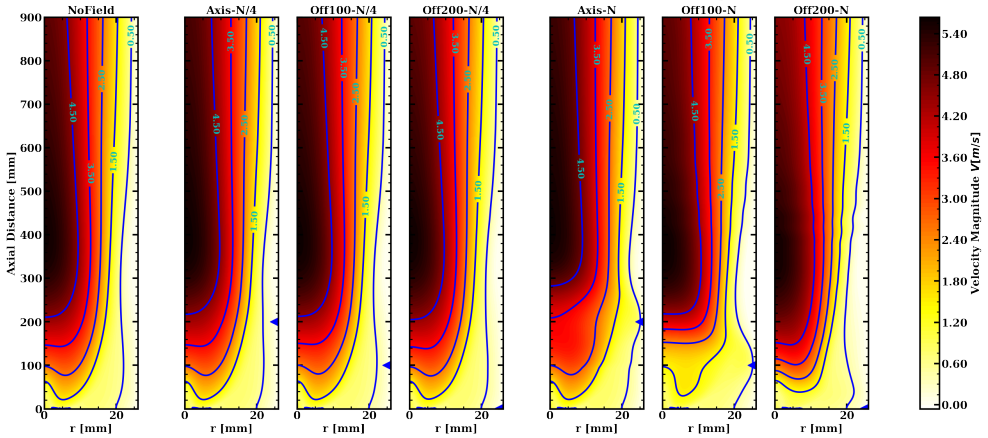

(b) Variation of the magnitude of velocity - V [m/s] .

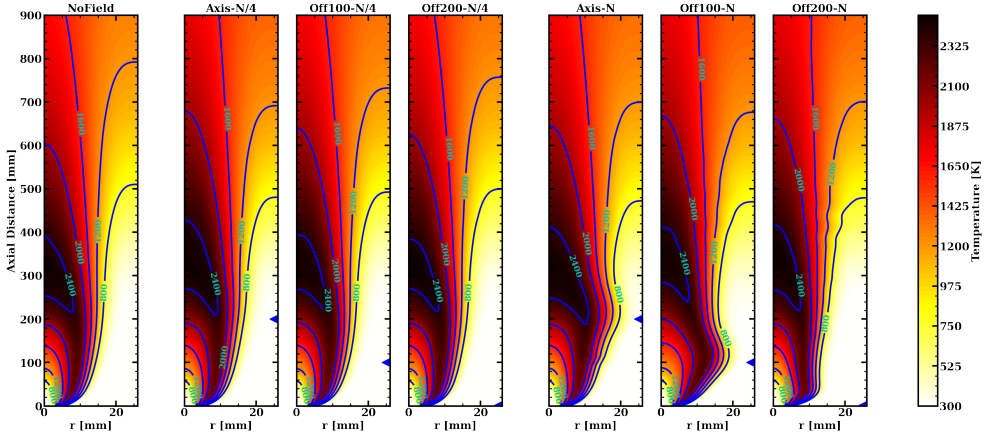

(c) Variation of temperature - T [K] .

Figure 5.3. Flow field variation in non-premixed C_3H_8 - Air flames in the presence of magnetic fields - N = 1×10^5 turns. Triangles mark the locations of the peaks of the magnetic field gradients imposed on the flames.

formation and availability of the soot incipient species. The soot incipient species is assumed to be C_2H_2. The formation of C_2H_2 during the combustion process depends

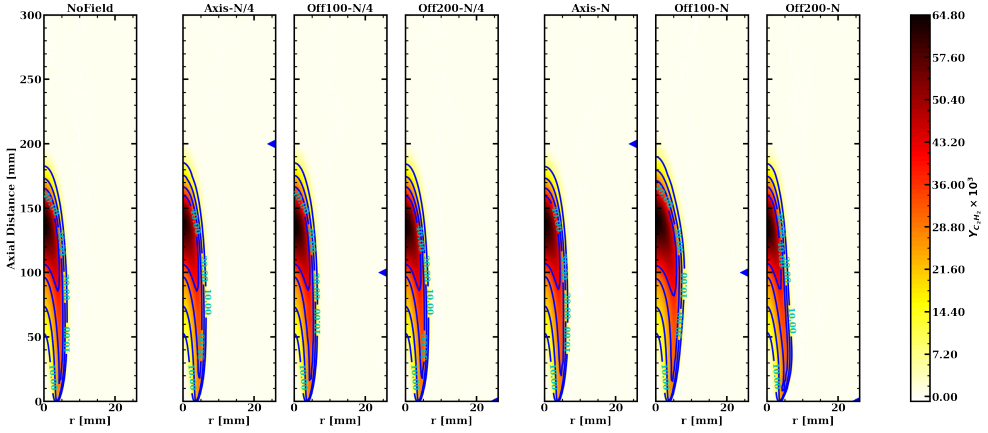

(a) Variation of the mass fraction acetylene - $Y_{C_2H_2}$ [−] .

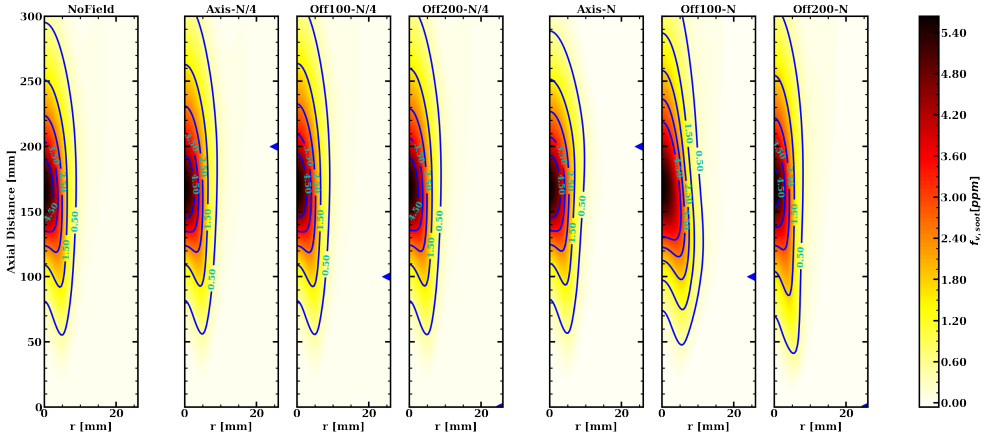

(b) Variation of the soot volume fraction - χ_{soot} [−]

Figure 5.4. Variation of mass fraction / volume fraction in non-premixed C_3H_8 - Air flames in the presence of magnetic fields - N = 1×10^5 turns. Triangles mark the locations of the peaks of the magnetic field gradients imposed on the flames.

on pyrolysis of the fuel - C_3H_8. The region of positive magnetic field gradients promoted the pyrolysis of C_3H_8 due to the radial diffusion of oxygen as shown in Figure 5.3.a, thus resulting in the formation of C_2H_2 as shown in Figure 5.4.a. Based on the location of the burner exit plane, the flame configuration with the burner exit plane located at 100 mm offset from the center of the magnetic field generated more C_2H_2 which resulted in an increased formation of soot as shown in Figure 5.4.b.

As illustrated in the results discussed so far, the effect of magnetic field on the emission of soot is dependent on the magnitude of the magnetic field gradient imposed on the flame. It is noted that Figure 5.3. and Figure 5.4. seem to show little or no

change in the results presented for $\frac{N}{4}$ turns of the solenoid coils, which is due to different magnitude of buoyant forces imposed. For $\frac{N}{4}$ turns, the magnetic field gradient is small in the order of about $O(10^{-1})$ unlike that induced by the N turns which is of the order of magnitude $O(1 \times 10^{1})$.

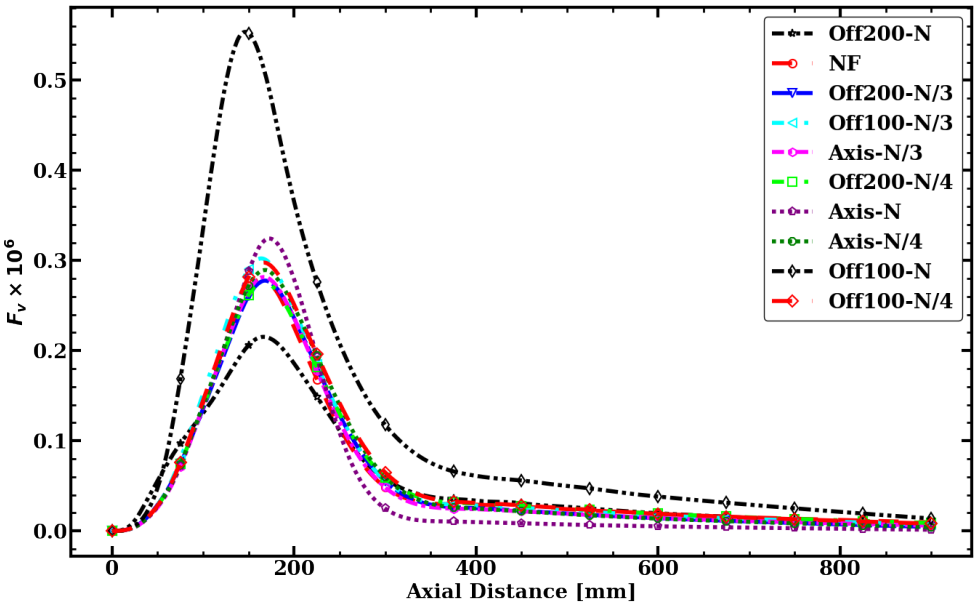

Figure 5.5. Axial variation of the integrated soot volume fraction of the C_3H_8 non-premixed flame

To assess the effect of the magnetic field on the amount of soot generated by the non-premixed flame analyzed in this work, integrated soot volume fractions F_v were computed as

$$F_v = \frac{1}{A_c}\int_S f_v dA_c = \frac{2}{R_{air}^2}\int_0^{R_{air}} r f_v dr \tag{5.1.}$$

The area average integrated soot volume fraction computed based on the analysis is shown in Figure 5.5.. As shown, the integrated soot volume fractions differ based on location and magnitude of the magnetic field and associated resultant buoyant forces.

Figure 5.6. shows the effect of magnetic field on the average soot volume fraction. Results indicate that the soot volume fraction generated increased due to the presence of magnetic field in most of the cases considered. However, a decrease in the average soot

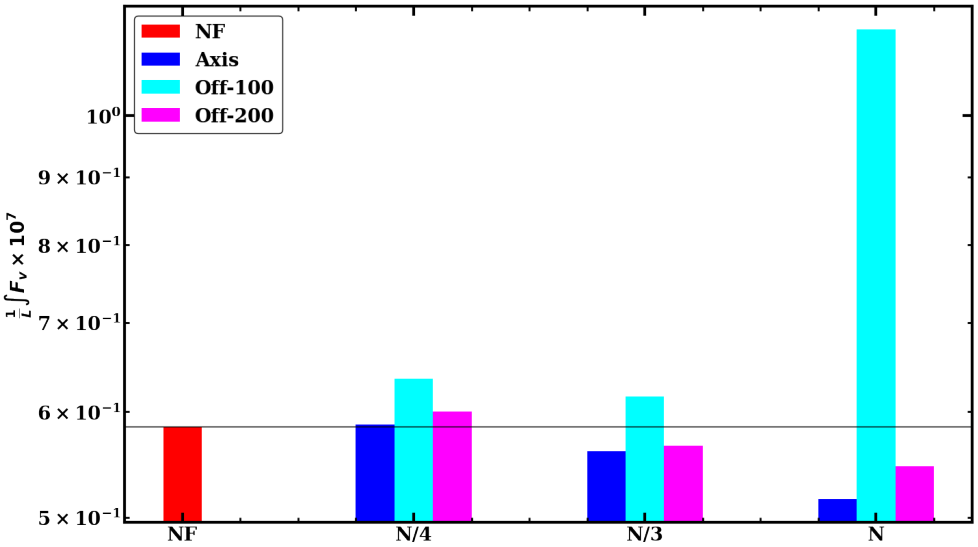

Figure 5.6. Average soot volume fraction due to the imposed magnetic fields

volume fraction was obtained when the magnitude of the magnetic field increased with the flame burner located at the center of the solenoid and at 200mm from the center of the solenoid.

5.2.2. Effect of magnetic field on CO

Figure 5.7. is the spatial variation of CO mass fraction in the presence of magnetic field. The presence of magnetic field in the vicinity of the flame affects the variation of Y_{CO} generated by the flame. The variation correlates with the variation of Y_{O_2} shown in Figure 5.3.a. When the flame burner exit plane is positioned at the center of the solenoid, the presence of magnetic field induced a displacement of the O_2 species towards the flame in the region with negative magnetic field gradients at 200 mm above the center of the solenoid coil, which further promotes the oxidation of CO to CO_2.

The promotion of oxidation of CO by the presence of magnetic field should have reduced the average formation of CO in the flame, but due to the presence of soot formation the average formation of CO increased as shown in Figure 5.9..

Figure 5.8. depicts the area weighted integrated average of Y_{CO} of the flame in the presence of magnetic field. This indicates that the area weighted integrated average of Y_{CO} depends on the magnitude of the magnetic field and also the location of the

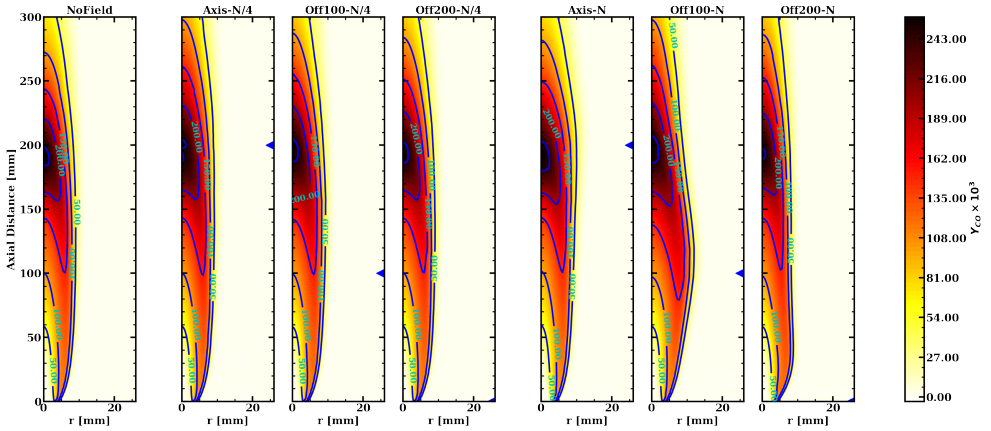

Figure 5.7. Magnetic field effect on the CO mass fraction distribution of the flame for $V_{C_3H_8} = 0.493\,m/s$ in the presence of the magnetic field of the solenoid coils .

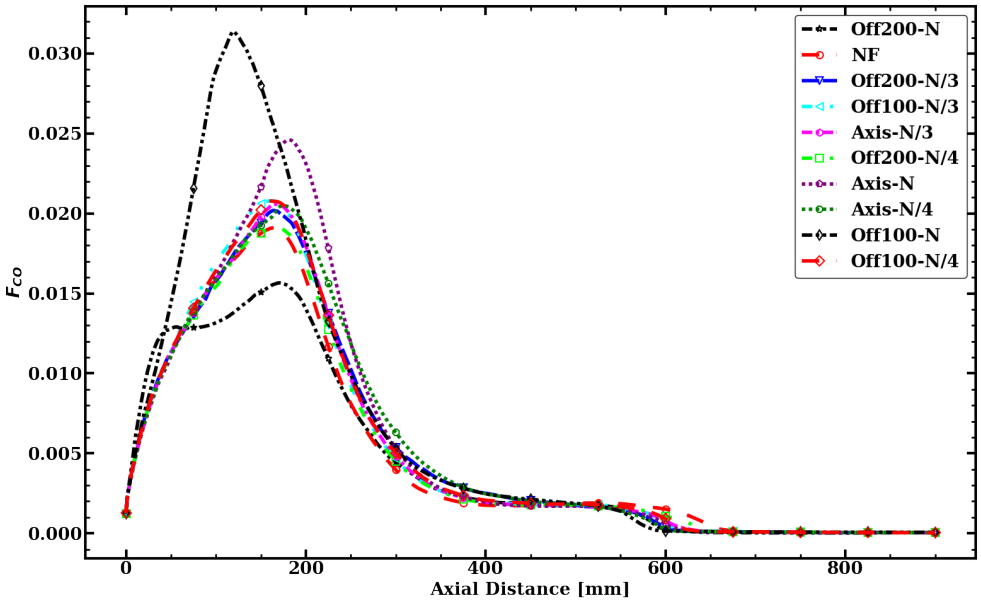

Figure 5.8. Variation of the radial integrated average of CO mass fraction of the flame for $V_{C_3H_8} = 0.493\,m/s$ in the presence of the magnetic field of the solenoid coils.

flame burner exit plane in the magnetic field. Figure 5.9. and Figure 5.10. are volume integrated average of Y_{CO} and percentage change in the volume integrated average of Y_{CO} with respect to the absence of magnetic field respectively. The presence of magnetic field increased the average Y_{CO} generated by the flame for the magnetic fields considered, but decreased when the flame burner exit is located at 200 mm from the center of the solenoid and the number of turns of the coil is N.

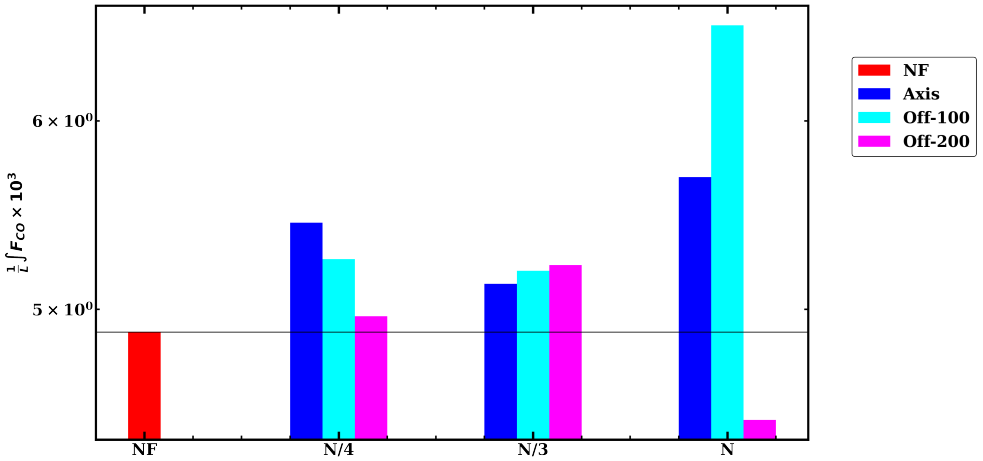

Figure 5.9. Average CO mass fraction due to the imposed magnetic fields of the flame for $V_{C_3H_8} = 0.493\,\text{m/s}$ in the presence of the magnetic field of the solenoid coils.

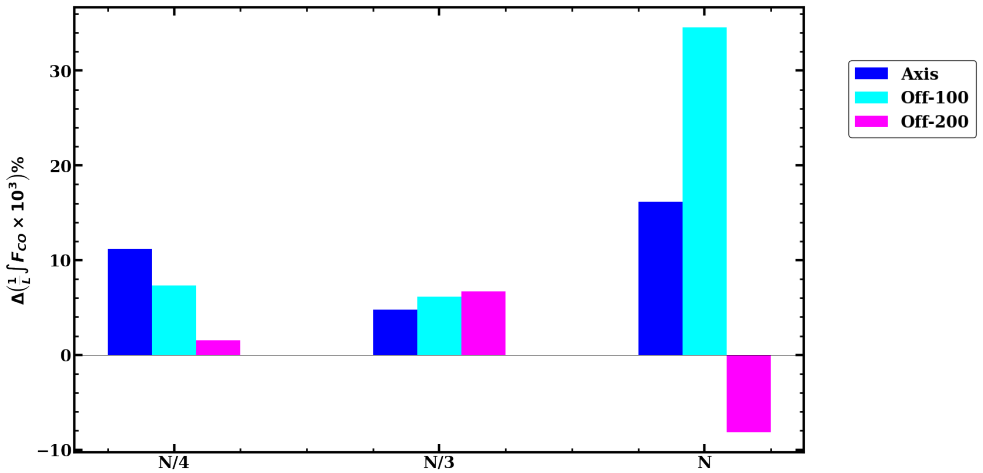

Figure 5.10. Effect of magnetic field on CO mass fraction of the flame for $V_{C_3H_8} = 0.493\,\text{m/s}$ in the presence of the magnetic field of the solenoid coils .

5.2.3. Relationship between the Magnetic Field Effect and Flame Size

The computation of the relationship between the magnetic field effect and the flame size (fuel velocity) is conducted with the fuel velocity of 0.2 m/s in the presence of the magnetic field generated by the solenoid coils of $N = 1 \times 10^5$ turns to determine the effect of the flame size on the magnetic field effect observed.

The flame temperature is shown in Figure 5.11.a and Figure 5.11.b shows the soot volume fraction obtained from the computation. Figure 5.11.c is the mass fraction distribution of CO in the presence of the magnetic field of the solenoid coil. The flame length computed for this flow condition is $\approx 30\,\text{mm}$.

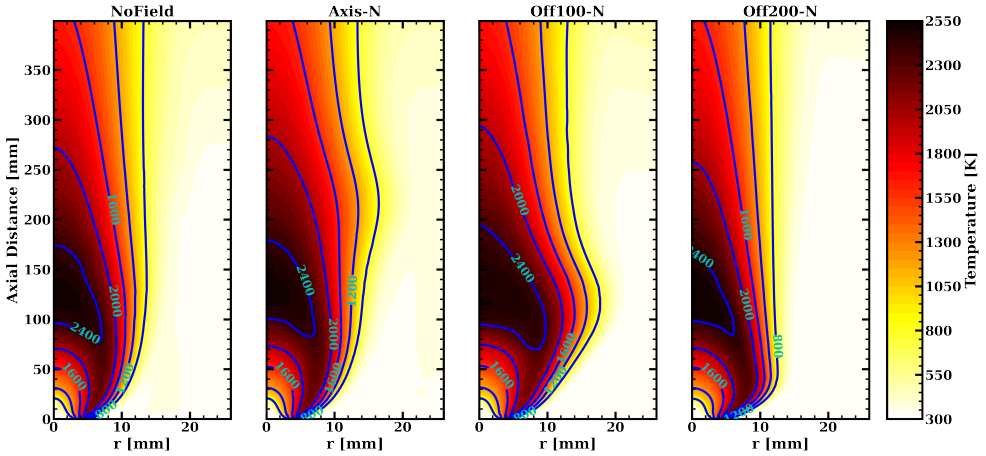

(a) Variation of temperature T[K].

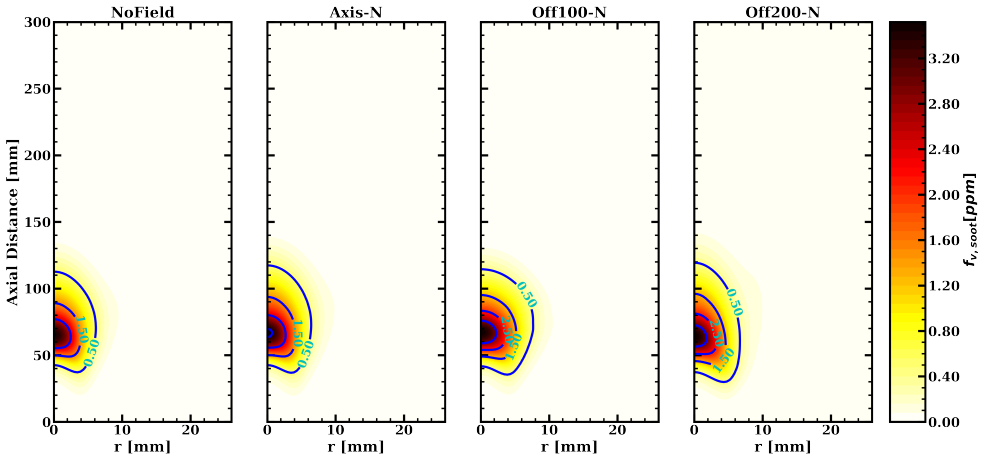

(b) Variation of soot volume fraction χ_{soot}.

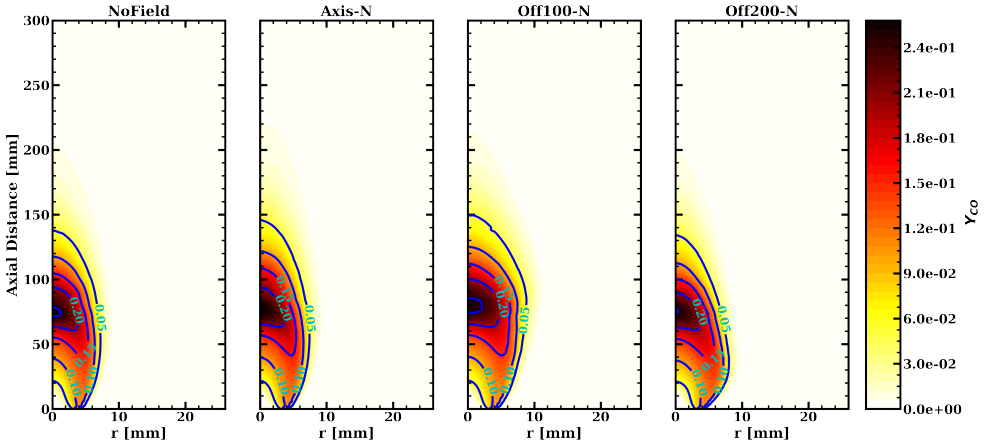

(c) Variation of CO mass fraction $Y_{CO}[-]$

Figure 5.11. Variation of the flame characteristics of C_3H_8 - Air non-premixed flame in the presence of the magnetic field of the solenoid coil for $V_{C_3H_8} = 0.2\,m/s$.

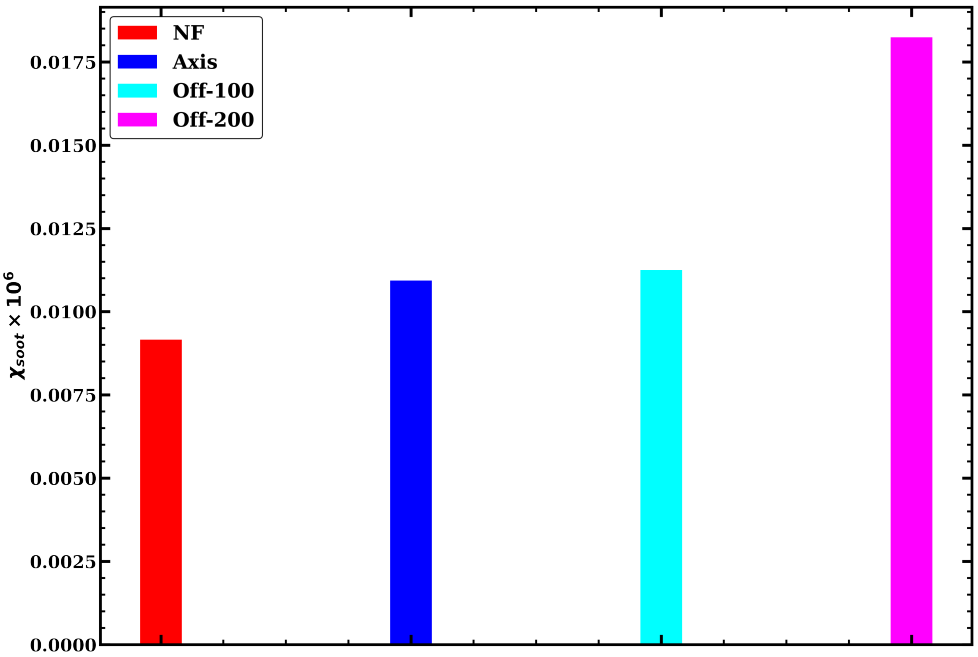

Figure 5.12. Average soot volume fraction due to the imposed magnetic field of the solenoid coil for $V_{C_3H_8} = 0.2\,\text{m/s}$.

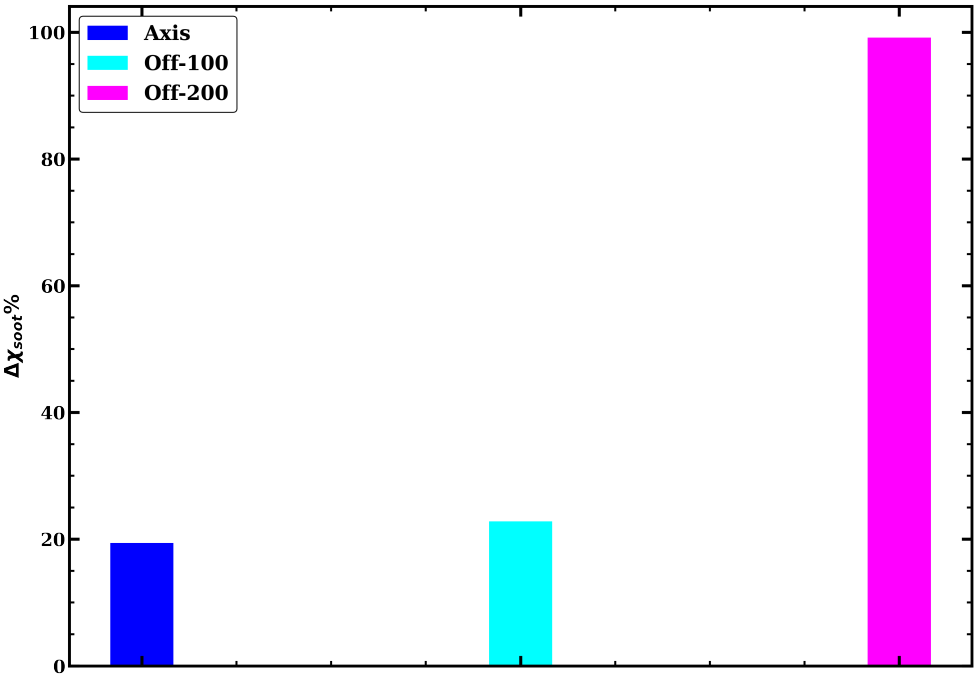

Figure 5.13. Effect of the magnetic field of the solenoid coil on soot volume fraction for $V_{C_3H_8} = 0.2\,\text{m/s}$.

Figure 5.12. and Figure 5.13. depict the effect of the solenoid's magnetic field on the soot volume fraction of the non-premixed flames . Figure 5.14. and Figure 5.15. show

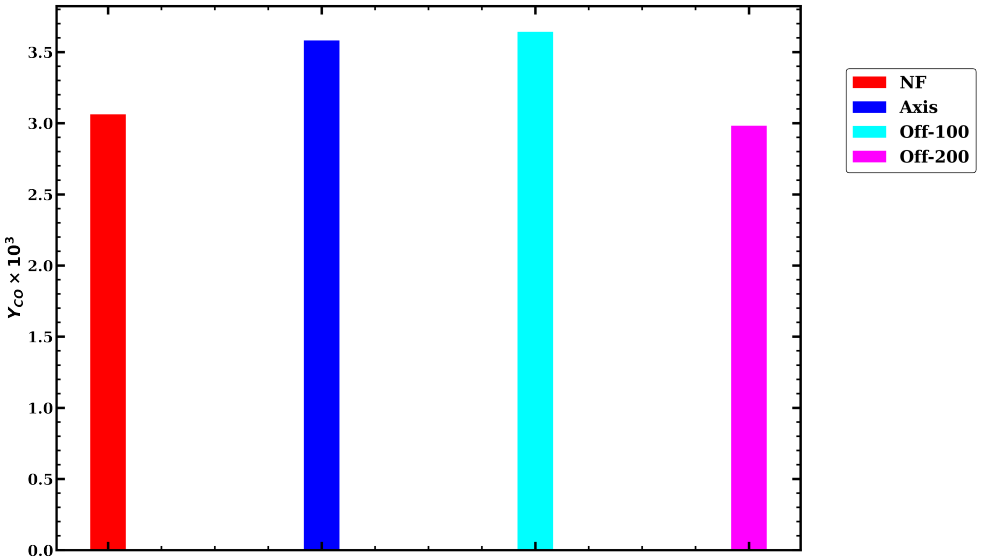

Figure 5.14. Average CO mass fraction due to the imposed magnetic field of the solenoid coil for $V_{C_3H_8} = 0.2\,\text{m/s}$.

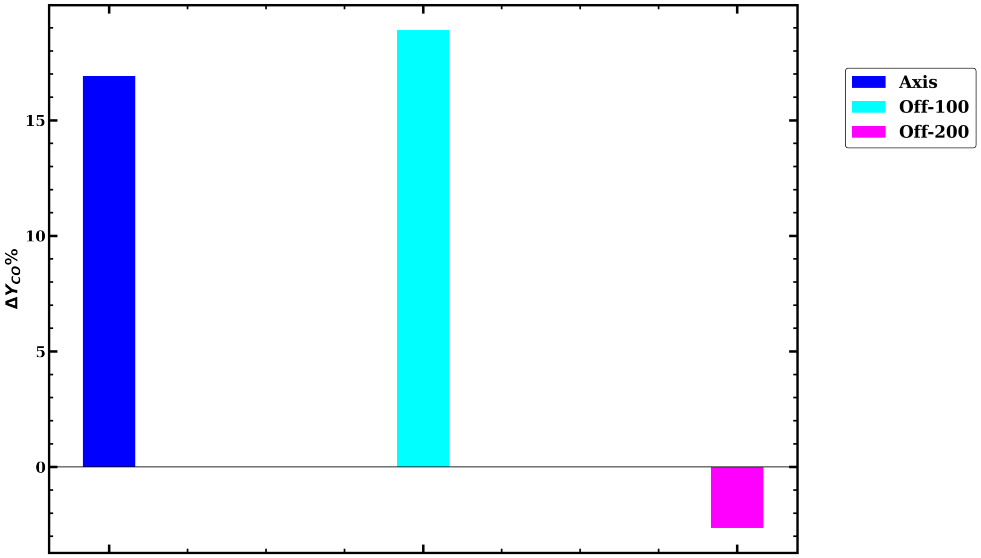

Figure 5.15. Effect of the magnetic field of the solenoid coil on CO mass fraction for $V_{C_3H_8} = 0.2\,\text{m/s}$.

the effect of the magnetic field on CO generated by the non-premixed flame .

When the burner exit plane is located at the center of the solenoid coils, the outward radial displacement of O_2 dominates the region where the flame is formed . Thus, the migration of O_2 retards the soot oxidation process, which promotes the formation of soot Figure 5.12.. In the same view, the oxidation of CO is retarded by the migration of O_2 induced by the magnetic field. This resulted in an increased average mass fraction

of CO in the combustion domain Figure 5.14. .

However, when the burner exit plane is located at 200 mm from the center of the solenoid, the region where oxygen migrates inwards to the flames encompasses the region of formation of CO. This migration of O_2 promoted the oxidation of CO which resulted in the reduction of the average mass fraction of CO. However, since the region of the formation of soot is below the inward migration of O_2, the oxidation of soot process is not promoted, thus resulting in an increased average soot volume fraction.

5.3. Conclusion

In this chapter, the effect of magnetic field on CO and soot formation in non-premixed flames was studied numerically. The presence of magnetic fields in the vicinity of non-premixed flames decelerates or accelerates the fluid flow of the gaseous mixture depending on the location of the burner exit plane in the magnetic field. The location of the flame within the magnetic field is inherently associated with the magnetic field variation imposed on the flame.

Results demonstrate that the presence of a magnetic field in the vicinity of non-premixed flames affects the variation of the mass fraction of O_2 and C_2H_2. This effect is due to the change in the body force acting on the flow field by the imposed magnetic field gradient. An increased body force promotes the combustion process.

The effect of the magnetic field on the emission of soot depends on the strength of the imposed magnetic field. This effect becomes pronounced as the magnetic field increases above 1 T. Overall, results indicate that the presence of a magnetic field increased the amount of soot produced by non-premixed flames. However, the magnetic field reduced the amount of soot when the flame burner exit is located at the center of the solenoid and offset by 200 mm.

The imposition of magnetic field on non-premixed flame increased the average mass fraction of CO by about 5% on average for the locations considered for all the solenoid coil, but decreases when the burner exit is offset by 200 mm when the number of turns

of coils is N. As the flame size decreases, the magnitude of the effect of the magnetic field on soot and CO increases.

Chapter 6.
Conclusion

The objective of this research is to predict the effect of magnetic fields on CO and soot generated by non-premixed flames numerically. In this regard, a commercial computational fluid dynamics (CFD) tool - Ansys-Fluent [77] was used to predict non-premixed flame characteristics which agrees to a large extent with empirical results presented in Chapter3.. In addition to the computation of the flame characteristics, the formation of soot was computed using the Moss-Brookes model [78]. Although the computed soot for a particular empirical scenario in literature did not qualitatively agree with the empirical data, the volume fraction of soot computed agrees with the empirical data.

To study the effect of the magnetic field gradient on the formation of CO and soot, the imposed magnetic fields are computed using a commercial CFD tool - Ansys-Maxwell [82]. In Chapter3., a verification of the computation was conducted by computing the magnetic of a permanent magnet which agreed with an exact relation of the magnetic field.

The presence of magnetic field in the vicinity of non-premixed flames induced additional body forces which either decrease or increase the buoyancy force acting on the paramagnetic species of the combustion process. This additional body force is incorporated into the CFD tool with an add-on script which imports the computed magnetic field gradient and computes the induced body force on the paramagnetic species.

In this research, two scenarios of the imposed magnetic fields were considered - a pair of an infinitely wide permanent magnet and wound solenoid coils. The imposed magnetic fields were computed for each case. To model the coflow non-premixed flames, an axisymmetric assumption was considered to simplify the computational domain without compromising the quality of the results obtained in relation to

experimental data. In this regard, the geometry of the source of the imposed magnetic field studied in this work was chosen such that the axisymmetric condition of the computation is validated. The magnetic field of the infinitely permanent magnets is assumed to vary only in the axial direction. However, the magnetic field of the wound solenoid coils varies in the radial and axial direction of the flow domain which satisfies the axisymmetric condition. These computed magnetic fields are then imposed on the non-premixed flames by computing the additional body force induced by the magnetic field.

When the center axis of infinitely wide permanent magnet is located in the neighborhood of the non-premixed flame tip, the volume average mass fraction of CO generated by the flame increased while the volume average soot volume fraction decreased. In addition, when the center axis of the infinitely wide permanent magnet is located at the flame burner exit plane, the average soot volume fraction produced decreased while volume average mass fraction of CO increased. At these locations, the magnitude of the effects of the magnetic field on the volume average of the mass fraction of CO and soot volume fraction is less pronounced due to the magnitude of the imposed magnetic field gradient. However, when the flame burner exit plane is below the axis of the permanent magnet, the average soot volume fraction increased. This can be attributed to the reduction of the body forces acting on flame around the flame burner exit which deter the combustion process.

Since the magnitude of the effect of the magnetic field was negligible when the size of the magnetic field is less than 1 T, the magnetic field of a wound solenoid coil is imposed on the non-premixed flame such that the magnitude of the magnetic field can be varied so that the imposed magnetic field is greater than 1 T. As a results, varying peak magnetic field was imposed on the non-premixed flame. The relative magnitude of the effect of the imposed magnetic field is pronounced when the peak magnetic field is greater than 1 T. When the non-premixed flame is placed in the vicinity of the

wound solenoid coils, the average mass fraction of CO generated increased. However, the volume average of soot volume fraction decreased when the flame burner exit plane is located at the center of the wound solenoid coils, but increased when the flame burner exit plane is 100mm off from the center of the solenoid coils. Considering these results obtained, the reduction of the soot volume fraction is attributed to the net reduction of the body force acting on the paramagnetic species.

Comparing the effect of the imposed magnetic fields studied, the magnetic fields of the wound solenoid coils induced a reasonable effect on the average amount of CO and soot generated by the non-premixed flames. Neglecting the cost effect of installing the source of the magnetic fields, the wound solenoid coils is effective in changing the pollutant propensity of non-premixed flames when placed in the vicinity of the flame. This is due to the relative magnitude of the magnetic field imposed by the wound solenoid coil.

6.1. Future Work proposed

Although the results of this work are obtained computationally, an experimental study is proposed to validate the results of these computations and further elucidate the relevance of magnetic field in the area of combustion controls.

In addition, the laminar case presented could be extended to the turbulent region of the flow for practical systems such as furnaces. In the turbulent region, the imposed magnetic field will affects the turbulence mixing depending on the nature of the magnetic field gradient in the region of flow.

Appendix
Magnetic Body Force

In order to compute the magnetic body force exerted on a magnetic fluid, we consider a finite volume δV of the fluid which is located in the vicinity of the magnetic field **H**. The magnetization vector **M** and pole density ρ_v of the fluid are related by [23]:

$$\rho_v = -\mu_m \nabla \cdot \mathbf{M} \tag{1.}$$

However, the magnetic force density on the magnetic fluid due to the magnetic field **H** is given as:

$$\mathbf{f}_{mag} = \rho_v \mathbf{H} = -\mu_m \nabla \cdot \mathbf{M} \tag{2.}$$

Using Coulomb's law, $-\mu_m \nabla \cdot \mathbf{M} = \mu_m \nabla \cdot \mathbf{H}$. Then equation 2. can be expressed as:

$$\mathbf{f}_{mag} = \mu_m \mathbf{H}(\nabla \cdot \mathbf{H}) \tag{3.}$$

Using tensor identity $\mathbf{H}(\nabla \cdot \mathbf{H}) = \nabla \cdot (\mathbf{HH}) - \mathbf{H} \cdot (\nabla \mathbf{H})$

However,

$$\mathbf{H} \cdot (\nabla \mathbf{H}) = \nabla\left(\frac{1}{2}H^2\right) - \mathbf{H} \times (\nabla \times \mathbf{H}) \tag{4.}$$

Using Maxwell's equation (1.32.) for magnetostatics, $\nabla \times \mathbf{H} = 0$, then equation (4.) becomes $\mathbf{H} \cdot (\nabla \mathbf{H}) = \nabla\left(\frac{1}{2}H^2\right)$. Thus, $\mathbf{H}(\nabla \cdot \mathbf{H}) = \nabla \cdot (\mathbf{HH}) - \nabla\left(\frac{1}{2}H^2\right)$

Equation 3. can be expressed as:

$$\mathbf{f}_{mag} = \nabla \cdot \left[\mu_m \left(\mathbf{HH} - \frac{1}{2}H^2 \mathbb{I}\right)\right] \tag{5.}$$

Considering the normal force component of 5., the magnetic body force is given as:

$$\mathbf{f}_{\text{mag}} = \nabla \cdot \left(\frac{1}{2} \mathrm{H}^2 \mathbb{I} \right) \tag{6.}$$

$\mathbb{I}$ is the unit Tensor.

References

[1] M. Smooke, M. Long, B. Connelly, M. Colket, and R. Hall, "Soot formation in laminar diffusion flames," vol. 143, no. 4, pp. 613–628, 2005.

[2] P. Gillon, W. Badat, V. Gilard, and B. Sarh, "Influence of a horizontal magnetic field on a co-flow methane/air diffusion flame," *Combustion Science and Technology*, vol. 180, no. 10-11, pp. 1920–1935, 2008.

[3] A. Linan and F. A. Williams, *Fundamental Aspects of Combustion*. 200 Madison Avenue, New York: Oxford University Press Inc., 1993.

[4] I. E. Agency, "2018 global energy and co2 status report," International Energy Agency, Report, 2018.

[5] S. R. Turns, *An introduction to combustion: Concept and Applications*. McGraw-Hill Companies Inc, 2000.

[6] C. K. Law, *Combustion physics*. New York: Cambridge University Press, 2006.

[7] J. Warnatz, U. Maas, and R. W. Dibble, *Combustion: Physical and Chemical Fundamentals, Modeling and Simulation, Experiments, Pollutant Formation*, 4th ed. Berlin: Springer, 2006.

[8] D. Veynante and L. Vervisch, "Turbulent combustion modeling," *Progress in energy and combustion science*, vol. 28, no. 3, pp. 193–266, 2002.

[9] K. K. Kuo, *Principles of combustion*, 2nd ed. Hoboken, N.J.: John Wiley, 2005.

[10] M. D. Smooke and V. Giovangigli, "Numerical modeling of axisymmetric laminar diffusion flames," *IMPACT of Computing in Science and Engineering*, vol. 4, no. 1, pp. 46–79, 1992.

[11] I. Glassman and R. A. Yetter, *Combustion*, 4th ed. Amsterdam ; Boston: Academic Press, 2008.

[12] K. K. Kuo and R. Acharya, *Fundamentals of turbulent and multiphase combustion*. Hoboken, N.J.: Wiley, 2012.

[13] F. G. Roper, "The prediction of laminar jet diffusion flame sizes: Part i. theoretical model," *Combustion and Flame*, vol. 29, pp. 219–226, 1977.

[14] R. J. Kee, M. E. Coltrin, P. Glarborg, and H. Zhu, *Chemically reacting flow : theory, modeling, and simulation*. Hoboken, NJ : John Wiley & Sons, 2018., 2018.

[15] S. P. Burke and T. E. W. Schumann, "Diffusion flames," *Industrial & Engineering Chemistry*, vol. 20, no. 10, pp. 998–1004, 1928.

[16] I. Zeldovich, G. I. Barenblatt, V. Librovich, and G. Makhviladze, "Diffusional combustion of gases," in *Mathematical theory of combustion and explosions*. Consultants Bureau, New York, NY, 1985.

[17] M. Ikegami, "Soot formation fundamentals," in *Advanced combustion science*. Springer, 1993, pp. 161–204.

[18] H. Bockhorn, "A short introduction to the problem—structure of the following parts," in *Soot Formation in Combustion*. Springer, 1994, pp. 3–7.

[19] T.-H. Kwak, S. Lee, S. Maken, H.-C. Shin, J.-W. Park, and Y. D. Yoo, "A study of gasification of municipal solid waste using a double inverse diffusion flame burner," *Energy & Fuels*, vol. 19, no. 6, pp. 2268–2272, 2005.

[20] M. Frenklach and H. Wang, *Detailed Mechanism and Modeling of Soot Particle Formation*, ser. Soot Formation in Combustion. Berlin: Springer Series in Chemical Physics, 1994, vol. 59.

[21] J. Walker, R. Resnick, and D. Halliday, *Fundamentals of physics*, 10th ed. Hoboken, NJ: Wiley, 2014.

[22] G. Meunier, *The finite element method for electromagnetic modeling*. London, Hoboken, NJ: ISTE ; Wiley, 2008.

[23] R. E. Rosensweig, *Ferrohydrodynamics*, ser. Cambridge monographs on mechanics and applied mathematics. Cambridge ; New York: Cambridge University Press, 1985.

[24] P. Campbell, *Permanent magnet materials and their application*. Cambridge England ; New York: Cambridge University Press, 1994.

[25] B. D. Cullity and C. D. Graham, *Introduction to magnetic materials*. John Wiley & Sons, 2011.

[26] K. L. Brown, Nancy J. ; Revzan and M. Frenklach, "Detailed kinetic modeling of soot formation in ethylene/air mixtures reacting in a perfectly stirred reactor," *The Combustion Institute*, vol. 27, no. 1, pp. 1573–1580, 1998.

[27] I. Glassman, "Soot formation in combustion processes," in *Symposium (international) on combustion*, vol. 22. Elsevier, 1989, Conference Proceedings, pp. 295–311.

[28] J. Appel, H. Bockhorn, and M. Frenklach, "Kinetic modeling of soot formation with detailed chemistry and physics: laminar premixed flames of c2 hydrocarbons," *Combustion and Flame*, vol. 121, no. 1-2, pp. 122–136, 2000.

[29] I. M. Kennedy, "Models of soot formation and oxidation," *Progress in Energy and Combustion Science*, vol. 23, no. 2, pp. 95–132, 1997.

[30] H. Calcote and D. Manos, "Effect of molecular structure on incipient soot formation," *Combustion and Flame*, vol. 49, no. 1-3, pp. 289–304, 1983.

[31] I. Khan, G. Greeves, and D. Probert, "Air pollution control in transport engines," *Institution of Mechanical Engineers*, vol. 205, 1971.

[32] P. Tesner, T. Smegiriova, and V. Knorre, "Kinetics of dispersed carbon formation," *Combustion and flame*, vol. 17, no. 2, pp. 253–260, 1971.

[33] K. M. Leung, R. P. Lindstedt, and W. P. Jones, "A simplified reaction mechanism for soot formation in nonpremixed flames," *Combustion and Flame*, vol. 87, no. 3-4, pp. 289–305, 1991.

[34] P. R. Lindstedt, *Simplified soot nucleation and surface growth steps for non-premixed flames*. Springer, 1994, pp. 417–441.

[35] M. Frenklach, "Reaction mechanism of soot formation in flames," *Physical Chemistry Chemical Physics*, vol. 4, no. 11, pp. 2028–2037, 2002.

[36] M. Frenklach, S. Taki, and R. Matula, "A conceptual model for soot formation in pyrolysis of aromatic hydrocarbons," *Combustion and Flame*, vol. 49, no. 1-3, pp. 275–282, 1983.

[37] H. Wang and M. Frenklach, "A detailed kinetic modeling study of aromatics formation in laminar premixed acetylene and ethylene flames," *Combustion and Flames*, vol. 110, no. 1-2, pp. 173–221, 1997.

[38] F. Zantedeschi, "On the motions presented by flame when under the electro-magnetic influence," *The London, Edinburgh, and Dublin Philosophical Magazine and Journal of Science*, vol. 31, no. 210, pp. 421–424, 1847.

[39] M. Faraday, "On the diamagnetic conditions of flame and gases," *The London, Edinburgh, and Dublin Philosophical Magazine and Journal of Science*, vol. 31, no. 210, pp. 401–421, 1847.

[40] Y. Pivovarenko, "Diamagnetism flame. faraday mystery," *Global Journal of Science Frontier Research: A Physics and Space Science*, 2016.

[41] S. Ueno, "Quenching of flames by magnetic fields," *Journal of Applied Physics*, vol. 65, 1988.

[42] N. I. Wakayama, "Behavior of gas flow under gradient magnetic fields," *Journal of Applied Physics*, 1990.

[43] ——, "Effect of a decreasing magnetic field on the flow of nitrogen gas," *Chemical Physics Letters*, vol. 185, no. 5-6, pp. 449–451, 1991.

[44] S. Ueno, H. Esaki, and K. Harada, "Magnetic-fields effects on combustion," *IEEE Translation Journal on Magnetics in Japan*, vol. TJMJ-2, 1987.

[45] N. I. Wakayama, "Effect of a gradient magnetic field on the combustion reaction of methane in air," *Chemical Physics Letters*, vol. 188, no. 3-4, pp. 279–281, 1992.

[46] N. I. Wakayama, I. Ogasawara, and H. Hayashi, "The external magnetic-field effect on the emission intensity of the na d-line in hydrogen oxygen flames," *Chemical Physics Letters*, vol. 105, no. 2, pp. 209–213, 1984.

[47] N. I. Wakayama, I. Ogasawara, T. Nishikawa, Y. Ohyagi, and H. Hayashi, "Magnetic quenching of the emission intensities of hpo and snh in hydrogen-oxygen flames." *Chemical Physics Letters*, vol. 107, 1984.

[48] T. Aoki, "Radicals' emissions and butane diffusion flames exposed to upward-decreasing magnetic fields," *Japanese Journal of Applied Physics*, vol. 28, 1989.

[49] ——, "Radical emissions and butane diffusion flames exposed to uniform magnetic fields encircled by magnetic gradient fields," *Japanese Journal of Applied Physics*, vol. 29, no. Part 1, No. 5, pp. 952–957, 1990.

[50] N. I. Wakayama, "Magnetic promotion of combustion in diffusion flames," *Combustion and Flame*, vol. 93, no. 3, pp. 207–214, 1993.

[51] J. Baker and M. E. Calvert, "A study of the characteristics of slotted laminar jet diffusion flames in the presence of non-uniform magnetic fields," *Combustion and Flame*, vol. 133, no. 3, pp. 345–357, 2003.

[52] B. Sarh, P. Gillon, V. Gilard, and E. Bodele, "Lengths of lifted laminar flames under vertical magnetic field gradient," *Combustion Science and Technology*, vol. 186, no. 10-11, pp. 1422–1433, 2014.

[53] V. Gilard, "Effects of a magnetic field on the stabilization of a lifted diffusion flame," *Proceedings of European Combustion Meeting*, 2009.

[54] P. Gillon, J. N. Blanchard, and V. Gilard, "Methane/air-lifted flames in magnetic gradients," *Combustion Science and Technology*, vol. 182, no. 11-12, pp. 1805–1819, 2010.

[55] N. I. Wakayama, "Magnetic support of combustion in diffusion flames under microgravity," *Combustion and Flame*, vol. 107, no. 1-2, pp. 187–188, 1996.

[56] S. Kinoshita, T. Takagi, H. Kotera, and N. I. Wakayama, "Numerical simulation of diffusion flames with and without magnetic field," *IEEE transactions on applied superconductivity*, vol. 14, no. 2, pp. 1685–1688, 2004.

[57] B. Jiang, P. Wang, and D. Liu, "Effects of magnetic fields on morphology and nanostructure evolution of incipient soot particles from n-heptane / 2, 5-dimethylfuran inverse diffusion flames," *Journal of Thermal Science*, vol. 29, no. 3, pp. 820–839, 2020.

[58] T. Delmaere, B. Sarh, and P. Gillon, "A numerical study of the magnetic influence on coaxial jets' flow upstream from lifted flames," *International Scientific Colloquium*, vol. 182, no. 11-12, pp. 1933–1944, 2010.

[59] J. A. Miller and R. J. Kee, "Chemical nonequilibrium effects in hydrogen-air laminar jet diffusion flames," *Journal of Physical Chemistry*, vol. 81, no. 25, pp. 2534–2542, 1977.

[60] N. W. Heys, F. G. Roper, and P. J. Kayes, "A mathematical model of laminar axisymmetrical natural gas flames," *Computers & Fluids*, vol. 9, no. 1, pp. 85–103, 1981.

[61] R. E. Mitchell, A. F. Sarofim, and L. Clomburg, "Experimental and numerical investigation of confined laminar diffusion flames," *Combustion and flame*, vol. 37, pp. 227–244, 1980.

[62] M. D. Smooke and M. B. Long, "Computatonal and experimental study of laminar flames," Brookhaven National Lab., Upton, NY (United States), Report, 1993.

[63] M. D. Smooke, R. E. Mitchell, and D. E. Keyes, "Numerical solution of 2d axisymmetric laminar diffusion flames," *Combustion Science and Technology*, vol. 67, pp. 85 – 122, 1989.

[64] M. S. Day and J. B. Bell, "Numerical simulation of laminar reacting flows with complex chemistry," *Combustion Theory and Modelling*, vol. 4, no. 4, pp. 535–556, 2000.

[65] A. Kazakov and M. Frenklach, "Dynamic modeling of soot particle coagulation and aggregation: Implementation with the method of moments and application to high-pressure laminar premixed flames," *Combustion and Flame*, vol. 114, no. 3, pp. 484–501, 1998.

[66] C. S. McEnally, A. M. Schaffer, M. B. Long, L. D. Pfefferle, M. D. Smooke, M. B. Colket, and R. J. Hall, "Computational and experimental study of soot formation in a coflow, laminar ethylene diffusion flame," vol. 27, no. 1, pp. 1497–1505, 1998.

[67] M. Smooke, C. McEnally, L. Pfefferle, R. Hall, and M. Colket, "Computational and experimental study of soot formation in a coflow, laminar diffusion flame," *Combustion and Flame*, vol. 117, no. 1-2, pp. 117–139, 1999.

[68] E. S. Oran and J. P. Boris, *Numerical simulation of reactive flow*. Cambridge university press, 2005.

[69] O. Zikanov, *Essential computational fluid dynamics*. John Wiley & Sons, 2019.

[70] T. Chung, *Computational fluid dynamics*. Cambridge university press, 2010.

[71] J. Blazek, *Computational fluid dynamics: principles and applications*. Butterworth-Heinemann, 2015.

[72] S. Gordon and B. J. McBride, *Computer Program for Calculation of Complex Chemical Equilibrium Compositions, Rocket Performance, Incident and Reflected Shocks, and Chapman-Jouguet Detonations. Interim Revision, March 1976*. Scientific and Technical Information Office, National Aeronautics and Space Administration, 1976.

[73] Ansys-Chemkin-Pro, *ANSYS® Academic Research Mechanical and CFD - Chemkin-Pro, Release 2019R1*. Ansys Inc., 2019.

[74] R. J. Kee, G. Dixon-Lewis, J. Warnatz, M. E. Coltrin, and J. A. Miller, "A fortran computer code package for the evaluation of gas-phase multicomponent transport properties," *Sandia National Laboratories Report SAND86-8246*, vol. 13, pp. 80 401–1887, 1986.

[75] F. A. Williams, R. J. Cattolica, K. Seshadri, and A. Sanchez, "Chemical-kinetic mechanisms for combustion applications," 2016. [Online]. Available: http://combustion.ucsd.edu

[76] S. B. Pope, "Computationally efficient implementation of combustion chemistry usingin situadaptive tabulation," *Combustion Theory and Modelling*, vol. 1, no. 1, pp. 41–63, 1997.

[77] Ansys-Fluent, *ANSYS® Academic Research Mechanical and CFD - Fluent, Release 2019R1*. Ansys Inc., 2019.

[78] S. Brookes and J. Moss, "Predictions of soot and thermal radiation properties in confined turbulent jet diffusion flames," *Combustion and Flame*, vol. 116, no. 4, pp. 486–503, 1999.

[79] S. J. Brookes, "Soot production and thermal radiation from turbulent jet diffusion flames," Dissertation, 1996.

[80] J. M. Camacho and V. Sosa, "Alternative method to calculate the magnetic field of permanent magnets with azimuthal symmetry," *Revista mexicana de física E*, vol. 59, no. 1, pp. 8–17, 2013.

[81] E. M. Purcell, *Electricity and Magnetism*, 2nd ed. New York: McGraw-Hill Book Co., 1985.

[82] Ansys-Maxwell, *ANSYS® Academic Research Maxwell, 2019R1.* Ansys Inc., 2019.

[83] E. Yamada, M. Shinoda, H. Yamashita, and K. Kitagawa, "Numerical analysis of a hydrogen-oxygen diffusion flame in vertical or horizontal gradient of magnetic field," *Combustion science and technology*, vol. 174, no. 9, pp. 149–164, 2002.

[84] R. R. Gupta and A. Gupta, *Magnetic Properties of Paramagnetic Compounds*. Springer, 2012.

VITA

Edison Chukwuemeka was born and raised in Lagos, Nigeria. He obtained his Bachelors' degree in Mechanical Engineering from the University of Lagos, Akoka in Fall of 2008. After graduation, he worked with Schlumberger Nigeria for 3.5 years before enrolling to graduate school. Currently, he is a candidate for doctorate degree in Mechanical Engineering.